



BRNO UNIVERSITY OF TECHNOLOGY

VYSOKÉ UČENÍ TECHNICKÉ V BRNĚ

FACULTY OF MECHANICAL ENGINEERING

FAKULTA STROJNÍHO INŽENÝRSTVÍ

INSTITUTE OF SOLID MECHANICS, MECHATRONICS AND BIOMECHANICS

ÚSTAV MECHANIKY TĚLES, MECHATRONIKY A BIOMECHANIKY

ASSESSMENT OF THERMO-MECHANICAL FATIGUE OF EXHAUST MANIFOLD

POSOUZENÍ TEPELNĚ-MECHANICKÉ ÚNAVY VÝFUKOVÉHO POTRUBÍ

MASTER'S THESIS

DIPLOMOVÁ PRÁCE

AUTHOR

AUTOR PRÁCE

Bc. JOSEF KOŠTÁL

SUPERVISOR

VEDOUCÍ PRÁCE

Ing. FRANTIŠEK ŠEBEK, Ph.D.

BRNO 2020

Specification Master's Thesis

Department: Institute of Solid Mechanics, Mechatronics and Biomechanics
Student: **Bc. Josef Košťál**
Study programme: Applied Sciences in Engineering
Study branch: Engineering Mechanics and Biomechanics
Supervisor: **Ing. František Šebek, Ph.D.**
Academic year: 2019/20

Pursuant to Act no. 111/1998 concerning universities and the BUT study and examination rules, you have been assigned the following topic by the institute director Master's Thesis:

Assessment of thermo–mechanical fatigue of exhaust manifold

Concise characteristic of the task:

The reduction of components' mass in the automotive industry cannot do without thorough analyses for keeping the desirable fatigue life. Therefore, get the geometrical model of the cast iron exhaust manifold and obtain the data from the literature for calibration of the employed material model. Consider the material model at two levels of complexity at minimum and carry out the thermo–mechanical analysis of the exhaust manifold for the life assessment.

Goals Master's Thesis:

1. Getting the geometrical model of the exhaust manifold.
2. Obtaining the data from literature for employed cast iron.
3. Calibrating the material models at two levels of their complexity at minimum.
4. Conducting the thermo–mechanical analyses and life assessments.

Recommended bibliography:

AHMED, R., HASSAN, T.: Constitutive modeling for thermo-mechanical low-cycle fatigue-creep stress–strain responses of Haynes 230. *International Journal of Solids and Structures*, vol. 126–127, pp. 122-139, DOI:10.1016/j.ijsolstr.2017.07.031, 2017

AHMED, R., BARRETT, P. R., MENON, M., HASSAN, T.: Thermo-mechanical low-cycle fatigue-creep of Haynes 230. *International Journal of Solids and Structures*, vol. 126–127, pp. 90-104, DOI:10.1016/j.ijsolstr.2017.07.033, 2017

BARTOŠÁK, M., NOVOTNÝ, C., ŠPANIEL, M., DOUBRAVA, K.: Life assessment of SiMo 4.06 cast iron under LCF and TMF loading conditions. *Materials at High Temperatures*, vol. 36, no. 4, pp. 285-295, DOI:10.1080/09603409.2018.1542825, 2019

BARTOŠÁK, M., ŠPANIEL, M., DOUBRAVA, K.: Thermo-mechanical fatigue of SiMo 4.06 turbocharger turbine housing: Damage operator approach. *Engineering Failure Analysis*, vol. 105, pp. 736-755, DOI:10.1016/j.engfailanal.2019.06.068, 2019

EKSTRÖM, M., JONSSON, S.: High-temperature mechanical- and fatigue properties of cast alloys intended for use in exhaust manifolds. *Materials Science and Engineering: A*, vol. 616, pp. 78-87, DOI:10.1016/j.msea.2014.08.014, 2014

HALAMA, R., MARKOPOULOS, A., JANČO, R., BARTECKÝ, M.: Implementation of MAKOC cyclic plasticity model with memory. *Advances in Engineering Software*, vol. 113, pp. 34-46, DOI:10.1016/j.advensoft.2016.10.009, 2017

HAZIME, R. M., DROPPS, S. H., ANDERSON, D. H., ALI, M. Y.: Transient Non-linear FEA and TMF Life Estimates of Cast Exhaust Manifolds. *SAE International*, 2003-01-0918, DOI:10.4271/2003-0-0918, 2003

PEČ, M., ŠEBEK, F., ZAPLETAL, J., PETRUŠKA, J., HASSAN, T.: Automated calibration of advanced cyclic plasticity model parameters with sensitivity analysis for aluminium alloy 2024-T351. *Advances in Mechanical Engineering*, vol. 11, issue 3, pp. 1-14, DOI:10.1177/1687814019829982, 2019

SEIFERT, T., HAZIME, R., DROPPS, S.: TMF Life Prediction of High Temperature Components Made of Cast Iron HiSiMo: Part II: Multiaxial Implementation and Component Assessment. *SAE International Journal of Materials and Manufacturing*, vol. 7, issue 2, pp. 421-431, DOI:10.4271/2014-01-0905, 2014

VON HARTROTT, P., SEIFERT, T., DROPPS, S.: TMF Life Prediction of High Temperature Components Made of Cast Iron HiSiMo: Part I: Uniaxial Tests and Fatigue Life Model. *SAE International Journal of Materials and Manufacturing*, vol. 7, issue 2, pp. 439-445, DOI:10.4271/2014-01-0915, 2014

Deadline for submission Master's Thesis is given by the Schedule of the Academic year 2019/20

In Brno,

L. S.

prof. Ing. Jindřich Petruška, CSc.
Director of the Institute

doc. Ing. Jaroslav Katolický, Ph.D.
FME dean

Summary

This master's thesis deals with thermo-mechanical analysis and fatigue life prediction of the exhaust manifold. At first, a research study was carried out, in which the phenomenon of thermo-mechanical fatigue is reviewed. The main damage mechanisms and the modelling methods were presented. The specific behaviors of the materials subjected to thermo-mechanical loads were also covered. An overview of suitable material and fatigue life models was listed together with the algorithm of the fatigue life component prediction. Secondly, the theoretical background has been applied to the case study of the exhaust manifold subjected to thermo-mechanical loads. Two temperature-dependent elasto-plastic material models were calibrated and validated on the basis of experimental data, and the discretized finite element model of the exhaust manifold assembly was created. The model of the thermal boundary conditions was prescribed on the basis of steady state conjugate heat transfer analyses. One-way coupled thermal-mechanical finite element simulations were performed for each material model. A paradigm of uncoupled fatigue life model – suitable for low cycle fatigue – was used, hence the fatigue life prediction was evaluated in post-processing. Two fatigue life models were used – energy-based and strain-based. The obtained values of predicted fatigue life have been compared according to the material and fatigue life models which have been used. Lastly, the conclusions, the possibilities of further research and possible improvements are proposed and discussed.

Keywords

Cyclic plasticity, thermo-mechanical fatigue, finite element method, conjugate heat transfer, material model calibration, fatigue life prediction.

Rozšířený abstrakt

Tato diplomová práce se zabývá posouzením tepelně-mechanické únavy výfukového potrubí spalovacího motoru.

V úvodní kapitole je formulována problémová situace a cíle této práce. Dále byla provedena analýza podstatných veličin, které podstatně ovlivňují predikci únavového života při tepelně-mechanickém zatěžování. Na základě identifikovaných podstatných veličin byla vybrána vhodná metoda pro řešení.

V druhé kapitole je definice a dělení únavy, definice počtu cyklu do poruchy, fáze únavového života z mikro a makro pohledů, seznam použitelných přístupů pro predikce a obecná definice tepelně-mechanické únavy. Následně byla provedena rešeršní studie poškozujících mechanismů, které jsou přítomny u tepelně-mechanické únavy. Mezi tyto hlavní mechanismy patří únava (která je spojena s cyklickou plasticitou), oxidace a creep. Pro mechanismus únavy byly diskutovány základy inkrementální teorie plasticity, skládající se z mezní podmínky plasticity, zákonu tečení a zákonu zpevnění. Hlavní důraz byl kladen na modely kinematického zpevnění. U mechanismu oxidace jsou rozebrány efekty prostředí a jsou zmíněné reference, které se detailněji zabývají tímto fenoménem. Z literatury bylo zjištěno, že se oxidace často uvažuje v modelech nepřímo, proto tento fenomén nebyl studován do větší hloubky. Pro mechanismus creepového poškození byl popsán Nortonův model, který je nejčastěji používán pro predikce únavového života komponent podléhajících tepelně-mechanické únavě.

Třetí kapitola se zaměřuje na tzv. hot end spalovacího motoru. Ten je tvořen výfukovým potrubím a statorem turbínové části turbodmychdla. Tyto komponenty jsou

vystaveny nejnáročnějším provozním podmínkám, které sestávají z opakovaných tepelných gradientů. Dále byly popsány nejčastěji používané skupiny litin, které se pro hot end používají. Následuje přehled specifických testů na úrovni vzorku, které jsou potřebné na kalibrace modelů materiálu a modelů únavové životnosti. Současně jsou zde vyobrazeny i některé fenomény, které se v těchto aplikacích objevují (ratcheting, shake-down, cyklické zpevnění a změkčení, relaxace napětí atd.). Velmi specifické jsou testy tepelně–mechanické únavy, při kterých se vzorek zatěžuje posuvem i teplotou. Podle fáze mezi profilem posuvu a teploty se tyto testy dělí na „ve fázi” a „mimo fázi”. Testy tepelně–mechanické únavy jsou velmi důležité pro validaci anizotermálního chování. Následně byl na základě mnoha referencí vytvořen algoritmus predikce tepelně–mechanické únavy výfukového potrubí. Algoritmus zahrnuje odhad tepelných okrajových podmínek, slabě sdruženou tepelně–deformační úlohu, kalibraci modelu materiálu a modelu únavového života na základě testů na úrovni vzorku, predikci únavového života jako součásti post-processoru a návrh na validaci na úrovni komponenty. Poté jsou prezentovány modely materiálů z referencí, které jsou vhodné na tuto predikci. Byl popsán rozdíl mezi sjednocenými a nesjednocenými viskoplastickými modely materiálů a ukázáno rozšíření o teplotní člen. V závěru kapitoly jsou dále prezentovány modely únavové životnosti, které byly také nalezeny v referencích. Na základě těchto znalostí byly vybrány varianty modelů materiálů a modelů únavové životnosti, které byl autor schopen aplikovat na dostupných datech z literatury v praktické studii.

Následuje tedy čtvrtá kapitola, ve které je aplikována předchozí rešerše na praktický příklad. V této případové studii je analyzováno výfukové potrubí z čtyřválcového diesellového motoru. Uvažovaný materiál je SiMo 4.06, pro který byla velká část potřebných testů na úrovni vzorku publikována v řadě článků. Pro výfukové potrubí byly nakalibrovány dva tepelně závislé a časově nezávislé modely materiálu. První kalibrovaný model je bi-lineární model kinematického zpevnění BKIN a druhý kalibrovaný model je nelineární model kinematického zpevnění Chaboche. Pro oba modely je kalibrace detailně vysvětlena. Oba modely byly validovány na izotermální a anizotermální úrovni. Byla diskutována důležitost klesajícího trendu identifikovaných parametrů modelu v závislosti s rostoucí teplotou a objektivnost i robustnost řešení při velkém počtu určovaných parametrů. Dále byly zmíněny modely materiálu pro další komponenty sestavy – při analýze komponenty je totiž uvažováno vodní chlazení od hlavy motoru a vliv předepnutých šroubů. Jak model hlavy motoru, tak model šroubů předpokládají tepelně závislý lineární elastický model materiálu. Stejný přístup byl nalezen i v literatuře. Taktéž fyzikální vlastnosti všech komponent jsou uvažovány tepelně závislé – hustota, měrná tepelná kapacita, tepelná vodivost a koeficient tepelné roztažnosti. Ty byly také převzaty z literatury. Výfukové potrubí je zatížené reprezentativním tepelným cyklem (= tepelný šok), který byl částečně vytvořen na základě literatury a částečně konzultován s expertem v tomto oboru. Reprezentativní tepelný šok představuje zatížení, kterému by potrubí bylo vystavené počas svého servisního života. Krátce je i zmíněna metoda, jakou se tento cyklus dá získat na základě reálných dat. Okrajové podmínky nucené konvekce od výfukových plynů pro přechodovou teplotní úlohu byly zjištěny s využitím výpočtového modelování dynamiky tekutin. Tento přístup byl zmíněn v mnoha referencích. Úloha se řeší jako sdružený přestup tepla mezi výfukovým plynem a výfukovým potrubím. Byl ukázán postup, jakým způsobem tyto výsledky analyticky verifikovat a jak je zpracovat a namapovat do následující zmíněné přechodové teplotní úlohy v komerčním softwaru využívající metodu konečných prvků. Následně byla spočítána slabě sdružená tepelně–deformační úloha me-

todou konečných prvků. Získaná data z těchto analýz slouží jako vstup do modelu únavové životnosti. Tomu odpovídá paradigma nízko-cyklové únavy – úloha je řešena sekvenčně jako tepelně–deformační a predikce únavy je součástí post-procesu (předpokladem je, že poškození zpětně neovlivňuje mechanickou odezvu). Z dostupných testů na úrovni vzorku a referencí byly použity dva modely únavové životnosti – tepelně nezávislý model s energetickým přístupem a tepelně závislý model s deformačním přístupem. Energetický model byl implementován do post-procesoru komerčního softwaru a pro deformační model byl vytvořený skript, který pracuje jak s teplotami z tepelné úlohy, tak s amplitudou přetvoření z deformační úlohy. Predikované hodnoty cyklů do poruchy jsou poté zpětně namapovány na diskrétní síť modelu a zobrazeny jako kontury. Celkem tedy byly získány čtyři sady výsledků predikovaných cyklů do porušení (pro dva modely materiálu a dva modely únavové životnosti).

V závěru jsou mezi sebou soubory výsledků porovnány. Plastická deformace, predikována modelem materiálu Chaboche, byla na větších a více oblastech v porovnání s modelem BKIN. Dále bylo zjištěno, že v tomto případě nemá na predikci životnosti v kritické oblasti zásadní vliv model materiálu, ale zásadní vliv má model únavové životnosti. Tato kritická oblast je predikována pro všechny kombinace modelů materiálu a modelů únavové životnosti na stejném místě. Výsledky se liší o faktor 2, což není neobvyklá diskrépance na základě jedné z referencí (kde byl rozdíl v predikci životnosti pro použité modely únavové životnosti o velikosti faktor 3). Dále jsou navržené testy na úrovni komponenty, které by sloužily pro kalibraci tepelné úlohy a validaci použitého postupu. Také jsou diskutovány nedostatky použitých modelů a možnosti dalšího výzkumu a vývoje.

Klíčová slova

Cyklická plasticita, tepelně–mechanická únava, metoda konečných prvků, sdružený přestup tepla, kalibrace modelu materiálu, predikce únavové životnosti.

KOŠŤÁL, Josef. *Assessment of thermo-mechanical fatigue of exhaust manifold*. Brno, 2020. Available from: <https://www.vutbr.cz/studenti/zav-prace/detail/121573>. Master's Thesis. Brno University of Technology, Faculty of Mechanical Engineering, Institute of Solid Mechanics, Mechatronics and Biomechanics. 109 p. Supervisor František Šebek.

I declare that I have written the master's thesis *Assessment of thermo-mechanical fatigue of exhaust manifold* on my own, under the supervision of Ing. František Šebek, Ph.D., using the sources listed in the bibliography.

Brno, June 2020

Bc. Josef Košťál

I would like to pay my special regards to prof. Dr.-Ing. Thomas Seifert of the University of Offenburg, not only for the knowledge shared regarding the thermo–mechanical fatigue and the number of great references provided, but also for the positive and empathetic approach, sincere kindness and willingness to spend time with me on the calls, answering my questions.

I would like to express my sincere gratitude to my supervisor Ing. František Šebek, Ph.D. who was a great mentor to me, with a friendly yet professional and passionate approach, and mainly for the honest and very frequent consultations during the thesis development.

Next I would like to thank the Garrett Advancing Motion employees, who advised me with several aspects of the thesis: Ing. Michal Kotačka with conjugate heat transfer modelling, Ing. Luděk Pohořelský, Ph.D., with the boundary conditions for the thermal shock, Bc. Matúš Oboňa with the 3D geometry creation, Ing. Adam Šabart with the practical tips for the component thermo–mechanical analysis, and Ing. Tomáš Lasota, Ph.D., with the provision of the references for the thermo–mechanical fatigue.

Another acknowledgment is for Dr. Sam Beaton, Ph.D., for the proofreading.

Finally, I would like to thank to my parents and grandparents for the continuous support during my university studies.

Bc. Josef Košťál

Contents

1	Introduction	14
1.1	Motivation	14
1.2	Problem Formulation and Thesis Objectives	14
1.3	Substantial Factors and Method Chosen for Solution	15
2	Thermo–Mechanical Fatigue	17
2.1	Damage Mechanisms	19
2.1.1	Fatigue – Cyclic Plasticity	19
2.1.2	Oxidation	24
2.1.3	Creep	24
3	High Temperature Components in Combustion Engines – Hot End	26
3.1	Heat Resistant Casting Materials in the Hot End	26
3.2	Material Testing	28
3.2.1	Tensile Test at Increased Strain Rate	28
3.2.2	Low Cycle Fatigue Test	28
3.2.3	Thermo–Mechanical Fatigue Test	33
3.2.4	Complex Low Cycle Fatigue Test	36
3.2.5	Creep Test	37
3.3	Algorithm of Thermo–Mechanical Fatigue Life Prediction	38
3.3.1	Overview of Used Material Models	40
3.3.2	Overview of Used Fatigue Life Models	43
4	Thermo–Mechanical Fatigue of the Exhaust Manifold – Case Study	46
4.1	Material Model	46
4.1.1	Considered Material	46
4.1.2	Available Experiments	47
4.1.3	Calibration and Validation of Material Models	49
4.1.4	Material Model for Additional Components	64
4.2	Finite Element Model	65
4.2.1	Model of Geometry	65
4.2.2	Model of Thermal Boundary Conditions	66
4.2.3	Finite Element Mesh	72
4.2.4	Transient Thermal Finite Element Analysis	72
4.2.5	Structural Finite Element Analysis	76
4.3	Fatigue Life Prediction	77
4.3.1	Fatigue Life Model	77
4.3.2	Comparison of Used Material and Fatigue Life Models	83
4.3.3	Validation of Results	91
4.3.4	Limitations of Used Model	92
5	Conclusion	94
6	List of symbols and abbreviations	103

1. Introduction

1.1. Motivation

The exhaust manifold is one of the components in the exhaust system of the combustion engine. The main function of the exhaust manifold is to contain and guide the exhaust gases from the engine head to the turbocharger and/or to the catalytic converter. Throughout its service life, the exhaust manifold is expected to endure severe repeated thermal cycling under harsh operating conditions, including start-up, stop and full load phases of the combustion engine [18, 70]. The operating temperatures for cast iron exhaust manifolds can be up to 800°C [52]. To increase the exhaust gas temperature is a frequent trend in the automotive industry, since it leads to the reduction of fuel; and hence reduction of the amount of pollutant emissions [38]. The aforementioned conditions impose transient inhomogeneous temperature fields, which together with the constraints from the mating components and the thermal expansion lead to inelastic mechanical strains. Therefore, there is a risk of Thermo–Mechanical Fatigue (TMF) of this component, leading to failure – meaning exhaust gas leakage. Additionally, the reduction of component mass plays an important role in the automotive industry, therefore a reliable TMF life prediction is necessary in order to minimize the number of conducted bench tests – avoiding over-dimensioning while fulfilling the service life. There are multiple phenomena occurring in TMF. The main damage mechanisms are fatigue, creep and oxidation of the material. To be able to capture such behaviors, reliable and sophisticated material and fatigue life models are needed in the TMF life predictions. Due to the rapid increase of the computational performance, significant progress has been done in the recent decade in TMF life predictions, regarding material and fatigue life models and finite element method modelling. This field remains relatively new, therefore there is much space for further research and development.

1.2. Problem Formulation and Thesis Objectives

The formulation of the problem is „*Realization of thermo–mechanical analysis of the exhaust manifold and its fatigue life prediction.*”

At first, the theoretical research was done in Chapters 2 and 3. After the theoretical background, the practical part of the thesis in Chapter 4 follows. The practical part meets the following objectives:

- Getting the geometrical model of the exhaust manifold.
- Obtaining the experimental data from literature for employed cast iron.
- Calibrating and validating the material models at various levels of their complexity based on the uniaxial experimental data.
- Calibrating and validating the fatigue life models based on the uniaxial experimental data.
- Creating the Finite Element (FE) model of the exhaust manifold, conducting the thermo–mechanical analyses with calibrated material models and life assessments

using calibrated fatigue life models. Comparing utilized engineering approaches regarding their fatigue life prediction.

1.3. Substantial Factors and Method Chosen for Solution

To be able to conduct the prediction realistically, one must identify the substantial factors that influence the TMF life predictions of the component (i.e. the exhaust manifold). Many of these factors are described broadly in the thesis, but a short overview is listed in this section. The suitable method of solution is chosen on the basis of these factors. The system of substantial factors is created on the basis of [44]:

Surroundings of the Component

The knowledge of surroundings of the component is important in order to prescribe correct boundary conditions for the thermal analysis. The external surfaces are being cooled by natural convection. Additionally, the oxidation which happens on the external surface of the component under high temperatures contributes to the damage, hence the type of the environment is also important. The manifold is located in the engine compartment and thereby exposed to ambient air. This exposure reduces fatigue life compared to a hypothetical scenario in which the manifold is surrounded by an inert atmosphere.

Geometry and Topology of the Component

Both geometry and topology of the components can be represented well by a three dimensional computer-aided design model. The manufacturing tolerances are considered as a non-significant factor.

Mates of the Component

The exhaust manifold is mounted to the engine head with bolts. This creates two sets of mates. From the thermal perspective, the water-cooled engine head cools down the exhaust manifold. The thermal contact conductance is dependent on the surfaces of the flanges and on the tightening of the bolts. From a structural perspective, the bolts constrain the expansion of the manifold.

Loads Acting on the Component

The exhaust manifold is loaded by the forced convection from the exhaust gases, which heat the internal surfaces. The load which the manifold experiences in the real driving conditions is represented by the thermal shock cycle, which is used for predictions in virtual models and for validations of the component prototypes. An additional load is caused by the bolt pretension, since the manifold is mounted to the engine head.

Properties of the Component

It is necessary to take into consideration the temperature dependency of both physical and mechanical properties, since the change in temperature can be more than 700°C. There

are several damage mechanisms present, which are addressed later – fatigue (related to cyclic plasticity), oxidation and creep. This means that the plasticity and creep should be included in the model. As described later, the oxidation can be included indirectly. These properties are derived on the basis of uniaxial experimental data. Ideally, a number of uniaxial tests should be conducted to include the stochastic character. However, due to financial resources, this is often neglected and a deterministic character is assumed.

Consequences of Loads Acting on the Component

The forced convection caused by the hot exhaust gases makes the manifold experience inhomogenous thermal gradients. These gradients, together with the thermal expansion of the material, cause the development of repeated inelastic strains. In addition, the bolted connection of the manifold and the engine head constrains the manifold to expand, leading again to repeated inelastic strains. Finally, the dwells in the thermal shock cycle at high temperatures can cause material to creep, leading again to the development of inelastic strains. All these damages accumulate in each cycle, resulting in the crack initiation after a number of cycles.

Method Chosen for Solution

Due to non-linear material behavior, contacts and temperature dependency of the properties, it is a non-linear problem. Furthermore, the component has a generic three dimensional shape that cannot be solved analytically. The problem can be validated experimentally on the test benches, however the goal of the companies is to minimize the number of prototype tests in order to reduce costs. Therefore, the Finite Element Method (FEM) is suitable for the solution of such a problem. Using the FEM, the thermal distribution can be calculated, leading to the calculation of strain tensors using the coefficient of thermal expansion, with consideration of elasto-plastic material. The fatigue life prediction is realized afterwards as a part of post-processing, using the FEM outputs.

2. Thermo–Mechanical Fatigue

Fatigue is a cumulative type of failure, depending not only on the instantaneous load, but on the loading history. Permanent changes and accumulation of damage occur in the material subjected to repeated or fluctuating strains. Fatigue can result in cracks and cause fracture after a sufficient number of cycles. Figure 2.1, the so-called S–N curve, visually represents the generic division of the fatigue failure [13, 75]. From the viewpoint of numbers of cycles to failure N_f , we distinguish three main groups – Low Cycle Fatigue (LCF), High Cycle Fatigue (HCF) and quasi-static fracture [75]:

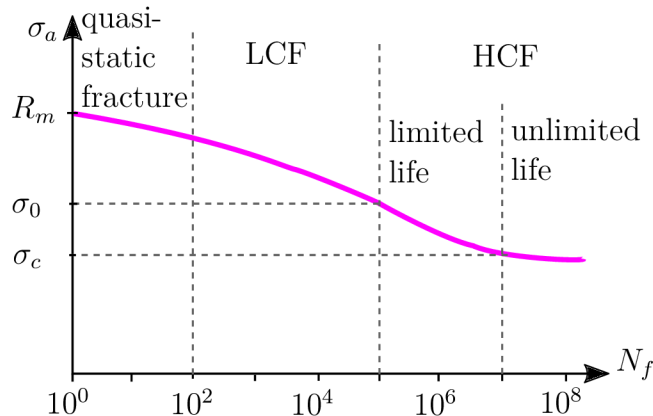


Figure 2.1: S–N diagram according to European conventions [75]

where σ is stress, subscript a indicates amplitude of the quantity, R_m is the ultimate tensile strength, σ_0 is the yield stress and σ_c is the endurance limit.

The HCF group is related to the vibrations of the components – typical are lower loads, with a higher amount of cycles and plasticity occurring only in the vicinity of the material defects. Most of the lifetime is drawn for the crack initiation. The HCF group can be subdivided into limited and unlimited life. For the unlimited life, there are nominal and localized approaches – notch and shape coefficients. The paradigm of the HCF unlimited life is that the theory does not work with the damage, and only linear analysis is performed. For the HCF limited life, the theory uses the damage accumulation (Palmgren–Miner hypothesis – linear damage accumulation). Note that the S–N curve is applicable only for the HCF [73].

The LCF failure occurs due to repeated cyclic plastic straining [13]. Typical are higher loads and lower numbers of cycles, and the plasticity occurring in macro-volumes (i.e. notches). The paradigm of the uncoupled model is that the fatigue damage does not influence mechanical response significantly. Therefore, the calculations can be done in sequence; structural analysis – fatigue life prediction (post-process) [73]. According to the European conventions, the border between LCF and HCF is considered to be $N_f = 10^5$ [75]. There are generally 5 stages of the fatigue failure process which are depicted in Figure 2.2 [75]. The microscopic and macroscopic (i.e. technical) points of view are shown in this figure. The technical crack initiation is up to the 3rd stage, followed by the technical crack propagation [75].

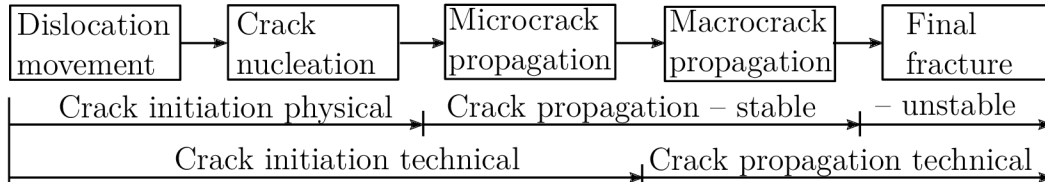


Figure 2.2: Stages of the fatigue process from the microscopic and macroscopic (technical) points of view [75]

The definition of N_f is also a convention – it can mean the fatigue fracture, the initiation of a crack of a defined size, or it can be defined as a decrease in stiffness of the specimen. For the LCF, it is practical to measure the number of cycles to crack initiation [73, 75]. Therefore, in this thesis, the fatigue is solved only up to the 3rd stage in Figure 2.2, and the N_f is a number of cycles to technical crack initiation. No macrocrack propagation is being solved or considered. Several approaches exist for the LCF predictions [75]:

- **Concept of fictitious linear elastic stress**, a highly simplified approach unifying the Manson–Coffin curve (described later in Subsection 4.3.1) with the S–N curve.
- **Concepts of local elasto–plastic stresses and strains**
 - **Concept of plastic stress redistribution (Neuber)**, based on the linear elastic analysis and superposition. However, it is limited for the LCF since it is always a non-linear task and generally the superposition principle does not work [73].
 - **Concept of equivalent energy (energy criterion Molski–Glinka)**, based on the assumption that the isovolumic strain energy density is the same for linear elastic and elasto–plastic deformations. The strain amplitude gained with this approach is lower compared to the Neuber approach, meaning the approach is less conservative [75].
 - **Using FEM in evaluation of elasto–plastic deformations**, this method enables the calculation of stress and strain tensors of the body of any shape at any discrete node, with a variety of non-linear material models [75]. Also, the material and physical models can be expanded by temperature dependency (which is significant in TMF cases). As mentioned before, the uncoupled paradigm is supposed – the fatigue analysis is done in sequence, firstly by the FEM simulation and then the fatigue life prediction is evaluated in post-processing [73]. As mentioned in the introduction, this method has been used in the practical part of the thesis in Chapter 4.

For the quasi-static fracture, a coupled fatigue model should be used – meaning the damage influences the mechanical response and the analysis cannot be done in sequence. The parameters of the phenomenological material model are changed during the analysis [73].

The TMF characterizes the fatigue of the material subjected to changes in temperature and mechanical strain. These conditions occur on the component under the temperature gradients or under the external constraints which restrict the thermal expansion. The TMF is in the LCF category. The TMF can be found, for example, in piping and pressure vessels in the electric power industry, turbine blades and disks in the aeronautic

industry, railroad applications or in the automotive industry – engine heads, pistons, exhaust manifolds, turbine housings in the turbocharger and the rest of the exhaust system (as described in Chapter 3) [13, 42]. Generally, there are three main damage mechanisms in the TMF [9], which are covered in the following Section 2.1.

2.1. Damage Mechanisms

2.1.1. Fatigue – Cyclic Plasticity

Fatigue is the first contributing damage mechanism, meaning the material experiences cyclic plasticity. There are many various material models developed to describe cyclic plasticity. Only the phenomenological models are the focus in this thesis, meaning the models based purely on the experimental behavior of the materials subjected to cyclic plasticity. The key to the phenomenological modelling are the experimental facts appearing in the material subjected to cyclic plasticity. One of the most important and well-known phenomenon is Bauschinger’s effect, which describes the reduction of the elasticity in the reverse loading. It means that the σ_0 value in tension is not equal to $-\sigma_0$ in compression, but it is an approximate drop of magnitude of $2\sigma_0$ from the tensile peak [13, 36]. Essentially, it is an effect related to dislocation pile-ups at the grain boundaries, which “helps” to yield material earlier in reverse loading [48]. Other phenomena, such as cyclic hardening/softening or Masing behavior are described in Section 3.2. Figure 2.3, where ε is strain, depicts Bauschinger’s effect [13, 36].

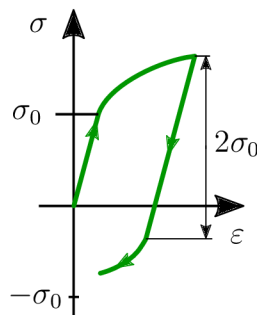


Figure 2.3: Illustration of Bauschinger’s effect, created on the basis of [13, 36]

According to [36], the constitutive models for the cyclic plasticity can be divided into the following groups:

- Overlay models
- Single-surface models
- Multisurface models
- Two-surface models
- Endochronic models
- Models with yield surface distortion

Only the single-surface models are going to be briefly discussed in this subsection, since they are popular, robust and widely implemented in commercial software.

The incremental theory of plasticity has three main pillars: **yield criterion**, **flow rule** and the **hardening rule** [68].

Yield Criterion

The yield criterion describes the boundary between the elastic and plastic deformation in the material model [68]. The most common and widely implemented in commercial software is the von Mises yield criterion. This criterion is defined as [35]:

$$F = \sqrt{\frac{3}{2} \underline{S} : \underline{S}} - \sigma_0 = 0 \quad (2.1)$$

where F is a yield surface and \underline{S} is a deviatoric stress tensor. The von Mises yield criterion has a shape of a cylinder in the Haigh–Westergaard space (where $\sigma_{I,II,III}$ are principal stresses), with the axis of hydrostatic pressure as depicted in Figure 2.4.

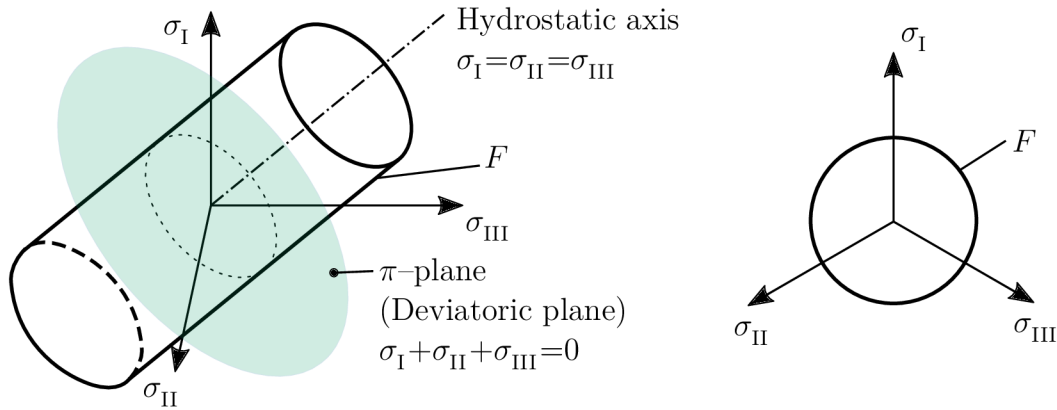


Figure 2.4: Von Mises yield criterion depicted in Haigh–Westergaard space (left) and in deviatoric plane (right) [15]

The von Mises yield criterion is applied in the practical part of this thesis. Apart from this criterion, other yield criteria (i.e. Tresca, Drucker–Prager, Mohr–Coulomb, etc.) exist [68], however they are not usually implemented in commercial software. These criteria are usually implemented as user sub-routines.

Flow Rule

The flow rule describes the direction of the development of plastic deformation [68]. Equation 2.2 describes it as [2]:

$$d\varepsilon_{pl} = d\lambda_p \frac{\partial Q_p}{\partial \underline{\sigma}} \quad (2.2)$$

where ε_{pl} is the plastic strain tensor, λ_p is the plastic multiplier, $\underline{\sigma}$ is the stress tensor and Q_p is plastic potential. The most commonly-used and commercially implemented rule is the associative flow rule. The associative flow rule directs the development of plastic deformation perpendicularly to the yield surface F as per Figure 2.5 [68]. Hence, the plastic potential Q_p is equal to yield surface F .

Apart from the associative flow rule, the non-associative flow rules exist. In non-associative flow rule, the plastic flow is not connected to the yield surface and it is directed by a different surface – plastic potential [68]. However, the non-associative flow rules are not widely used since they can lead to worse numerical stability of the solution [68].

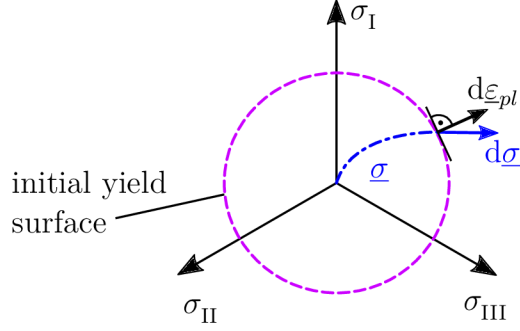


Figure 2.5: Illustration of associative flow rule

Hardening Rule

The hardening rule governs the change of the material strength after yielding, i.e. how the yield surface changes with the elasto–plastic loading. The hardening rule allows the calculation of the plastic multiplier which governs the magnitude of plastic flow [68]. There are 3 hardening groups:

Isotropic hardening. Isotropic hardening is increasing or decreasing the size of the yield surface in Haigh–Westergaard space. This is depicted in Figure 2.6, where σ_A is a generic value of stress larger than σ_0 . It is important that the boundary surface of plasticity does not move as whole [68]. It can be observed that the reverse loading is overpredicted. The isotropic hardening does not describe Bauschinger’s effect well, however it can describe the cyclic hardening/softening (depicted in Subsection 3.2.2). Isotropic hardening substitutes the term σ_0 in Equation 2.1 with a linear or non-linear function describing the hardening. For example, Voce is one of the most widely-used and commercially implemented non-linear relationships for isotropic hardening [15].

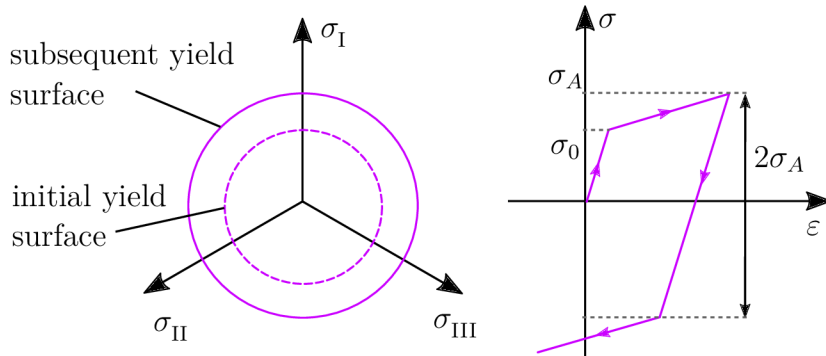


Figure 2.6: Illustration of linear isotropic hardening [15], left – in Haigh–Westergaard space, right – in the form of a stress–strain curve

Kinematic hardening. Kinematic hardening moves the yield surface as a whole in Haigh–Westergaard space, and it does not change its size [68]. The behavior is depicted in Figure 2.7. It can be observed that kinematic hardening describes Bauschinger’s effect well, however it cannot model the cyclic hardening/softening. However, as later stated, the cyclic hardening/softening is often neglected and only a representative hysteresis loop is used for calculation. A kinematic hardening material model is used in the practical part of this thesis, therefore it is described in further detail.

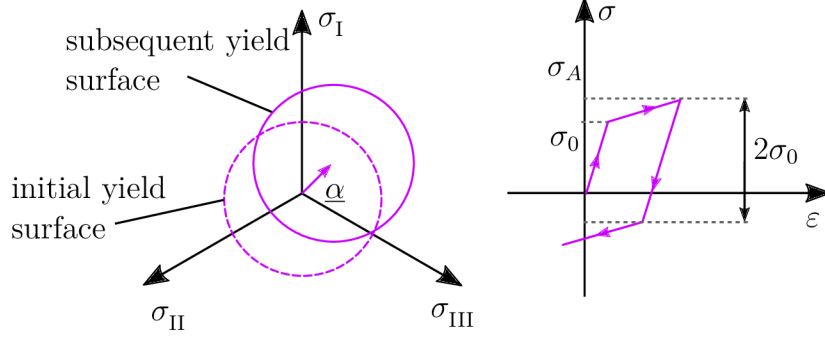


Figure 2.7: Illustration of linear kinematic hardening [15], left – in Haigh–Westergaard space, right – in form of stress–strain curve

The von Mises yield criterion is modified to [35]:

$$F = \sqrt{\frac{3}{2}(\underline{S} - \underline{\alpha}) : (\underline{S} - \underline{\alpha})} - \sigma_0 = 0 \quad (2.3)$$

where $\underline{\alpha}$ is the so-called backstress (tensor, describing the location of the center of the yield surface) [35].

At first, a linear kinematic hardening material model was introduced by Prager [4]. Prager is the simplest kinematic hardening model. In this case, the backstress is linearly related to plastic strain [4, 35]:

$$d\underline{\alpha} = \frac{2}{3}C d\underline{\varepsilon}_{pl} \quad (2.4)$$

where C is the additional material parameter, equal to the plastic modulus and proportional to the tangent modulus E_T .

A non-linear kinematic hardening model was proposed by Armstrong & Frederick [6]. The non-linearity is included by expanding the Equation 2.4 for backstress with the so-called recall term (also called the dynamic recovery term):

$$d\underline{\alpha} = \frac{2}{3}C d\underline{\varepsilon}_{pl} - \gamma \underline{\alpha} d\hat{\varepsilon}_{pl} \quad (2.5)$$

Where C and γ are material parameters and $\hat{\varepsilon}_{pl}$ is the accumulated plastic strain.

Chaboche et. al [8] proposed to perform a superposition of several Armstrong & Frederick non-linear rules:

$$\underline{\alpha} = \sum_{i=1}^k \underline{\alpha}_i \quad (2.6)$$

$$d\underline{\alpha}_i = \frac{2}{3}C_i d\underline{\varepsilon}_{pl} - \gamma_i \underline{\alpha}_i d\hat{\varepsilon}_{pl} \quad (2.7)$$

where k is the number of backstresses. The superposition is demonstrated in Figure 2.8 [35, 36]. The meaning of the constants is also depicted. Note that the last parameter γ_k is set to zero when the ratcheting is not considered. The Chaboche model can be expanded by viscous terms or temperature dependency as later described in Subsection 3.3.1.

Additionally, the rheological schema for kinematic hardening models was created on the basis of [48] in Figure 2.9, where ε_{el} and ε_{pl} are elastic and plastic strain.

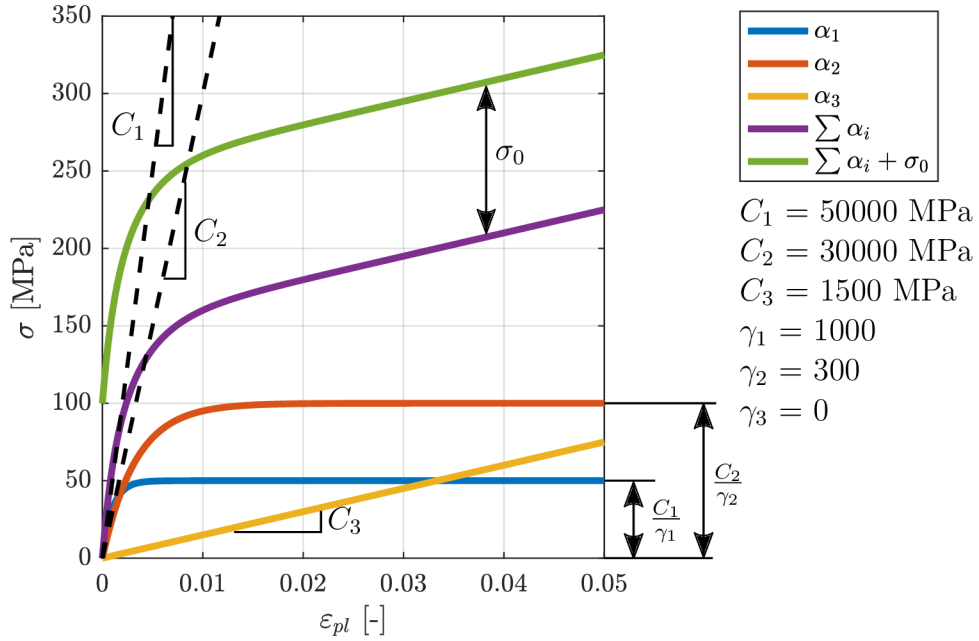


Figure 2.8: Decomposition of Chaboche model for $k = 3$ for illustration purposes, inspired by [35, 36]

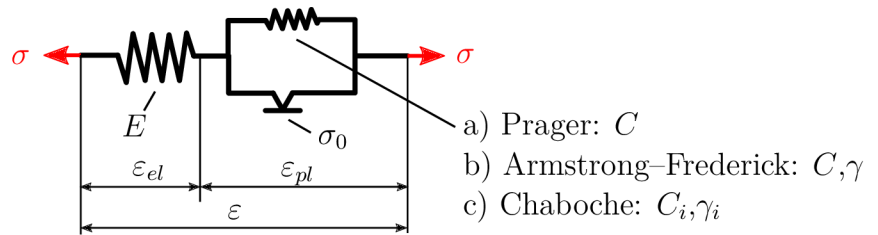


Figure 2.9: Rheological schema for kinematic hardening models [48]

Combined hardening. This model can describe both Bauschinger's effect and cyclic hardening/softening. One of the popular non-linear combinations is Chaboche's kinematic hardening + Voce's isotropic hardening. The yield surface moves as a whole (its center described by backstress $\underline{\alpha}$) and also increases/decreases its size. Similarly, the term σ_0 in Equation 2.3 is replaced by the linear or non-linear relationship prescribing the isotropic hardening. The behavior is depicted in Figure 2.10, where the isotropic hardening is denoted by Y .

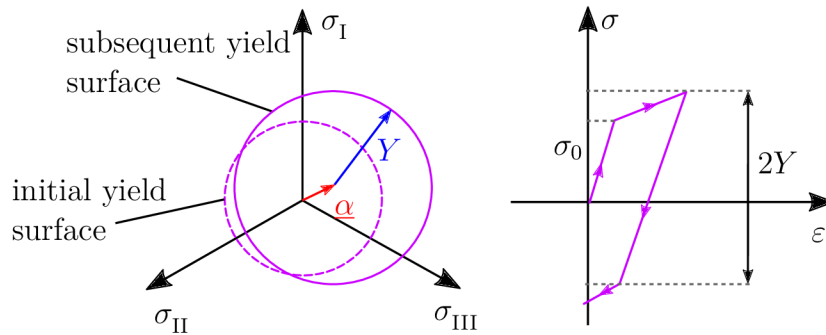


Figure 2.10: Illustration of linear combined hardening [36], left – in Haigh–Westergaard space, right – in form of stress–strain curve

2.1.2. Oxidation

Apart from fatigue damage, environmental damage (i.e. oxidation) also contributes to TMF at high temperatures. A deep investigation of oxidation, as a 2nd damage mechanism, was done by Neu and Sehitoglu in [9, 10]. They performed various tests (isothermal and both in-phase and out-of-phase non-isothermal tests – see Section 3.2) in air and in helium atmospheres. Testing in an inert atmosphere is one way of separating the environmental from creep and fatigue damage. The study concluded that the fatigue life was 2 to 12 times greater in helium than in air, hence oxidation plays a significant role in TMF. At high temperatures, an oxide layer appears on the surface of the specimen. Several types of oxidation damage mechanisms have been observed [9]:

- intensified crack nucleation and crack growth by brittle surface oxide scale cracking
- intergranular cracking caused by grain boundary oxidation
- preferential oxidation of second-phase particles

Typically, fatigue and oxidation interact, causing shorter life than either of them acting separately [9]. The oxide layer is subjected to mechanical strain. A tensile load can cause brittle oxide to fracture while a compressive load can cause buckling of the oxide or complete separation of the oxide scale, the so-called spallation. The tensile loading is more critical, because the repeated oxide fracture can guide the crack into the material [9]. Neu and Sehitoglu developed a fatigue life model for the oxidation in [10].

However, when the uniaxial tests are performed in ambient air, it is often assumed that the oxidation effects are accounted for in the prediction indirectly, and only fatigue and creep damage are taken into account [65, 70]. The same assumption is applied in the practical part of this thesis.

2.1.3. Creep

The creep is the 3rd major damage mechanism contributing to TMF failure. Creep can be defined as the development of inelastic strain in time, under a constant load, at increased temperatures. Hence the inelastic strain is a function of stress, time and temperature. It is a diffusion-driven process. There are 3 creep stages: primary, secondary and tertiary, depicted in the typical creep curve in Figure 2.11 a) [82], where ε_{creep} is the creep strain and T is temperature. The most important stage for the exhaust manifold subjected to TMF is the secondary stage – higher loads and shorter dwell times [14, 21, 49, 61, 64, 70]. The secondary stage is the longest portion of the creep curve, with the steady state strain rate $\dot{\varepsilon}_{ss}$ depicted in Figure 2.11 b), where $\dot{\varepsilon}_{creep}$ is the strain rate related to the creep. Figure 2.11 c) shows the so-called creep mechanism map, where G is the shear modulus used for normalizing the stress axis and T_{melt} is a melting temperature used for normalizing the temperature axis. The mechanism which is in the exhaust manifold subjected to TMF (the highlighted area of the map) is the so-called *dislocation climb* (also a diffusion driven mechanism). In contrast, the *diffusion creep* mechanism can be found in applications such as power plant applications (e.g. pipes under low stresses and a very long operating time). The stress and temperature dependency of the steady state strain rate $\dot{\varepsilon}_{ss}$ is described most commonly by Norton's exponential law (linear in the log–log coordinates) [82]:

$$\dot{\varepsilon}_{ss} = A_N \sigma^{n_N} \exp\left(-\frac{Q_N}{RT}\right) \quad (2.8)$$

where n_N is the Norton's creep exponent, A_N is the prefactor of the equation, R is the universal gas constant and Q_N is the activation energy. Hence creep describes the viscous behavior of the material. The A_N and n_N can be fitted in the log–log coordinates from the stress–strain rate curve. It is a linear line in such coordinates, hence n_N is the slope of the line and A_N is the intercept as depicted in Figure 2.12 a). The Q_N is proportional to the slope of the $\dot{\epsilon}_{ss}$ in the semi-natural logarithm coordinates from the temperature–strain rate curve shown in Figure 2.12 b) [82]. Norton's equation is typically used in the TMF modelling [17, 21, 27, 45, 47, 67, 70, 71].

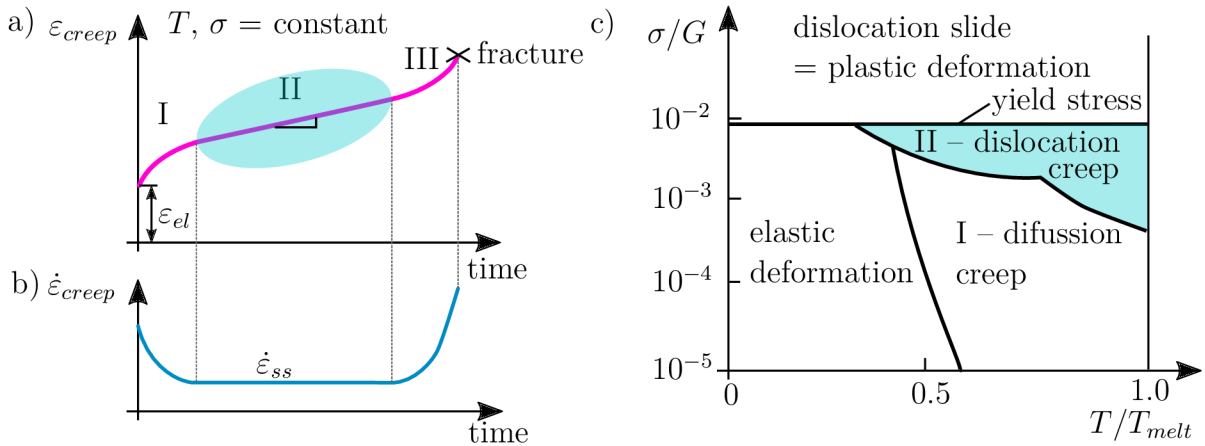


Figure 2.11: a) Illustration of the typical creep curve [12, 82], b) illustration of the typical corresponding strain rate [12], c) creep deformation mechanism map [82]

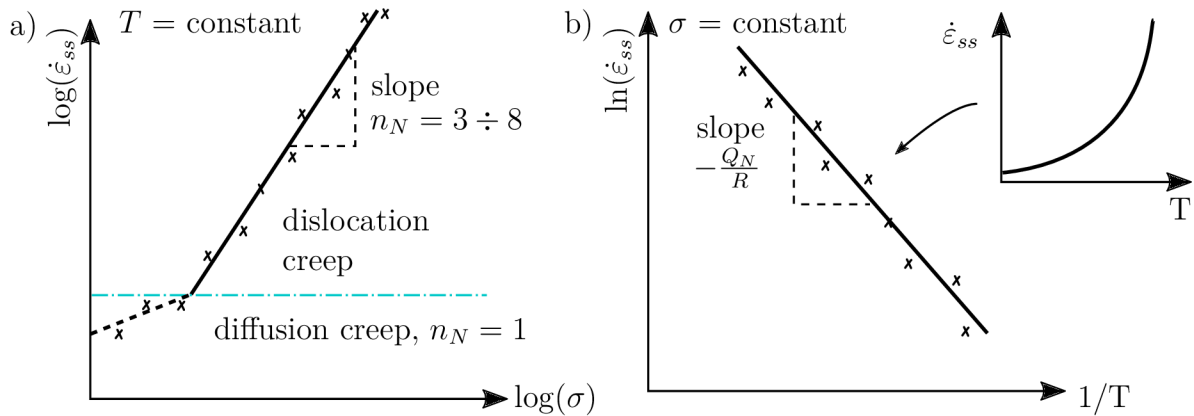


Figure 2.12: Illustration of the determination of the secondary creep parameters: a) creep strain rate curve in stress–strain rate logarithmic coordinates – identification of A_N and n_N ; b) creep strain rate curve in temperature–strain rate semi-natural logarithm coordinates – identification of Q_N [82]

In the practical part of this thesis, the creep effects are not taken into account as the experimental data were not available. The same approach in the case of exhaust manifold TMF analysis was done in [20, 55]. However, creep plays a significant role in the TMF predictions. This is a major drawback of this thesis and a possibility for further research.

3. High Temperature Components in Combustion Engines – Hot End

The exhaust system of the combustion engine starts from the engine head with the exhaust manifold, connected to the turbine side of the turbocharger (optional), succeeding the catalytic converter, particulate filter (optional) and muffler, and ending with the tail pipe. Additional components, such as the exhaust gas recirculation valve or resonators, can also be present. The components of the so-called hot end of the exhaust system are considered to be the exhaust manifold and the turbine side of the turbocharger (sometimes also a catalytic converter). The hot end components experience the most extreme operating conditions. The ongoing emissions legislation demands more efficient engines, furthermore the trend is to increase the power of the engine while maintaining low fuel consumption. Both of these demands result in higher exhaust gas temperatures [42]. Therefore, state-of-the-art materials are used in such applications. Figure 3.1 shows the real hot end of the combustion engine, where the components glow due to the extreme operating temperatures.

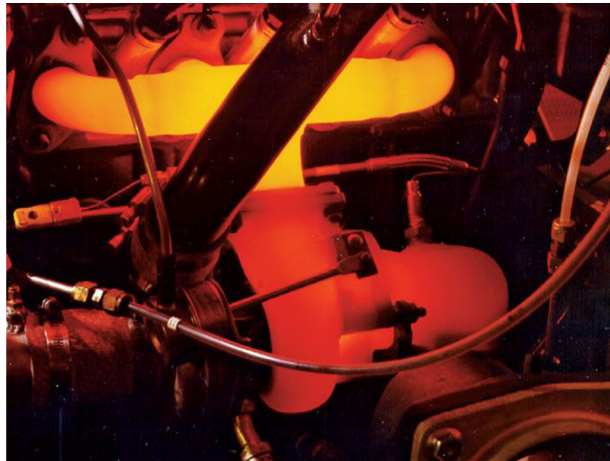


Figure 3.1: The hot end of the exhaust system (the exhaust manifold and the turbine side of the turbocharger) glowing due to extreme temperatures [83]

3.1. Heat Resistant Casting Materials in the Hot End

Generally, the alloys used for the castings of the engine's hot end can be divided into 4 groups as per Figure 3.2 [42, 62]. The general demands for the materials are good castability, low cost, low weight, corrosion resistance and appropriate high temperature mechanical properties. Also, when the material has a low thermal expansion coefficient and high thermal conductivity, the strains induced by thermal cycling can be reduced, hence these physical properties are also important [42].

The most common and widely used is the **ferritic ductile cast iron** group. These alloys contain a high amount of carbon in spherical form, resulting in a low melting point and high fluidity, which is beneficial for the castability. The Silicon–Molybdenum (SiMo) family is typically used in diesel applications up to the exhaust gas temperature $T_1=750^{\circ}\text{C}$. This alloy disposes with low cost [42, 43, 65].

For the higher temperatures, the more expensive **austenitic ductile irons** can be used – namely the Ni-resist D5S grade, which is used in gasoline applications. The D5S has a higher strength compared to the SiMo, but has some limitations regarding corrosion resistance. This alloy has appropriate mechanical properties up to $T_1=850^\circ\text{C}$ [42].

The next is the **ferritic cast stainless steels** group. High-temperature mechanical properties and corrosion resistance are better compared to the previous groups. However, the carbon content is relatively low, resulting in poor castability. The low amount of carbon can also result in the presence of large grains in the microstructure, which is not beneficial for the fatigue life. Hence ferritic steels are often used in exhaust manifolds in the form of sheet metal produced by forming. However, ferritic cast steels were developed too – for example, the StarCast DCR3 alloy is used as a replacement for the Ni-resist D5S. The StarCast DCR3 was treated to have better castability and can be used in gasoline applications up to $T_1=900^\circ\text{C}$ [42].

The last state-of-the-art group are the **austenitic cast stainless steels**. These are used in the most critical and demanding operating conditions, where the ferritic alloys reach their limitations. These alloys contain mainly Cr and Ni alloying elements. The HK30 is one of the commercially-used austenitic cast steel alloys in exhaust manifold applications. This material can be used up to an exhaust gas temperature of $T_1=1000^\circ\text{C}$. Other alloy from this group, designated as CF8C-plus, is used as a less expensive variant [42]. Other alloys are from the so-called 1.48 family (e.g. 1.4848), which is also used in the gasoline hot end components (e.g. turbocharger turbine housings). The alloy can be used up to $T_1=1020^\circ\text{C}$ and sustains good castability, corrosion resistance and mechanical properties [62]. The cost of these components is naturally higher compared to the previous material groups [42].

Note that these are operating temperatures, which means that the material can sustain a higher T_1 but for a limited amount of time [42].

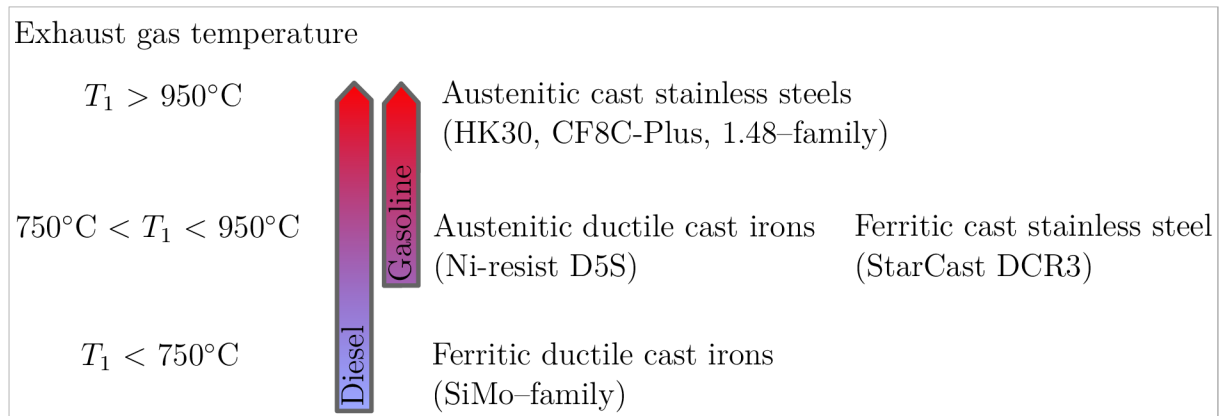


Figure 3.2: Approximate division of the material groups used in hot end components, with respect to exhaust gas temperature [42, 62]

3.2. Material Testing

Specific uniaxial tests on the specimen level (apart from the quasi-static monotonic tensile test) are frequently performed. These tests are used by material scientists for material development, as well as structural engineers for the development of material and fatigue life models in order to predict TMF life. Some of these tests and materials phenomena are listed in this section.

3.2.1. Tensile Test at Increased Strain Rate

Apart from the quasi-static tensile tests, the tensile tests with increased strain rate are performed. The purpose of these tests is to examine viscous behavior, mainly at elevated temperatures. In the tensile test, the higher the strain rate, the higher the stress response of the material. This aforementioned behavior can be seen, for example, in Figure 3.3; which was created from the real data in [69].

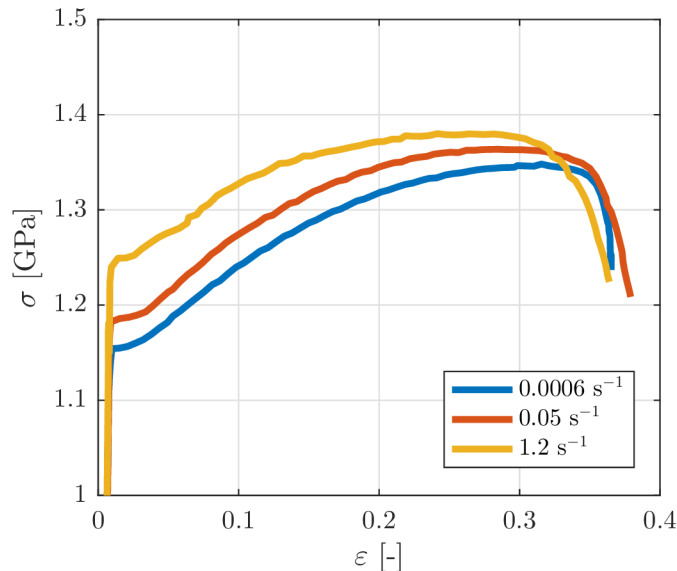


Figure 3.3: Typical response of the material for the strain rate increase – high specific strength steel, re-created from [69]

3.2.2. Low Cycle Fatigue Test

In order to calibrate the material model which describes the cyclic behavior, a hysteresis loop of the material must be obtained. This is done in a similar manner to the tensile test, on an unnotched cylindrical specimen with high surface quality. The cyclic tests are usually controlled by servohydraulic systems. The control quantities in the test can be either stress or strain. The shape of the hysteresis loop depends on the control mode (stress or strain controlled) and the load frequency [13].

The hysteresis loop in the form of σ - ϵ dependency carries the basic cyclic behavior of the material over each loading cycle. Unlike the monotonic loading, where we obtain a unique σ - ϵ dependency, a hysteresis loop is obtained every cycle. In addition, the hysteresis loop is often recalculated from total strain ϵ into plastic strain ϵ_{pl} coordinates

using Hooke's law in Equation 3.1 [13], where E is the Young's modulus. The elastic part of the hysteresis loop in plastic coordinates transforms into a vertical line [13].

$$\varepsilon = \varepsilon_{el} + \varepsilon_{pl} = \frac{\sigma}{E} + \varepsilon_{pl} \quad (3.1)$$

Some of the important quantities are taken directly from the hysteresis loop depicted in Figure 3.4. The maximum and minimum stress and strain of cycle $\varepsilon_{max}, \sigma_{max}, \varepsilon_{min}, \sigma_{min}$; mean stress or strain σ_m, ε_m ; stress and strain range (Δ) of the cycle $\Delta\varepsilon, \Delta\sigma$ – Equations 3.2, 3.3, 3.4, 3.5. The range of the plastic strain $\Delta\varepsilon_{pl}$ corresponds to the intersection of the loop with the strain axis. The amplitudes of the quantities are halves of the corresponding ranges of the quantities [13].

$$\Delta\sigma = \sigma_{max} - \sigma_{min} \quad (3.2)$$

$$\Delta\varepsilon = \varepsilon_{max} - \varepsilon_{min} \quad (3.3)$$

$$\sigma_m = \frac{\sigma_{max} + \sigma_{min}}{2} \quad (3.4)$$

$$\varepsilon_m = \frac{\varepsilon_{max} + \varepsilon_{min}}{2} \quad (3.5)$$

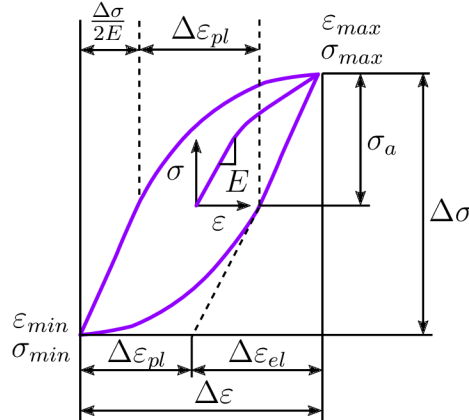


Figure 3.4: Evaluated quantities of the hysteresis loop [13]

The cyclic behavior of the hysteresis loop may be transient during the test. This is referred to as cyclic hardening, softening and other phenomena. Some of the examples of the transient behaviour are depicted in Figure 3.5, which was created on the basis of [13, 22, 25, 35]. Note that the specimen does not always have to be cylindrical, but for example in the case of ratcheting test, a tubular specimen is used [72].

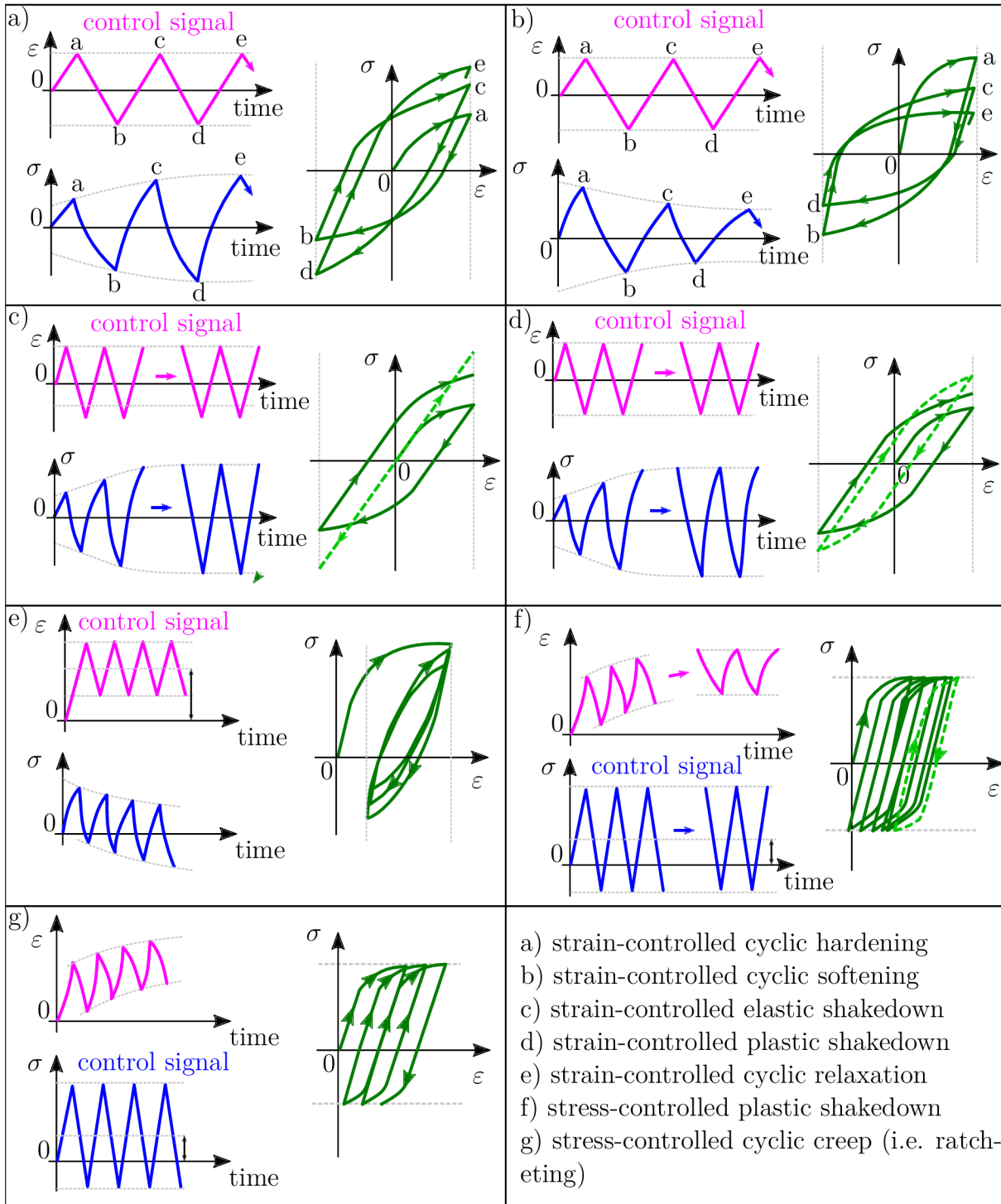


Figure 3.5: Some of the examples of transient cyclic behaviors [13, 22, 25, 35]

However, these transient effects (like hardening and softening) are often disregarded and the cyclic behavior is described by a representative loop [13]. Common practice is to take the representative loop from the half life to failure ($N_f/2$), however according to [13] it is up to the interpreter who should note at which point the saturated state was considered.

The cyclic stress–strain curve is another important curve. It is created by connecting the peaks in tension and compression from the stabilized hysteresis loops. An example of

the cyclic stress–strain curve is in Figure 3.6 [25]. This curve (depicted by the red line) can be described by the Ramberg–Osgood relationship from Equation 3.6 [3].

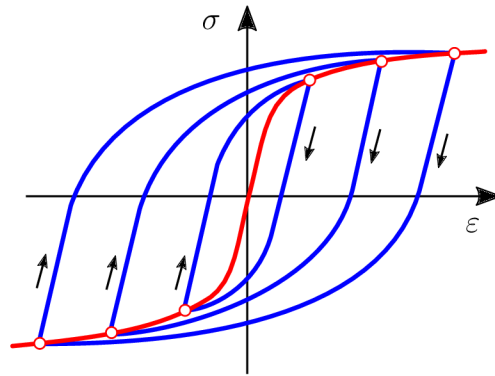


Figure 3.6: An example of cyclic stress–strain curve, depicted by the red line [25]

$$\varepsilon = \frac{\sigma}{E} + \left(\frac{\sigma}{K'} \right)^{\frac{1}{n'}} \quad (3.6)$$

where K' is the cyclic strength coefficient and n' is the cyclic strain hardening exponent. The cyclic stress–strain curve is compared to the monotonic one, in order to assess cyclically induced changes. The examples of cyclic behaviors compared to the monotonic ones are in Figure 3.7. There is a rule of thumb which can estimate whether the material cyclically hardens or softens – when the cyclic softening is expected, the ratio of ultimate strength and yield stress from the monotonic test is below 1.2, whereas for cyclic hardening this ratio is expected to be larger than 1.4 [13].

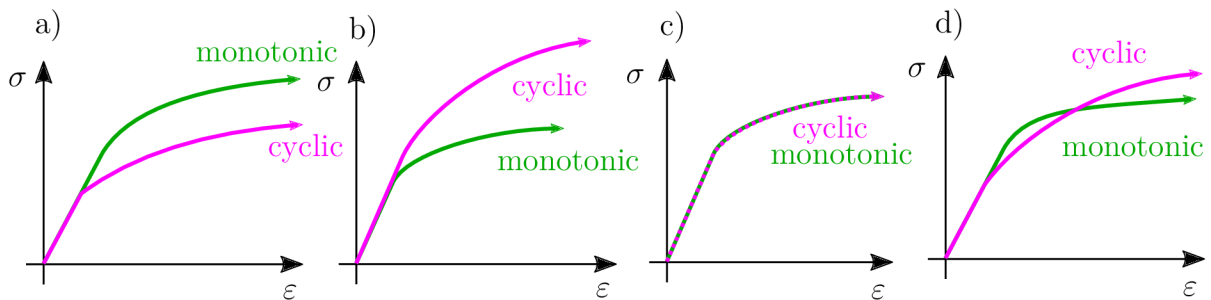


Figure 3.7: Examples of cyclic stress–strain curves compared to monotonic ones, created on the basis of [13]; a) cyclic softening, b) cyclic hardening, c) cyclically stable, d) mixed behavior

One important phenomenon that the material can exhibit is Masing behavior. This is when each stabilized loop follows the master curve (the origin of the stabilized loop is translated to compressive peak). The example is depicted in Figure 3.8.

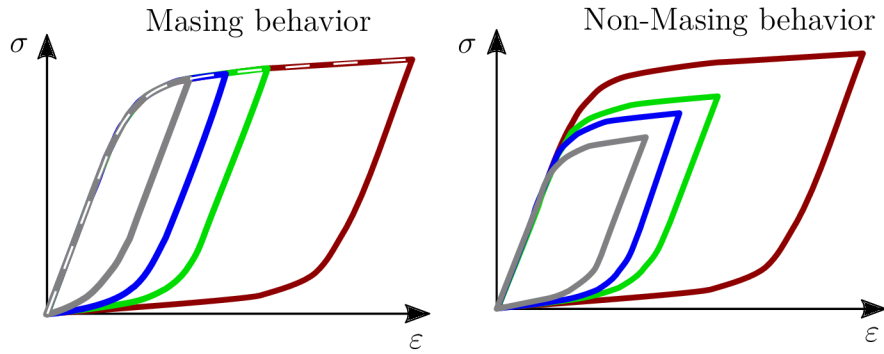


Figure 3.8: Example of Masing and non-Masing behavior [1]

Another typical test performed for the LCF at high temperatures is testing with a dwell period (the so-called creep-fatigue test). This test is used to examine the stress relaxation of the material and can be used for the calibration and validation of the visco-plastic material model and the static recovery term of the model. Both stress-strain and stress-time curves are used for the calibration [64, 70]. An example of such a test is in Figure 3.9. In this example of Ni-based alloy 230 at 850°C, the stress magnitude dropped by 80 % in a time of 1800 s. Note that this test can be again stress or strain controlled, hence the relaxation line can be either horizontal or vertical [12].

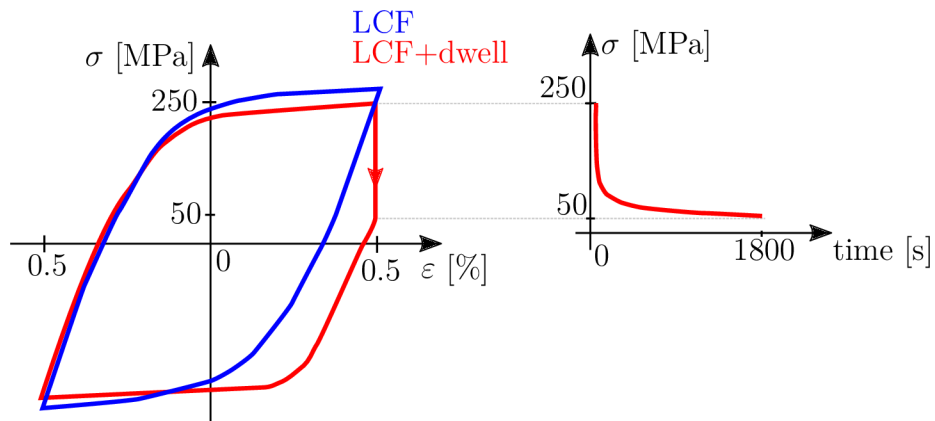


Figure 3.9: Examples of LCF test with a dwell period – Ni-based alloy 230 at 850°C, created on the basis of [64]

Additionally, a mean stress effect influences the fatigue life significantly. An example of this influence is in Figure 3.10 [25], where ϵ'_f is the fatigue ductility coefficient. Therefore, the mean stress corrections were proposed, and they are covered later in Section 4.3.

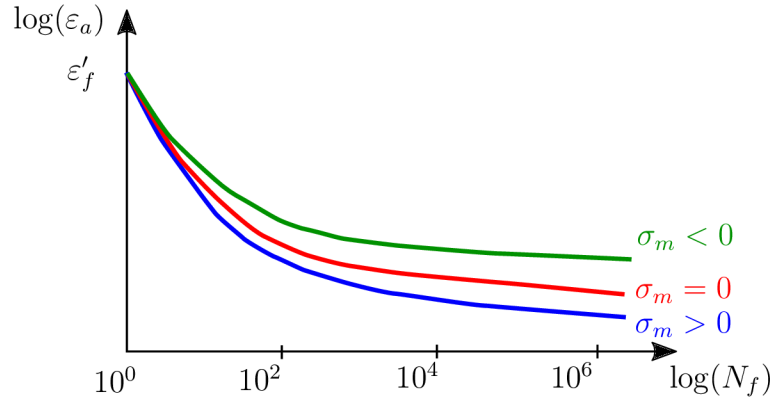


Figure 3.10: Example of mean stress influence on fatigue life [25]

The LCF tests can be done at increased strain rate, similarly to the tensile tests. The behavior is the same – the higher the strain rate, the higher the stress response is obtained. Again, the viscous behaviour of the material model is validated using such a test. This behavior can, for example, be seen in [70]. Apart from the uniaxial tests, multiaxial ones can also be performed. For example in [72], non-proportional multiaxial tests were performed for the LCF modelling.

3.2.3. Thermo–Mechanical Fatigue Test

The aforementioned LCF tests at a constant temperature are conventional Isothermal Fatigue (IF) tests. IF life data at the maximum operating temperature have been used in order to predict TMF. However, this approach results in non-conservative predictions [9]. The fatigue is caused not just by variation of the mechanical strain¹ ε^m , but also by the temperature variation. The mechanical strain occurs from either external constraints or from external loading. The IF is hence a special case of TMF. The fatigue cannot be predicted based on IF data, therefore TMF experiments are introduced. These tests were firstly reported in the 1950s by research groups in the United States, Europe and Japan. Nowadays the rise of computer control and servohydraulic testing machines have established accurate control of the temperature and strain, thus increasing the size of the research field. The database of TMF research is still small in comparison to the IF database, however. This is due to the fact that the TMF tests are significantly more difficult and expensive to conduct. The heating of the specimen is mostly done by resistance or induction. The temperature should be controlled by thermocouples and uniform along the gage length and diameter. [13, 60]. Only a strain-controlled variant of this test is known to the author based on the research. The standards for the TMF exists – ASTM E2368-10 and ISO 12111:2011 [67].

The TMF tests are classified based on the phase between ε^m and T . When the peak mechanical strain coincides with the maximum temperature, the test is called In-Phase Thermo–Mechanical Fatigue (IPTMF) (0° phase shift). On the other hand, an Out-of-Phase Thermo–Mechanical Fatigue (OPTMF) test has the peak mechanical strain

¹It is necessary to distinguish the thermal and mechanical strain in TMF tests. Total strain is described by Equation 4.1. The author denotes mechanical strain with ε^m only regarding the TMF tests (i.e. in Subsections 3.2.3 and 4.1.3). Otherwise in any other conditions, thermal strains are equal to zero, hence total strain ε is equal to mechanical strain ε^m .

coinciding with the minimum temperature (180° phase shift) [13]. The control quantities ε^m and T of both tests are plotted in Figure 3.11, as well as the stress responses. The hysteresis loops are not balanced in tension and compression. For the OPTMF tests, the inelastic strains are developed more in compression than in tension. The IPTMF tests exhibit the opposite behavior [13]. The strain ratio (sometimes called constraint) $R_{\varepsilon^m} = -\frac{\varepsilon_{min}^m}{\varepsilon_{max}^m}$ of the cycle can be calculated. According to [13] the tests are typically conducted with $R_{\varepsilon^m} = -1$ (fully reversed), $R_{\varepsilon^m} = 0$ (minimum mechanical strain is zero) and $R_{\varepsilon^m} = -\infty$ (maximum mechanical strain is zero). In the practical part of this thesis, an OPTMF test with $R_{\varepsilon^m} = -\infty$ was used for the material model validation (Subsection 4.1.2).

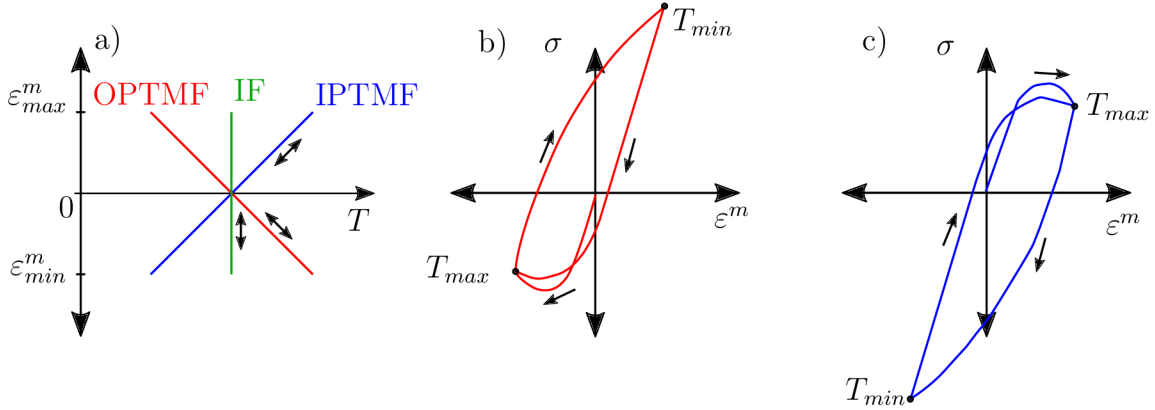


Figure 3.11: a) Variation of ε^m and T for IPTMF, OPTMF and IF tests, b) σ response for OPTMF test, c) σ response for IPTMF test, re-created on the basis of [13]

The stress range $\Delta\sigma$ and mechanical strain range $\Delta\varepsilon^m$ is depicted for the OPTMF test case in Figure 3.12. Note that for the OPTMF test, at ε_{min}^m (point B), the stress magnitude is not necessarily a minimum one. Usually, there is an inelastic deformation with softening between points A and B, which is caused by strength decrease with increasing temperature. At point B, a maximum temperature is achieved. Then the cooling succeeds with elastic deformation, followed by the plastic one until the lowest temperature is achieved (point C) [13]. This behavior can be observed later in Subsection 4.1.2 on experimental data. For the IPTMF test, the behavior is in the same manner, but reversed [13].

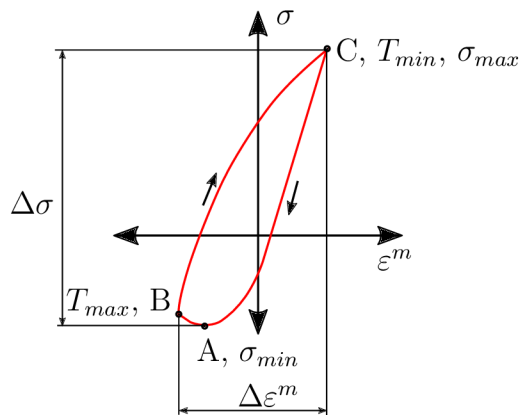


Figure 3.12: Stress and mechanical strain range with important points in OPTMF hysteresis loop, re-created on the basis of [13]

Similarly to IF tests, the hysteresis loops in TMF tests can cyclically harden or soften. This behavior is influenced by the material microstructure and the test conditions, such as maximum temperatures or phase shifting. By calculating the mean stress σ_m using Equation 3.4 in each cycle, a mean stress evolution can be captured and evaluated. It is another important quantity, which describes the saturation of the TMF test and influencing the fatigue life [60]. The cyclic behavior can be complex, however, due to temperature–strain interaction. The material can behave differently at T_{max} and T_{min} , meaning it can cyclically harden, soften or be stable [13]. Two variants have been plotted on the basis of [13] in Figure 3.13 as an example of OPTMF response. Variant a) shows material which cyclically softens at T_{max} and stays stable at T_{min} . This can happen due to thermal recovery which causes a coarser microstructure. The overall stress range decreases in this variant. Variant b) shows material which is stable at T_{max} and hardens at T_{min} . The hardening at T_{min} can be caused by dynamic or static strain–aging effects. The overall stress range increases in this variant. Another complex TMF behavior was described in [67]. Liu et al. encountered a sudden stress decrease, probably caused by a change in magnetic property at Curie temperature (around 720°C). Generally, there are material phenomena (intergranular embrittlement, phase changes, etc.) which are not captured in the material modelling, but they exist in the applications. These phenomena can carry useful information for the failure analysis [67].

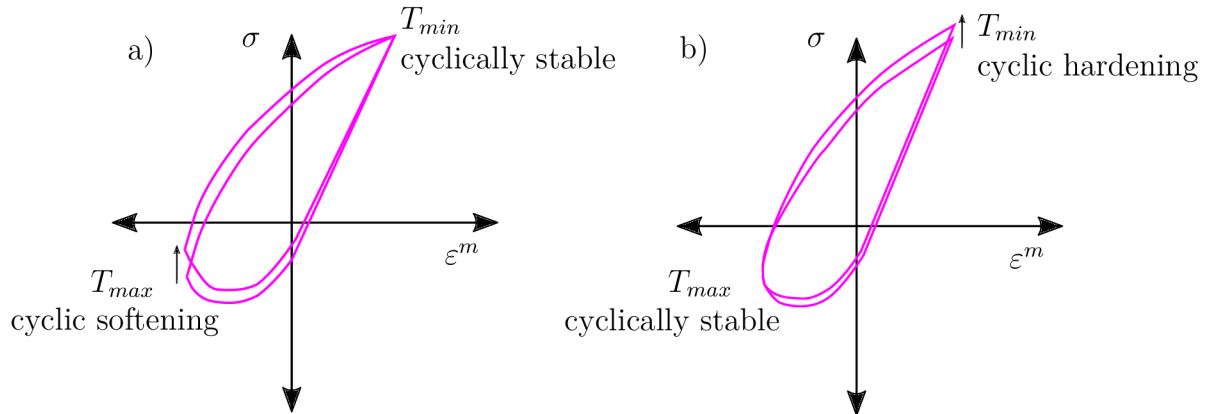


Figure 3.13: Example of cyclic behaviour response for OPTMF test [13]

Furthermore, the TMF tests can be conducted with dwell periods, the same as the IF tests. Such tests can be used for the calibration and validation of rate-dependent material models. Typically, the stress relaxes through creep deformation in the dwell time, leading to the investigation of creep–fatigue interaction [60]. An example of such a test is plotted in Figure 3.14.

Another variant of the TMF tests are the so-called diamond (sometimes called baseball) modifications. These variants are done by shifting the phase between ε^m and T by 90° or 270°. Then, the controlling path can be in a clockwise direction – Diamond Clockwise (DCW) or counterclockwise – Diamond Counterclockwise (DCCW). The direction also influences TMF life [13]. According to [13], in many alloys the DCW and DCCW tests were not as damaging in comparison to IPTMF and OPTMF. This is due to the fact that the T_{max} , ε_{max} and σ_{max} does not occur at the same time. An example of DCCW is in Figure 3.15 a) ε^m and T variation and b) the stress response.

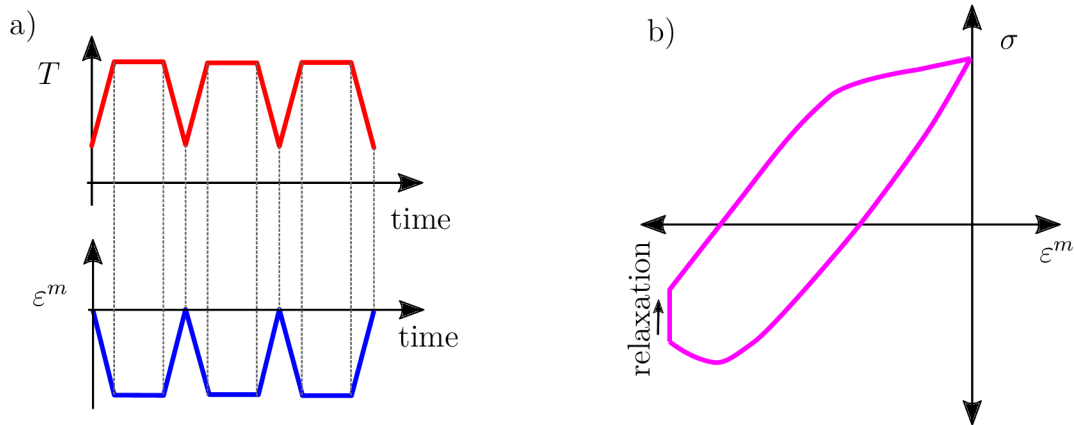


Figure 3.14: Example of OPTMF with dwell periods, a) control quantities, b) stress response, re-created from [60]

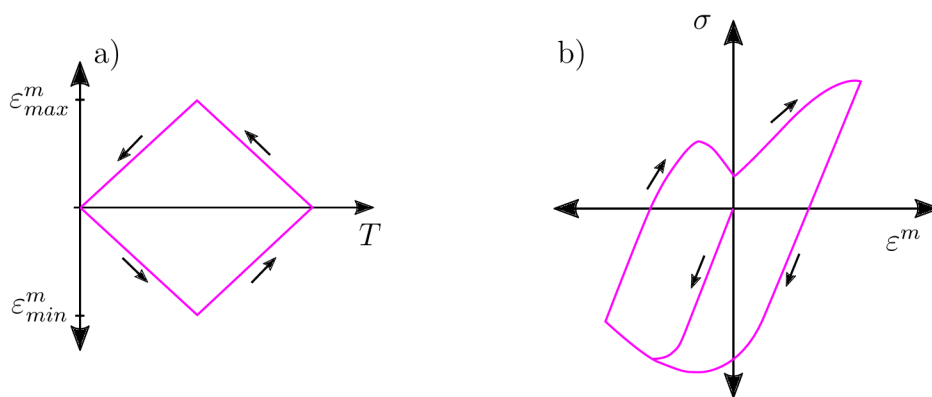


Figure 3.15: Example DCCW test, a) control quantities, b) stress response, re-created from [13]

3.2.4. Complex Low Cycle Fatigue Test

Another effective possibility for testing the behavior of materials in the LCF regime is the Complex Low Cycle Fatigue (CLCF) test [47, 49, 61, 64, 56]. The CLCF test is isothermal and typically consists of both non-periodical and periodical parts. Dwell times and various strain rates are used in the non-periodical parts, whereas a constant strain rate is used in the periodical part, until specimens fail. The intention of this test is to raise various material phenomena, such as strain rate effects, stress relaxation and cyclic hardening in one single experiment [49]. Therefore, the efforts for the number of physical specimens and costs can be reduced. An example of the CLCF test is in Figure 3.16. This test can also be used for obtaining more robust results of calibration of the material model [56] as further mentioned in Subsection 4.1.3.

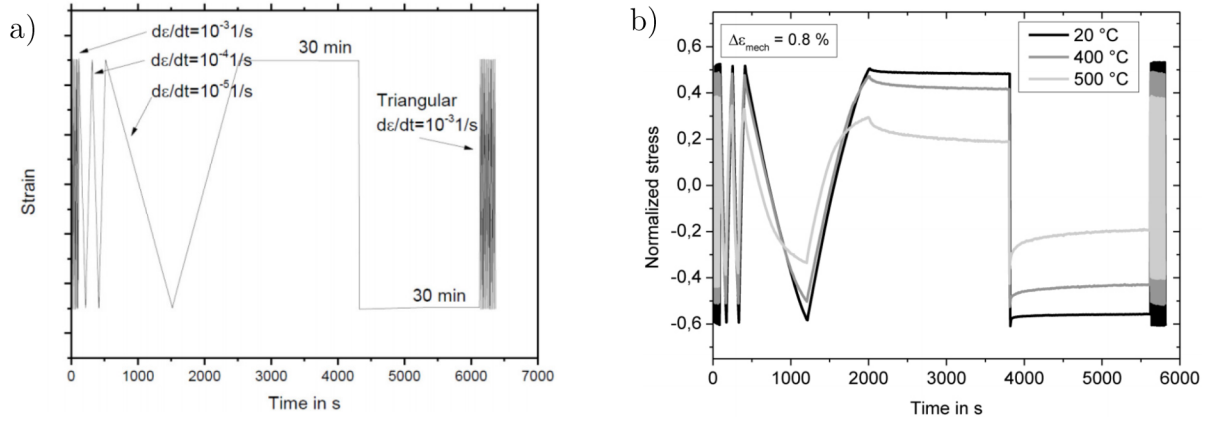


Figure 3.16: Example of CLCF test, a) control quantities, b) stress response [49]

3.2.5. Creep Test

Apart from the damage caused by mechanical loading (i.e. cyclic plasticity), creep is another important mechanism present in TMF, directly contributing to the damage of the material (as described in Section 2.1) [13]. To be able to model the creep behavior in TMF, the creep-rupture data must be known across the whole stress and temperature range of the component. However, the creep-rupture characteristics evaluated at low stresses and temperatures can exceed 10^5 h. Naturally, this is unacceptable for engineering purposes due to the immense amount of time and expense. Hence, it is a common practice to evaluate the behavior at high temperatures and stresses, and to extrapolate to low ones using the time-temperature parameters (Larson-Miller, Manson-Hafnerds, Sherby-Dorn, Restrained Manson-Brown, etc.). Each of these parameters is based on the different family of the so-called master curve [34, 70]. The example of the creep test's sensitivity to control quantities is in Figure 3.17 a) and the master curves are in Figure 3.17 b)[34, 70].

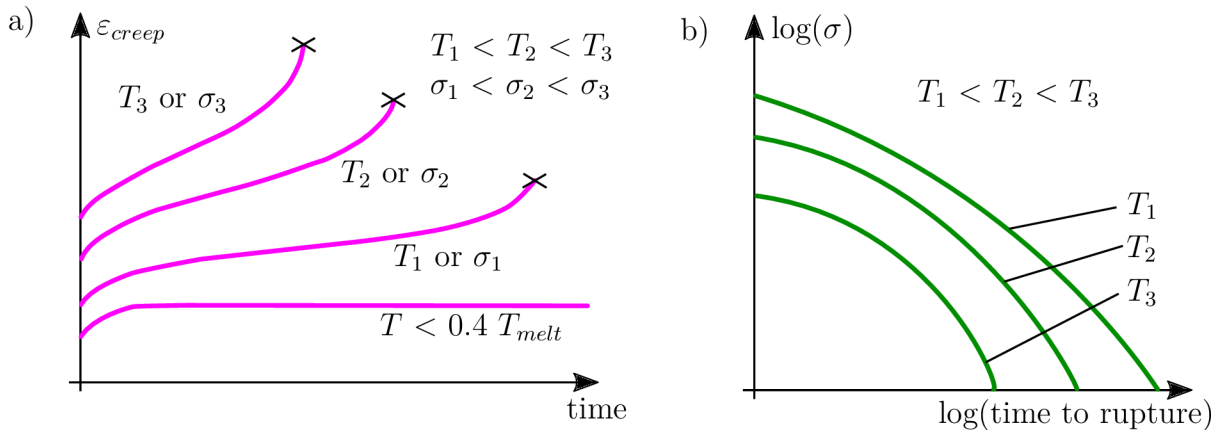


Figure 3.17: a) Typical behavior in a creep test for T or σ variation [12], b) example of master curves used for extrapolation [34, 70]

3.3. Algorithm of Thermo–Mechanical Fatigue Life Prediction

The approaches of the component TMF life prediction were researched. Based on the research from [14, 17, 18, 20, 21, 27, 33, 37, 38, 40, 45, 47, 49, 51, 55, 61, 63, 64, 67, 70], it was idealized into an algorithm, depicted in form of flowchart in Figure 3.18, in which T_{bulk} is the bulk temperature, HTC is the heat transfer coefficient, FEA means Finite Element Analysis, CFD means Computational Fluid Dynamics, CHT means Conjugate Heat Transfer and BC means Boundary Conditions. This algorithm was applied in Chapter 4. It is evident that the experiments on both a specimen and component level are essential for the correct fatigue life prediction. Tests conducted on a specimen level are used for the material and fatigue life model development, whereas the component tests serve for calibration and validation of the numerical model. The component tests are depicted by blue boxes. Ideally, these are conducted at least in the first and last simulation loop. As there were no resources for this thesis and the case serves only to demonstrate the workflow, no component tests have been conducted.

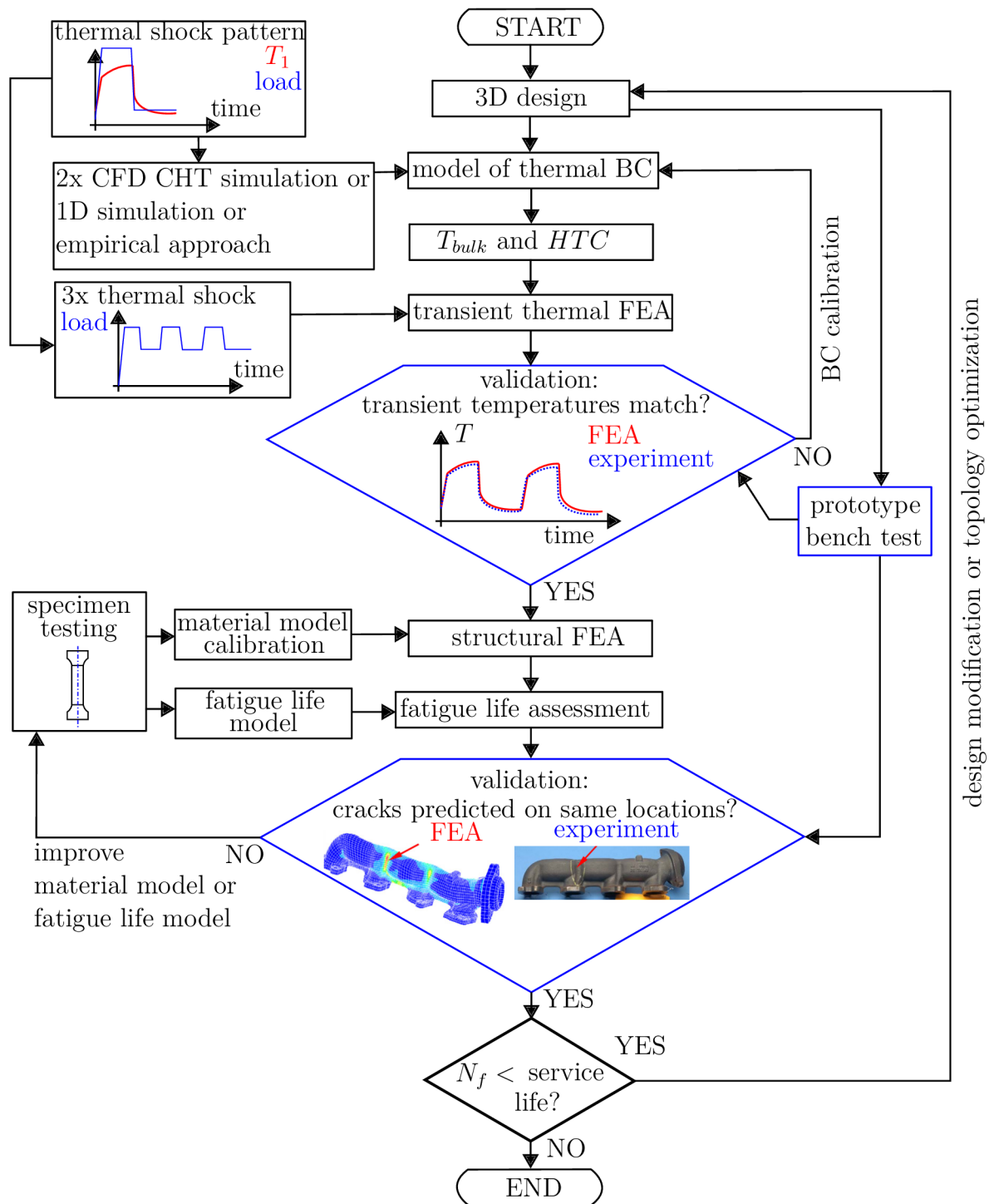


Figure 3.18: Idealized flowchart of the TMF life prediction algorithm, including the manual or automated optimization loop; based on [14, 17, 18, 20, 21, 27, 33, 37, 38, 40, 45, 47, 49, 51, 55, 61, 63, 64, 67, 70]

3.3.1. Overview of Used Material Models

Several types of temperature-dependent material models, which are capable of describing most of the phenomena from Section 3.2, have been used. Typically, viscoplastic material models are suitable for the TMF life predictions. This is a state-of-the-art group of cyclic plasticity models. The most frequently used viscoplastic material models in the hot end components subjected to TMF applications are [48, 67]:

Non-Unified Creep and Plasticity Models

The non-unified models calculate the creep and plasticity separately [73]. The rheological schema is in Figure 3.19 a), where ε_v is viscous strain [48]. It is evident that the viscous damper is in series with plasticity, hence the creep and plasticity do not interact. A material model with Chaboche combined hardening, Norton's and hyperbolic sine creep law in series was used in [45].

The Two-Layer Visco-Plastic Model

In unified models, the creep and plastic deformation are coupled [73]. The Two-Layer Visco-Plastic model (2LVP) can be considered as a unified model and has been used in [17, 47, 67, 70]. However, in contrast to typical unified models, the 2LVP model expresses the deformation by two parallel networks – elasto-plastic and visco-elastic [16, 67]. Some authors distinguish it from the unified models and consider it as a separate group (e.g. [16]). The kinematic hardening is often based on Chaboche non-linear kinematic hardening (meaning the backstress is a superposition of Armstrong-Frederick models as covered previously). In the 2LVP model, the viscous damper is usually described by Norton's law [17, 47, 67, 70]. The 2LVP model is implemented in Abaqus commercial FE software. The rheological schema is depicted in Figure 3.19 b), where $E_{(pl)}$ is the elastic modulus in elasto-plastic network, $E_{(v)}$ is elastic modulus in visco-elastic network. Hence there is the presence of elastic strain in elasto-plastic network $\varepsilon_{el(pl)}$ and elastic strain in the visco-elastic network $\varepsilon_{el(v)}$. The overall strain is computed using following equations:

$$\varepsilon = \varepsilon_{el(v)} + \varepsilon_v = \varepsilon_{el(pl)} + \varepsilon_{pl} = \varepsilon_{el} + \varepsilon_{vp} \quad (3.7)$$

$$\varepsilon_{el} = f\varepsilon_{el(v)} + (1 - f)\varepsilon_{el(pl)} \quad (3.8)$$

$$\varepsilon_{vp} = f\varepsilon_v + (1 - f)\varepsilon_{pl} \quad (3.9)$$

$$f = \frac{E_{(v)}}{E_{(pl)} + E_{(v)}} \quad (3.10)$$

where f is a ratio of elastic modulus in the visco-elastic network out of the elastic modulus of the whole material [67]. It can be concluded, that the plasticity and creep interact, resulting in the visco-plastic strain ε_{vp} . The calibration of this model is explained in [67].

Unified Creep and Plasticity Models

This is another family of unified models. However, these models do not describe the creep and plasticity in two parallel networks, but the damper is in parallel with kinematic hardening, as per Figure 3.19 c), where the rheological schema have been depicted. Typically, Chaboche-based models are the most frequently used. Seifert et al. used the visco-plastic version of the Chaboche model for 2 backstresses, coupled with Norton's law for creep effects – [21, 27] with cyclic hardening and [47, 71] without cyclic hardening but with static recovery. Studies have shown that the unified viscoplastic formulation of the Chaboche model gives a better description of stress relaxation compared to the 2LVP model [47]. However, due to the more complex coupling of the creep and plasticity, the identification of the model parameters is more demanding [16]. The Chaboche model coupled with Norton's creep law was also used in [23].

As seen in Figure 3.19 c), the plasticity and creep also interact, resulting in ε_{vp} . The model can expand the formulation by static recovery term (meaning a decrease of the hardening with time) [47]. The Exponential Visco-Hardening (EVH) model, which has been adressed for the TMF modelling of hot end components in [64], and implemented in ANSYS commercial FE software, is another extension of this model. In the case of the EVH model, the damper is a superposition of individual dampers – the so-called multi-layer effect. Apart from the non-linear kinematic hardening, a unified visco-plastic model with a linear kinematic hardening has been used in [17, 63].

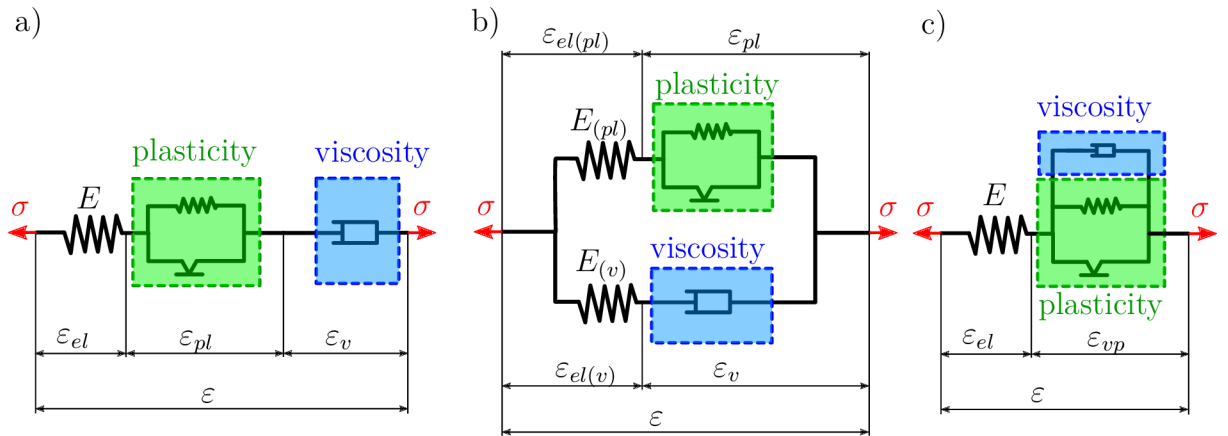


Figure 3.19: Rheological schemas of a) the non-unified visco-plastic model [45], b) the 2LVP model [16, 67], c) the unified (Chaboche) visco-plastic model [16, 48]

Other Models

Apart from the aforementioned families, other kinds of material models have been used regarding the hot end components subjected to TMF. They also include rate-independent models:

- Combined hardening with time hardening creep [18].
- A linear elastic model [20]. However, only a quantitative component stress analysis was performed, without TMF life prediction.
- An overlay model [38].
- A rate-independent linear kinematic hardening model [55].
- A rate-independent Chaboche model [29, 33]. The calculation of creep effects was done in post-processing by means of correction methods.

In the practical part of this thesis (Chapter 4), two rate-independent material models were used as the creep properties were absent. Both models were temperature-dependent. These models are underlined in the previous list with corresponding references. At first, a linear kinematic hardening has been used. The same model has been used in the same application in [55] as mentioned previously. This model has a backstress definition by Prager expanded by the temperature term. It is described in Equation 3.11 (which is Equation 2.4 + temperature dependency term). Secondly, Chaboche non-linear kinematic hardening model has been used. The same model has been used in the same application in [29, 33]. Similarly, Chaboche non-linear kinematic hardening backstress increment expanded by the temperature term is in Equation 3.12 (which is Equation 2.7 + temperature dependency term) [35].

$$d\underline{\alpha} = \frac{2}{3}C(T)d\underline{\varepsilon}_{pl} + \frac{1}{C(T)}\frac{\partial C(T)}{\partial T}\underline{\alpha}dT \quad (3.11)$$

$$d\underline{\alpha}_i = \frac{2}{3}C_i(T)d\underline{\varepsilon}_{pl} - \gamma_i(T)\underline{\alpha}_i d\hat{\varepsilon}_{pl} + \frac{1}{C_i(T)}\frac{\partial C_i(T)}{\partial T}\underline{\alpha}_i dT \quad (3.12)$$

As the field evolves rapidly, there are several other phenomena which have not been extensively covered – kinematic static recovery, memory of prior deformation, material aging, etc. These effects are omitted and could be a part of further research. A number of new models have been proposed and usually validated on the basis of uniaxial tests. However, the author was mainly searching for models which have been used in the hot end component analyses. Also, it is questionable up to which point the increased complexity of the material model, and the effort spent on the identification of an increased number of unknown parameters bring a recognizable improvement in fatigue life prediction on the component level.

3.3.2. Overview of Used Fatigue Life Models

Similar to the material models, an overview of fatigue life models used in the life predictions of the hot end components subjected to TMF, was done. The models are usually calibrated and validated on the basis of uniaxial data in correlation plots [17, 21, 27, 29, 33, 45, 49, 65, 67]. The correlation plots can be seen later in Section 4.3. The most challenging part of the component analysis is to create a multiaxial criteria based on uniaxial experimental data and to perform mean stress corrections (as mentioned before, mean stress influences fatigue life – see Figure 3.10). There are several approaches and models for the multiaxial fatigue life predictions, that have been used:

Energy-Based Approaches

The energy-based approaches use a quantity called dissipated energy per cycle w . The criterion was proposed by Charkaluk and Constantinescu in [16]. Since this approach has been used in the practical part of the thesis, it is not explained extensively in this subsection, but in Subsection 4.3.1. The same approach was used in several references with various modifications. For example, two energy-based criteria were used in [40]. The first criterion was temperature-independent and used the so-called normalized plastic energy. The second criterion used constants calibrated only for the highest temperature present in the cycle. Note that the difference on the component's life prediction was of factor of 3 in the most critical area between these two fatigue life models. Another energy-based criterion was used in [38]. The very same model is used in this thesis. Additionally, a temperature-independent energy-based criterion was used in [17].

Strain-Based Approaches

The strain-based approaches use a well-known Basquin and Manson–Coffin curve, or some modification of it. The quantities which are used in the model are elastic and plastic strain ranges per cycle. Since this approach has been used in the practical part of the thesis, it is not explained extensively in this subsection, but in Subsection 4.3.1. The same approach was done in a few references. For example, the original strain-based criterion was used in [63]. The strain-based criterion with the mean stress correction by Morrow was used in [55]. Finally, a temperature-dependent variant, which interpolates between the temperature levels at which the model was calibrated, is mentioned in the commercial post-processor [28]. The same approach was used in this thesis, as shown later.

Neu–Sehitoglu Damage Model

The damage-based models are an extension of the strain-based approaches. The damage model developed by Neu–Sehitoglu is a frequently used damage-based model in TMF [10]. The damage per cycle is the sum of three damage mechanisms [10]. The damage term is the inverse value of numbers of cycles to failure:

$$\frac{1}{N_f} = \frac{1}{N_{fat}} + \frac{1}{N_{ox}} + \frac{1}{N_{creep}} \quad (3.13)$$

Each damage part expresses the damage mechanism present in TMF, as described in Section 2.1. The individual subscripts for the number of cycles to failure N means: fat

the damage caused by fatigue, $_{ox}$ the damage caused by oxidation and $_{creep}$ the damage caused by the creep. Each damage part is calculated separately, based on the mechanical data (e.g. FEM simulation). A good explanation of how to calibrate this model is in [67], where the model was used also on the component prediction. This model was also used in [45], as a part of the commercial post-processing software FEMFAT² which implemented this model. The calibration of the fatigue life model is described in great detail in the mentioned paper.

Taira Damage Model

Another damage-based model used in TMF component life prediction was proposed by Taira [7]. It is one of the first damage-based models in this field. The fatigue damage per cycle is assumed to be proportional to the temperature-dependent damage factor and plastic strain range powered, and multiplied by two temperature-independent material parameters. The Taira fatigue life model has been used in [23].

Seifert-Riedel Mechanism-Based Model

Seifert and Riedel developed a mechanism-based fatigue life model, which is based on the crack tip opening displacement [27, 71]. „*The hypothesis of the mechanism-based model for TMF life prediction is that the life of a component under TMF loading conditions is dominated by the number of cycles for a small crack to grow from an initial length a_0 to a technical length a_f . Hence, a crack growth law is used to describe the evolution of damage.*” [71]. The fatigue life model contains the properties from the Ramberg–Osgood relationship (Equation 3.6), Norton’s creep law (Equation 2.8) and accounts for environmental effects by using a diffusion-based model [71]. This model is implemented in the commercial fatigue post-processing software T-fat³.

Strain Range Partitioning

Strain Range Partitioning (SRP) is another approach for the TMF life prediction. It was developed by Manson et al. in 1971 [11]. Instead of working with the total inelastic strain range separately, the SRP fatigue life model partitions the inelastic strain range into time-independent plasticity and time-dependent creep. Assuming a fully reversed cycle, four combination cycles of inelastic strain are considered in the SRP model [11]:

PP – plasticity in tension and plasticity in compression

CC – creep in tension and creep in compression

PC – plasticity in tension and creep in compression

CP – creep in tension and plasticity in compression

The most simple form of SRP model uses the linear damage rule (Manson, Halford and Hirschberg 1971) [11]:

$$\frac{1}{N_f} = \frac{1}{N_{pp}} + \frac{1}{N_{cc}} + \frac{1}{N_{pc}} + \frac{1}{N_{cp}} \quad (3.14)$$

²www.enginsoft.com/bootstrap3/images/products/femfat/femfat_max_LR.pdf

³www.adacs-eng.com/t-fat-thermo-mechanical-fatigue-analysis-tool.html

where N is number of cycles to failure and subscripts are corresponding with the list of the damage cycles above. The theoretical background of this model can be found, for example, in [11]. The SRP of Manson–Halford model was used by Hazime et al. in [18] on the hot end component analysis. The SRP fatigue life model is implemented in the commercial post-processing software fe-safe/TURBOLife™⁴.

Critical Plane Approach

The Critical Plane Approach (CPA) is rather a multiaxial criterion than a fatigue life model. Experiments show that the cracks nucleate (and grow) on specific planes, the so-called critical planes. These planes are usually maximum shear or maximum tensile stress planes, depending on the material and loading conditions. CPAs are attempting to describe the physical nature of the fatigue damage. The critical plane models are multiaxial fatigue models, which are calculating damage (usually strain quantities) on these planes [79]. Hence, it is an approach used for gaining an equivalent quantity from a multiaxial load state. Part of the post-processing is to iteratively identify the critical plane, which can lead to extensive computational times [70].

This approach has been used on the hot end component TMF life prediction in [57, 70] with a damage-based fatigue life model (Nagode) and Swift–Watson–Topper parameter. The CPA was used for mode I – maximum normal stress, integrated as a C++ post-processor. The stress tensor was calculated for every time step, and fatigue damage was calculated for every plane (meaning the plane is rotated in space by two rotation angles). The plane with the maximum calculated fatigue damage is the critical one [57].

Commercial fatigue life post-processors have also implemented this state-of-the-art approach, e.g. FEMFAT or nCode⁵. The implementation of CPA is one of the possibilities of further research.

Similar to Subsection 3.3.1, there are a lot of phenomenological TMF life models that have been proposed and developed for only uniaxial test data. Each criterion is suitable for different material and loading. However, the author was searching for fatigue life models that have been used for the TMF life predictions of the components. There is a great space in further research and development in this area.

⁴www.3ds.com/fileadmin/PRODUCTS/SIMULIA/PDF/brochures/fe-safe-turbolife-brochure.pdf

⁵www.ncode.com/images/Resources/Proceedings/2016/2016nCodeUGM_NewCapabilitiesforFatigueLifewithnCode.pdf

4. Thermo–Mechanical Fatigue of the Exhaust Manifold – Case Study

4.1. Material Model

4.1.1. Considered Material

A SiMo cast iron was considered for this particular case study. As mentioned in Section 3.1, this cast iron is commonly used in automotive diesel applications (turbocharger turbine housings, exhaust manifolds, exhaust gas recirculation system housings, etc.) due to its good castability (suitable for such complex shapes), low cost and appropriate mechanical properties up to 750°C [42, 43, 65]. The material SiMo 4.06 was considered, for which most of the necessary material testing was published in [53, 65, 70]. Bartošák et al. designed an in-house testing stand with resistance heating for material tests at high temperatures, the results of which have been discussed extensively in a number of papers. The chemical composition of the tested material is shown Table 4.1 and the spherical graphite microstructure is depicted in Figure 4.1. The available material tests are in Figures 4.2–4.5.

Table 4.1: Chemical composition of considered SiMo 4.06 cast iron [65]

Si [%]	C [%]	Mo [%]	Mn [%]	Cr [%]	Cu [%]	Mg [%]	P [%]	Ni [%]	Al [%]
4.10	3.21	0.555	0.394	0.085	0.066	0.048	0.038	0.024	0.018

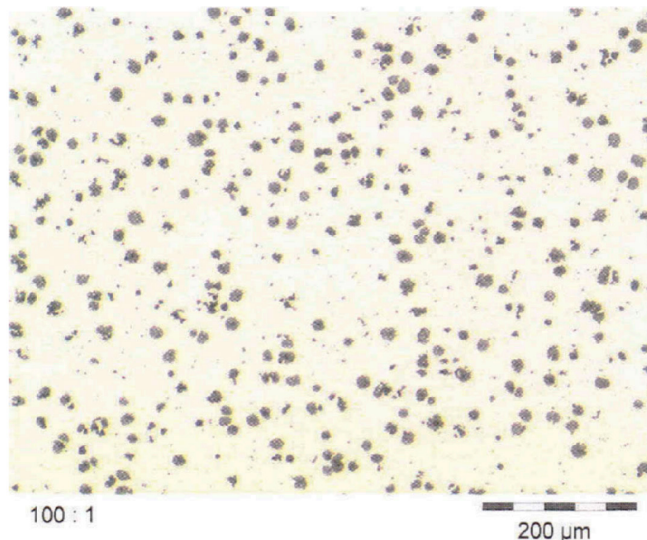


Figure 4.1: Spherical microstructure of considered SiMo 4.06 cast iron at room temperature [65]

Additionally, temperature-dependent physical properties (i.e. coefficient of thermal expansion, thermal conductivity, specific heat and density) depicted in Figure 4.6, necessary for intended transient thermal simulation, were obtained from the report [30]; in which a very similar cast iron SiMo 4.05 was extensively investigated.

4.1.2. Available Experiments

- Temperature-dependent Young's modulus (left) and initial yield stress (right) – Figure 4.2

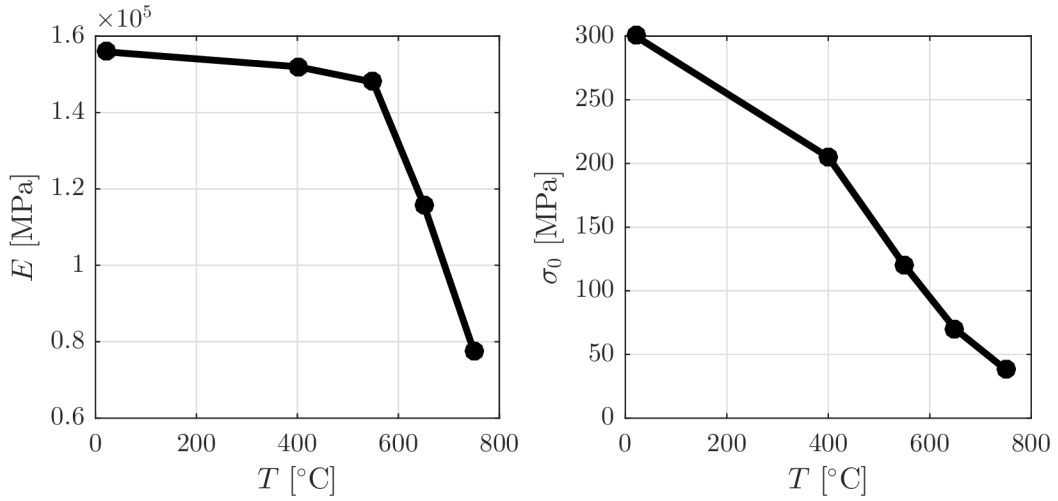


Figure 4.2: Young's modulus E (left) and initial yield stress σ_0 (right) [53, 65]

- The LCF saturated hysteresis loops at half life ($N_f/2$) at a strain amplitude of $\varepsilon_a = 0.006$ for 4 different isothermal levels (400°C, 550°C, 650°C and 750°C) with recorded maximum stresses as a function of the number of the cycles – Figure 4.3

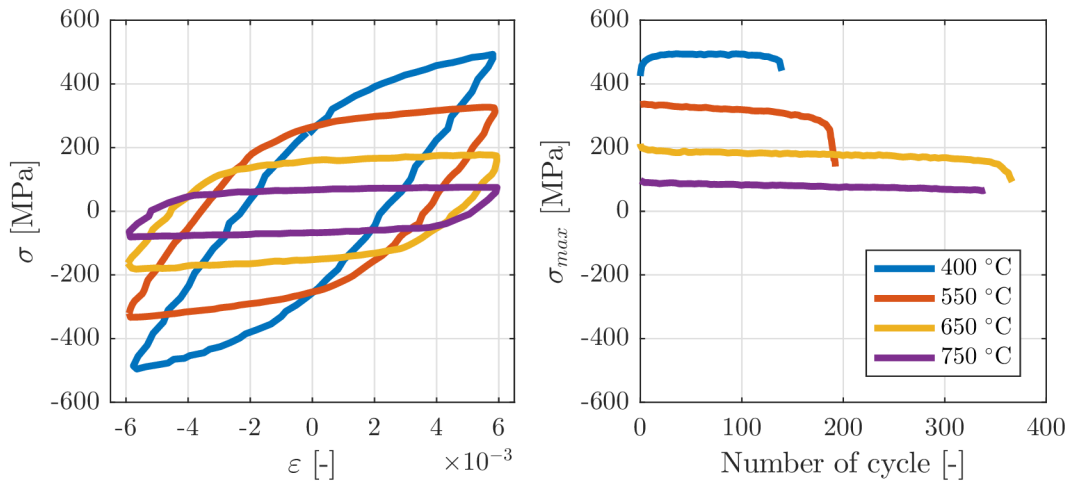


Figure 4.3: Saturated LCF hysteresis loops (left) and maximum stress as a function of the number of the cycles (right) [65]

- The cyclic stress–strain curves for 20°C, 400°C, 550°C, 650°C, 750°C – Figure 4.4

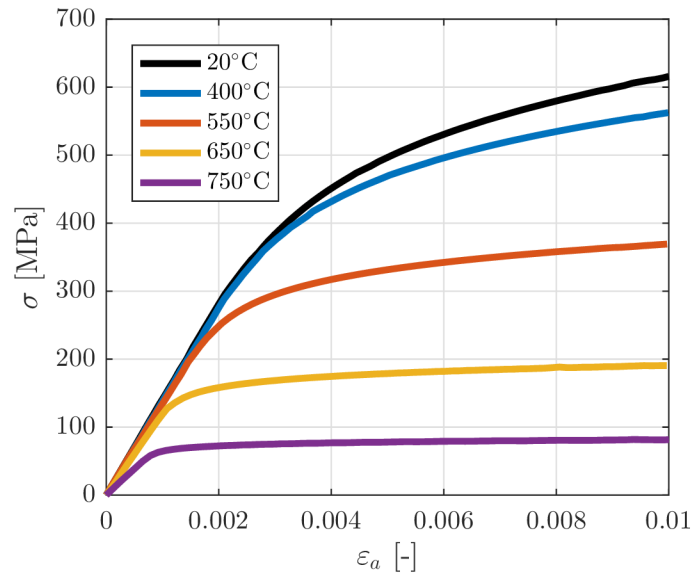


Figure 4.4: Cyclic stress–strain curves [70]

- The OPTMF test with variation of temperature from 100°C–650°C, including the test profile ($R_{\epsilon^m} = -\infty$) – Figure 4.5

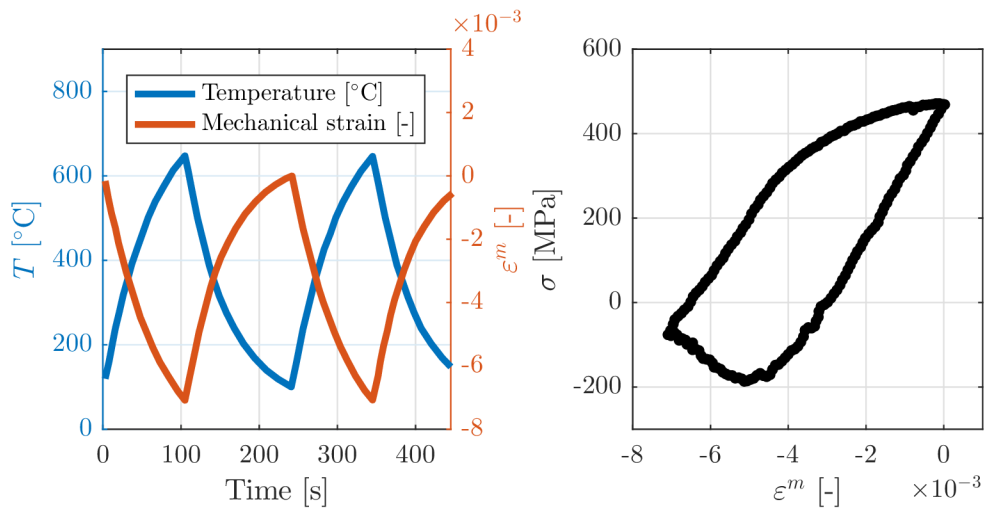


Figure 4.5: OPTMF test profile (left) and saturated stress response in a hysteresis stress–mechanical strain loop (right) [65]

- The temperature-dependent physical properties – Figure 4.5

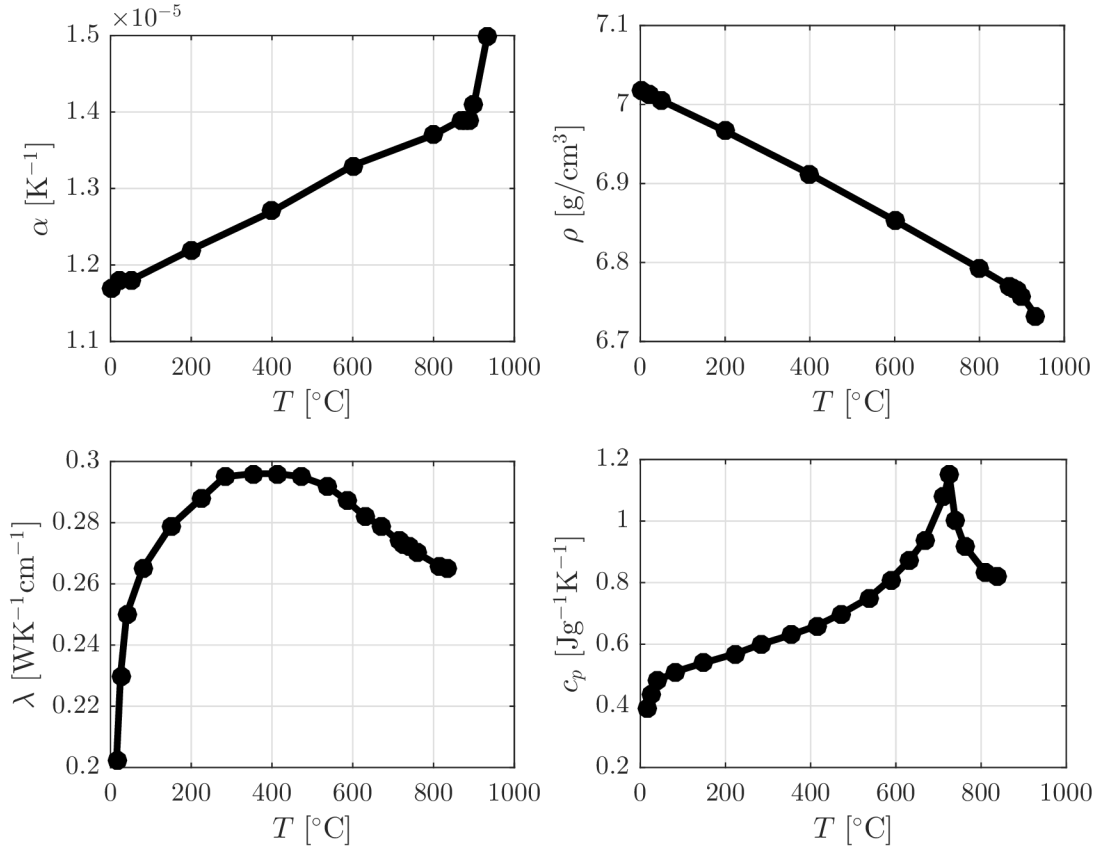


Figure 4.6: Coefficient of thermal expansion α (top left), thermal conductivity λ (bottom left), specific heat c_p (bottom right) and density ρ (top right) [30]

4.1.3. Calibraton and Validation of Material Models

Bilinear Kinematic Hardening

The Bilinear Kinematic Hardening (BKIN) material model expands the linear elastic model with two additional constants – the tangent modulus E_T and yield stress σ_0 . Essentially it is a temperature-dependent Prager’s model from Equation 3.11 (the E_T is in total strain coordinates whereas the C from this equation is in plastic strain coordinates) with a rheological schema from Figure 2.9 a). The model is implemented in the commercial software ANSYS. The σ_0 is a property of material, but when fixing the σ_0 at a known value from the tensile test, the identified value of E_T is large; making the stress–strain curve very steep and over-predicts stresses for larger strains. On the other hand, when both σ_0 and E_T are calibrated as variables, the hysteresis loop is described more accurately, but plasticity occurs later than in reality. This phenomenon is depicted in Figure 4.7.

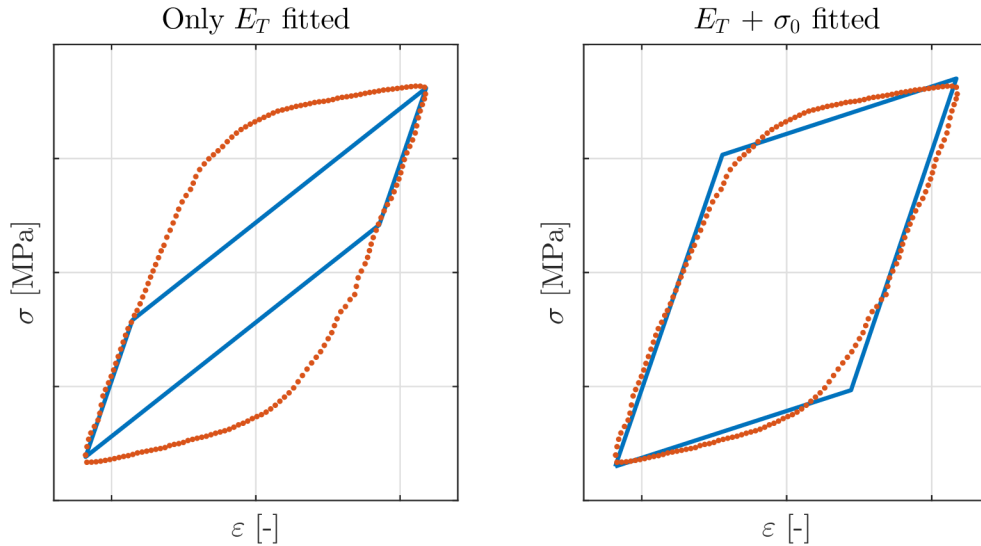


Figure 4.7: BKIN calibrated with E_T as an only variable (left) and with both σ_0 and E_T as variables (right)

The latter approach was chosen – hence σ_0 and E_T are considered as unknowns. Initially, a calibrating script was created in MATLAB R2016a, where only the tensile branch of the isothermal hysteresis loop is used for calibration, since BKIN behaves the same in tension and compression. The *fmincon* function from the Optimization Toolbox™ was suitable for such least-squares identification. The calibration itself is simple, since BKIN is a bi-linear function.

The validation of calibration is performed on two levels in ANSYS. A set of ANSYS Parametric Design Language (APDL) macros was developed for validations. At first, the isothermal validation is performed. Only one PLANE182 element was used in the FE model. Setting the element length to 1 mm enables to directly take displacements as strains. The numerical model of the isothermal LCF test is shown in Figure 4.8, where UY stands for displacement in y axis direction. The stress response from this analysis is then plotted against the experiment, and one needs to verify the fit. This is done for each temperature separately. The validation with constants obtained by least-squares fitting is depicted in Figure 4.9.

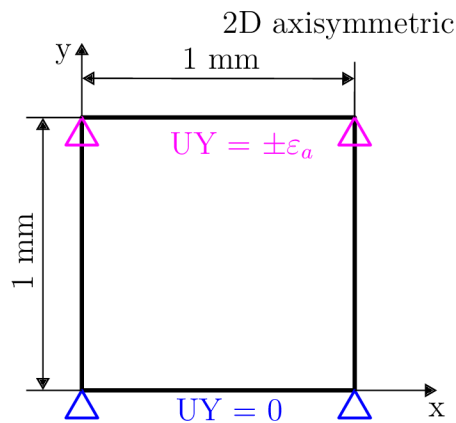


Figure 4.8: FEM model of LCF isothermal test

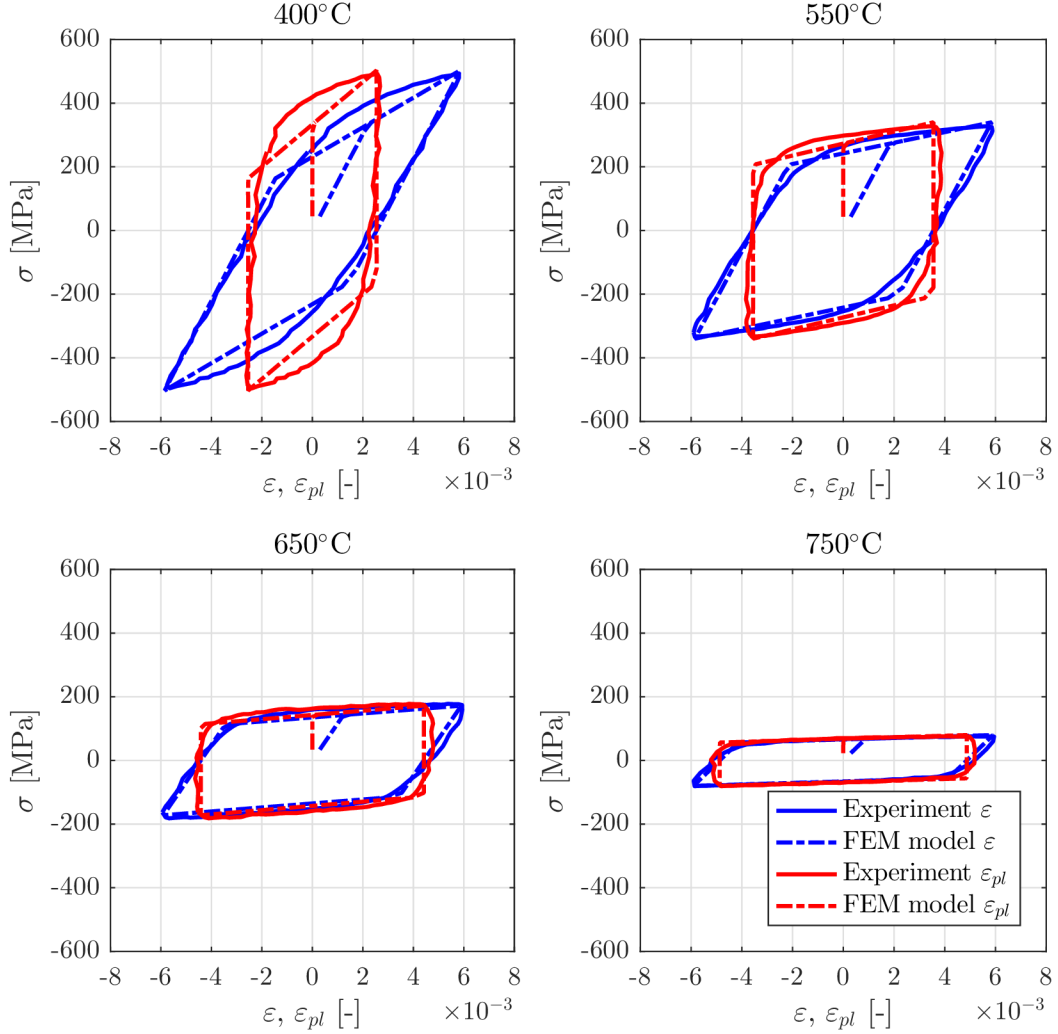


Figure 4.9: Validation of the calibrated BKIN model on the isothermal level, initial calibration by means of least-squares

Secondly, a non-isothermal validation is done on the basis of an OPTMF test. The identified set of constants is submitted to the APDL macro, this time for all n number of temperature levels at which the IF tests were conducted and the model was calibrated. Then the FEM simulation solves a model of the OPTMF test. Similarly, one PLANE182 element 2D axisymmetric model is used in developed APDL code. This leads to a one-way coupled steady state thermal – static structural analysis. Since the PLANE182 element enables thermal strains, the author chose to perform this analysis only in the static structural ANSYS analysis type, and not the classical steady state thermal – static structural approach with change of the element type. At first, a simulation is performed with only temperature effects from Figure 4.5 (left) in order to obtain the thermal strains ε^{th} , then the total strain ε is computed from the Equation 4.1 [70].

$$\varepsilon = \varepsilon^m + \varepsilon^{th} \quad (4.1)$$

The mechanical strain ε^m is discretized from the test profile from Figure 4.5 (left). Lastly, a simulation with both temperature and structural effects is computed. Figure 4.10 shows

the workflow. This approach ensures to obtain stress response with the same mechanical strain profile as in the real test seen in Figure 4.11. Note that *time* is represented by *loadstep* number in the static simulation.

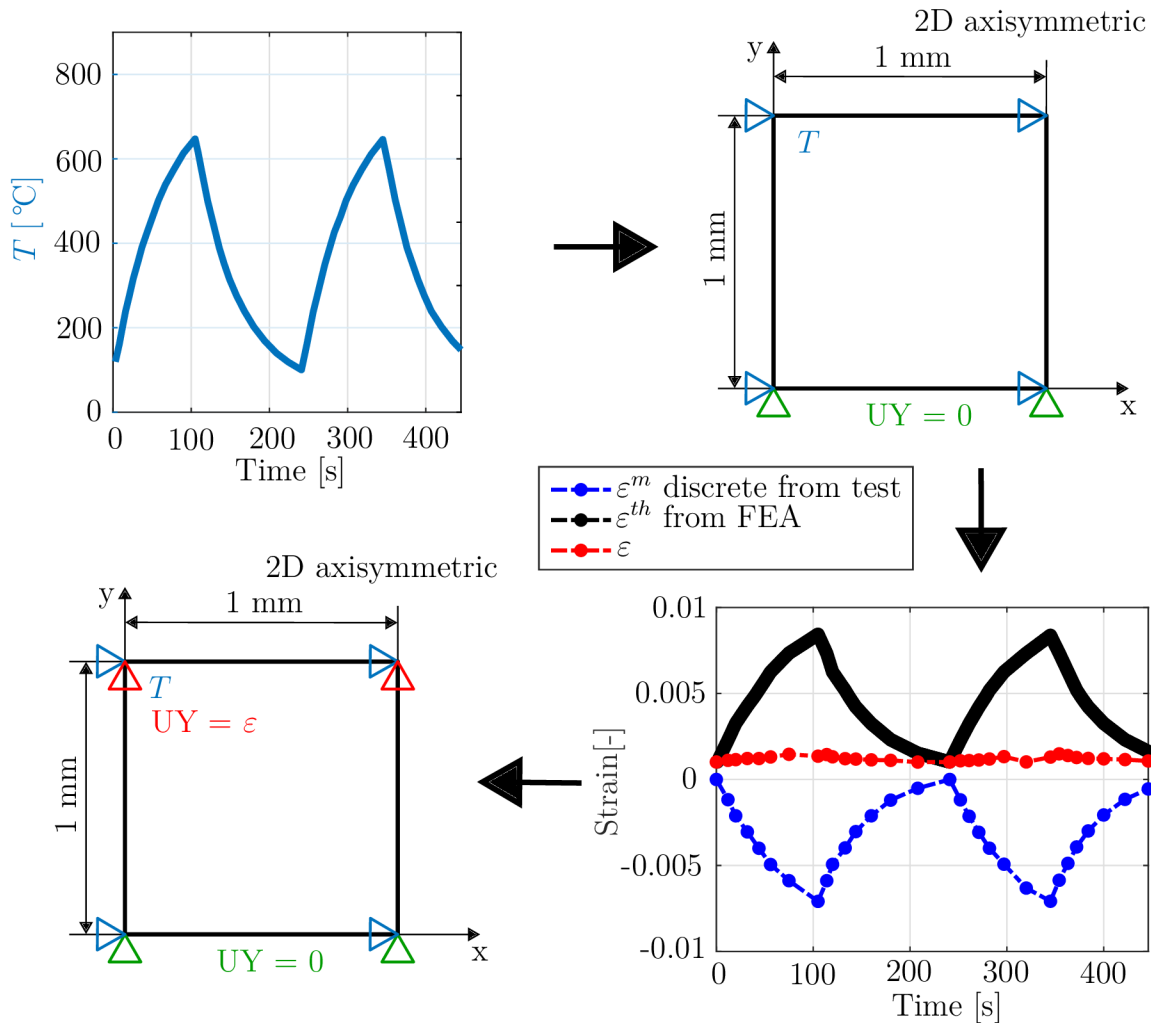


Figure 4.10: FEM model of OPTMF non-isothermal test and the simplified workflow

When the BKIN model with initially identified constants by least-squares fitting is validated on a non-isothermal level, a non-satisfactory stress response in comparison with the experiment is obtained. This is likely caused by still having relatively high values of E_T , which tends to over-predict stresses for higher strains. The non-isothermal validation with bad stress response, using the initially-calibrated BKIN model compared to the experiment, is in Figure 4.12.

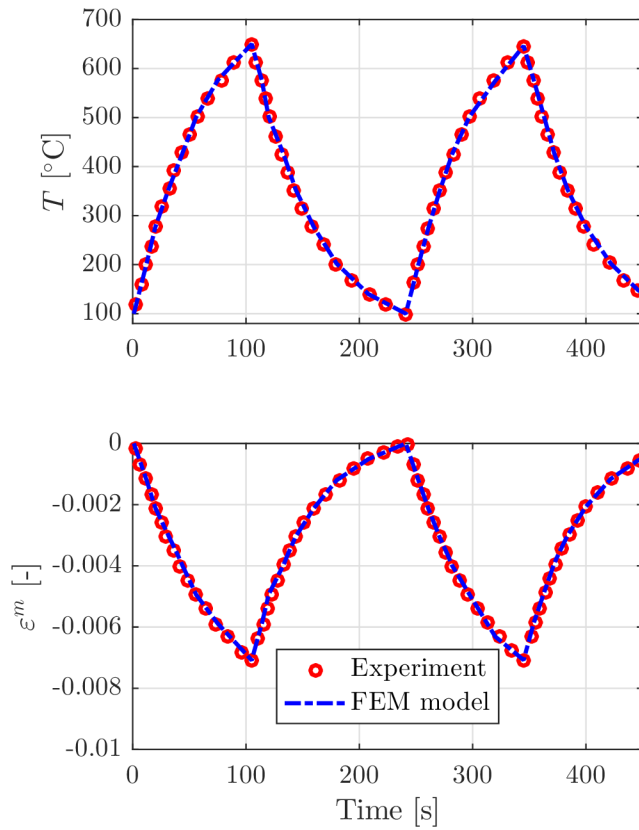


Figure 4.11: Validation of calibrated BKIN model on non-isothermal level – control quantities

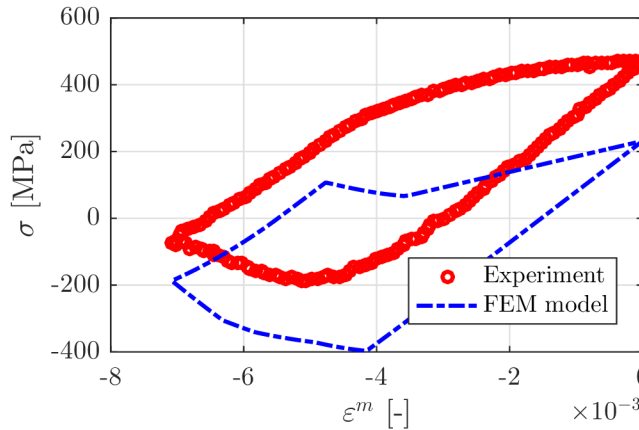


Figure 4.12: Validation of the calibrated BKIN model on a non-isothermal level, initial calibration by least-squares fit – bad stress response compared to the experiment

Hence, the constants E_T and σ_0 were modified for temperatures 400°C, 550°C and 650°C manually, in order to obtain a better description of the OPTMF test. That means decreasing the value of E_T and increasing the value of σ_0 . The flowchart of calibration is depicted in Figure 4.13. The isothermal validation with manually modified BKIN constants is in Figure 4.14. The isothermal fit is worse compared to the initial model, with constants obtained by least-squares fitting (Figure 4.9). However, the non-isothermal

behavior is better and it is plotted in Figure 4.15. Therefore, it is a trade-off between the isothermal and non-isothermal behavior. Subsequent analyses will be conducted with manually-adjusted BKIN constants, since the non-isothermal behavior is more important for TMF. It is evident that the non-isothermal hysteresis loop from the OPTMF test gained with the BKIN material model is not smooth and has some sharp peaks. This is a product of approximation of the non-linear curve by a bi-linear one.

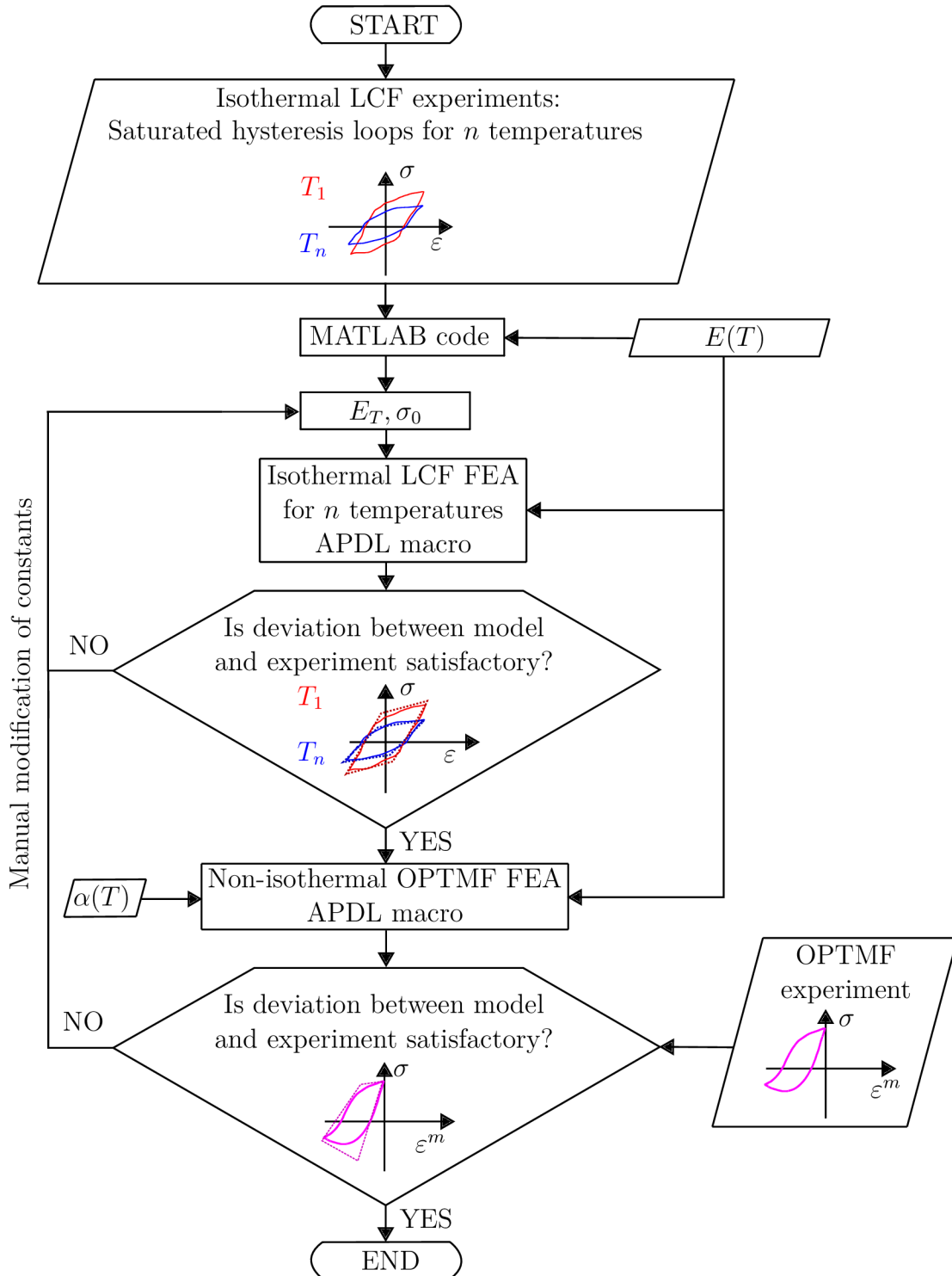


Figure 4.13: Flowchart of a temperature-dependent BKIN model calibration

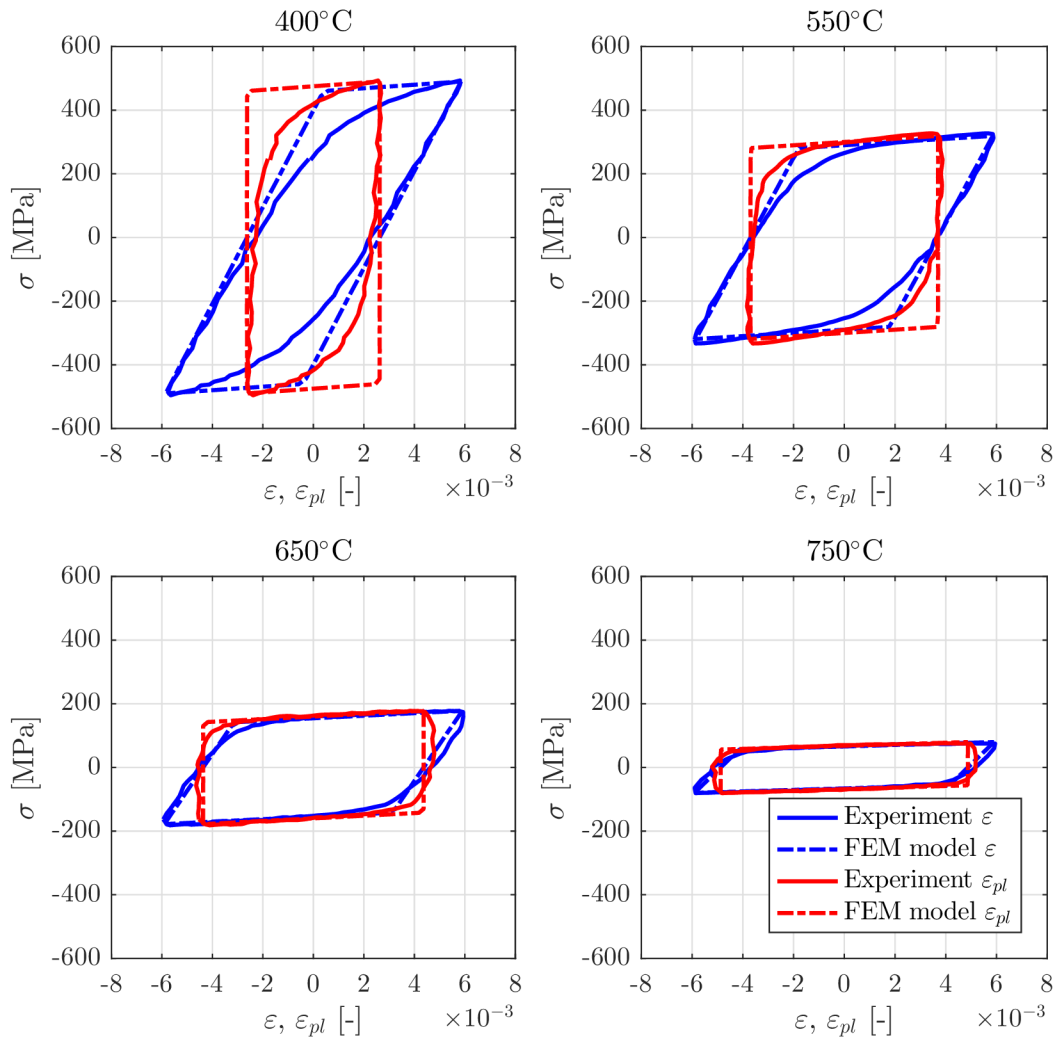


Figure 4.14: Validation of the calibrated BKIN model on the isothermal level, manual adjustment of constants

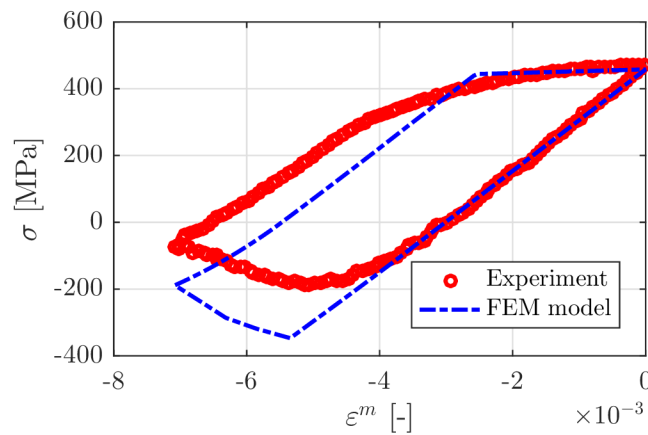


Figure 4.15: Validation of the calibrated BKIN model on the non-isothermal level, manual adjustment of constants – better stress response compared to Figure 4.12

The identified constants were also plotted against the temperature in Figure 4.16. It can be seen that with the increasing temperature, the magnitudes of the constants are decreasing. The importance of the trend of constants plotted against temperature is addressed in the following subsection on the Chaboche model, since it is a more complex model and the number of identified constants is larger. However, it is an important property of the solution and it applies to the BKIN model in the same manner.

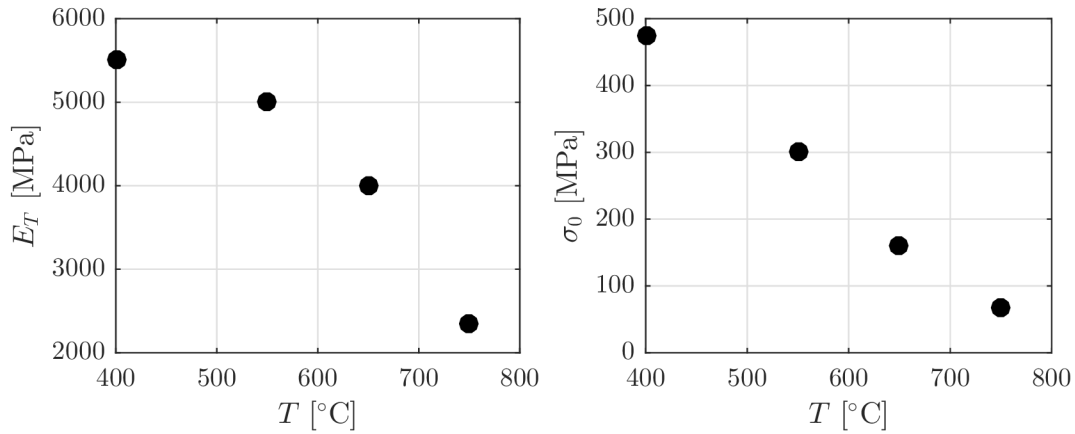


Figure 4.16: Identified BKIN constants plotted against the temperature

Chaboche

In order to obtain a more accurate description of material behavior in comparison to the BKIN model, a Chaboche model was calibrated. The model is also implemented in ANSYS.

The relationship used for the determination of constants present in Chaboche's non-linear kinematic hardening model without ratcheting for uniaxial tension is defined by Equation 4.2 [8]. Note that in Subsection 2.1.1, C and γ were referenced as generic material properties. From now on, C and γ are related only to Chaboche's kinematic hardening model. Hence:

$$\sigma = \sigma_0 + \sum_{i=1}^{k-1} \frac{C_i}{\gamma_i} (1 - 2e^{-\gamma_i[\varepsilon_{pl} - (-\varepsilon_{pl,a})]}) + C_k \varepsilon_{pl} \quad (4.2)$$

where C_i is a constant that is proportional to the hardening modulus [35], γ_i is the rate of decrease of the hardening modulus [35], ε_{pl} is plastic strain and $\varepsilon_{pl,a}$ is plastic strain amplitude.

It needs to be stressed that the unknown constants are temperature-dependent, hence $C_i(T_j)$ and $\gamma_i(T_j)$. The values of these constants are not randomly determined, but they have a physical meaning and follow requirements, which create a set of linear constraints. On the isothermal level T_j , where $j = 1, 2, \dots, n$ and $i = 2, 3, \dots, k - 1$:

$$C_i(T_j) \geq C_{i+1}(T_j) \quad (4.3)$$

$$\gamma_i(T_j) \geq \gamma_{i+1}(T_j) \quad (4.4)$$

Also, the magnitude of constants C_i and γ_i should not have a random trend when plotted against temperature, but rather a decreasing trend; otherwise one might end up with convergence issues [70] or calibrate a material that gives unreasonable stress-strain responses [50]. This statement can be interpreted on a non-isothermal level, where $j = 1, 2, \dots, n - 1$ and $i = 2, 3, \dots, k$:

$$C_i(T_j) \geq C_i(T_{j+1}) \quad (4.5)$$

$$\gamma_i(T_j) \geq \gamma_i(T_{j+1}) \quad (4.6)$$

where $T_j < T_{j+1}$.

Therefore, the unknown set of constants for the desired number of backstresses k , and the levels of temperatures n , is determined on the basis of the non-isothermal approach (the constants are determined together with respect to temperature and not separately for each temperature). A script was developed in MATLAB, version R2016a, using Optimization Toolbox™. The mentioned set of linear constraints can be effectively implemented using the *fmincon* function used for finding a minimum of constrained nonlinear multi-variable function. The problem solved by *fmincon* is specified as [80]:

$$\min \tilde{x} \text{ for } f(\tilde{x}) = \begin{cases} ceq(\tilde{x}) = 0 \\ \mathbf{A} \cdot \tilde{x} \leq \vec{b} \\ lb \leq \tilde{x} \leq ub \\ x_0 \end{cases} \quad (4.7)$$

where \tilde{x} is an unknown set of constants for all temperature levels $C_i(T_j)$ and $\gamma_i(T_j)$, $f(\tilde{x})$ is the objective function to minimize (i.e. deviation between the experiment and the material model), \mathbf{A} is a linear inequality constrain matrix (defines inequality between constants according to 4.3, 4.4, 4.5 and 4.6), \mathbf{b} is a linear inequality constraints vector (in this case $\mathbf{b} = \mathbf{0}$), $ceq(\tilde{x})$ is equality constraint (constraint which forces the initial and last point of the curve to be equal with experiment), lb and ub are lower and upper bounds of \tilde{x} and x_0 is an initial guess of \tilde{x} from which the solver starts the optimization.

The calibration flowchart is depicted in Figure 4.17. A number of macros were developed for the task.

A set of n saturated isothermal LCF loops is submitted to the created MATLAB code. Only a tensile branch of the hysteresis loop is supposed for the Chaboche model (the model is symmetrical in tension and compression). Additional inputs, as E and σ_0 for n temperatures are also needed, and then the number of backstresses k is specified, for which the set of unknown constants is found. The code works with the general number of $k = 2 \div \infty$ backstresses (note that ANSYS supports up to $k = 5$ [35]). The model was calibrated for $k = 3$ backstresses, which adequately represents the stabilized stress–strain hysteresis loop [70].

The developed code then fits the Equation 4.2 to the saturated hysteresis loop for each temperature, with constraints 4.3–4.6, and returns the constants using a gradient-based optimization solver [80].

Validation of the obtained constants is again on two levels. At first, the isothermal level is validated. A set of constants C_i , γ_i is imported into the ANSYS APDL macro, and a model of the LCF test at constant temperature is solved. This is done in the same manner as in the BKIN calibration. The one-element model is the same as in Figure 4.8. Again, the stress response from this analysis is plotted against the experiment. If the material model does not fit the experiment well, it is possible to change x_0 , lb and ub . The x_0 is a very sensitive input, since the problem submitted to optimization is solved by means of a non-linear least squares fit. An educated guess of x_0 decides whether this technique works or not [19]. Also, the large amount of parameters that are identified might end up as non-objective identification [56]. The stability of identified parameters is discussed at the end of this subsection.

When the fit is good enough for the engineering resolution, the second level validation then succeeds. That is a non-isothermal OPTMF test. This is done in the same manner as BKIN calibration – see Figure 4.10. Again, the stress response from this simulation is plotted against the experiment, to see the non-isothermal behavior of the model. ANSYS interpolates Chaboche’s constants linearly in-between the discrete temperature levels at which the material model was calibrated [27, 56, 70].

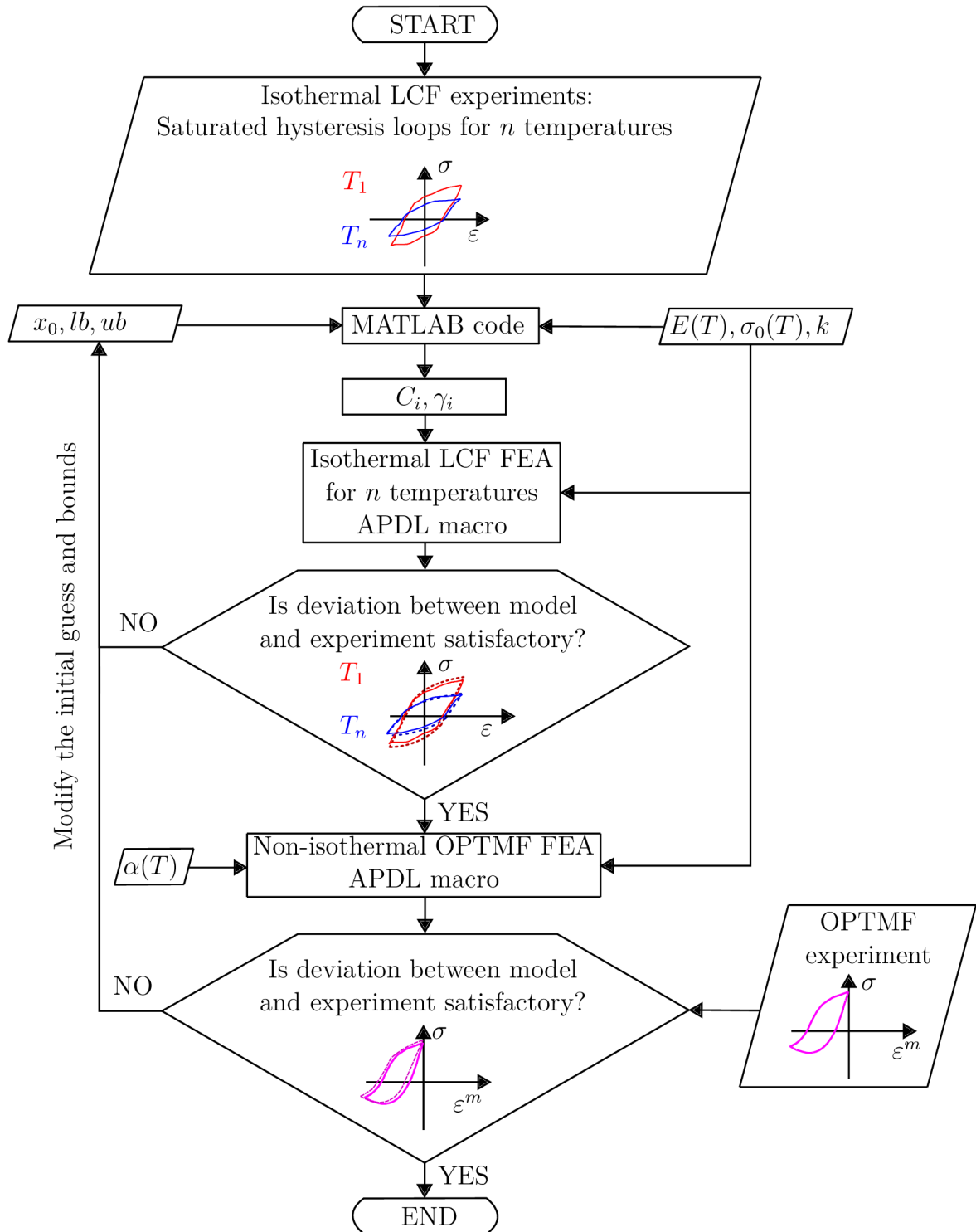


Figure 4.17: Flowchart of the temperature-dependent Chaboche model calibration

The isothermal validation is depicted in Figure 4.18. The model was additionally validated with recently published experiments from [74] in the Appendix A of the thesis, however these experiments were not used for the calibration.

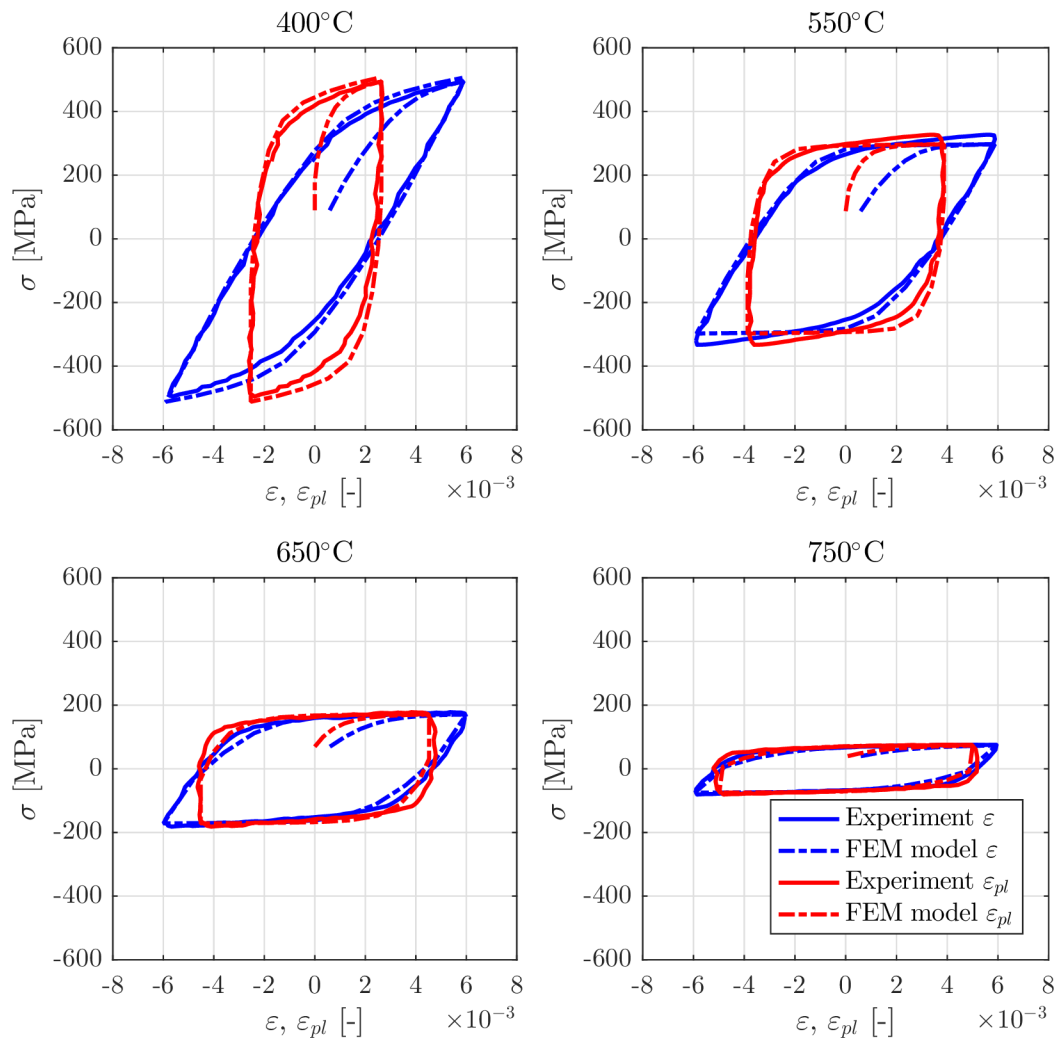


Figure 4.18: Validation of the calibrated Chaboche model on the isothermal level

The non-isothermal validation of control quantities is the same as in the BKIN. It is depicted in Figure 4.11, and the stress response in Figure 4.19:

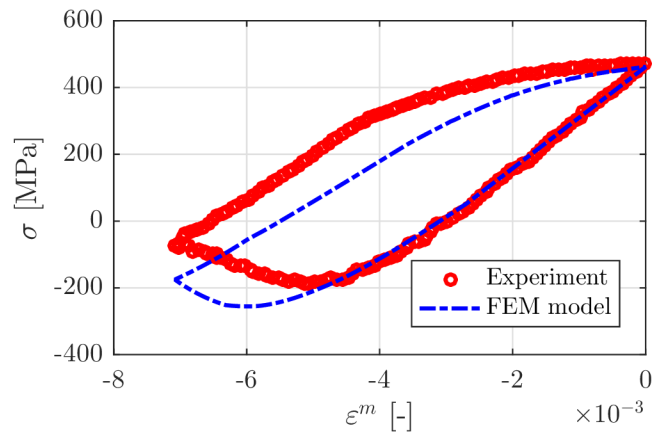


Figure 4.19: Validation of the calibrated Chaboche model on the non-isothermal level – stress response

For a better understanding of the OPTMF test stress response, a color-mapped chart was plotted in Figure 4.20:

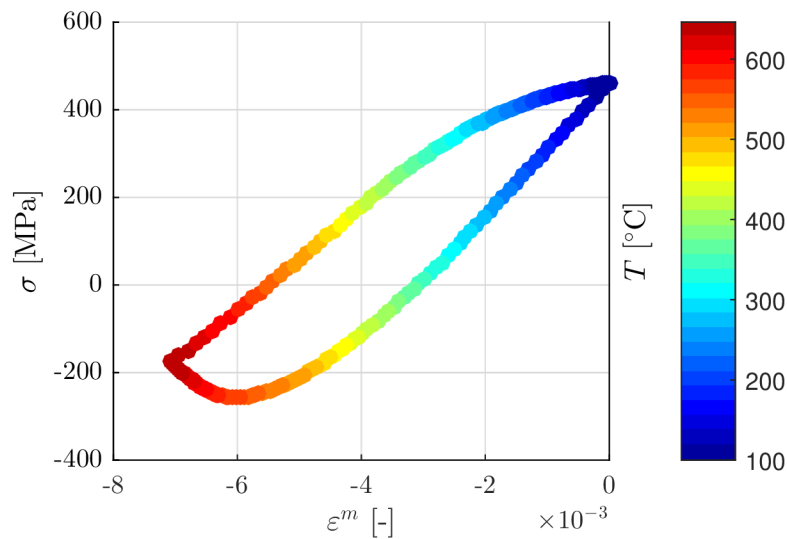


Figure 4.20: FEM model stress response for the OPTMF test model with the temperature magnitude depicted using a colormap

The Chaboche model gives significantly better agreement with the experiment on both isothermal and non-isothermal levels in comparison to the BKIN model. However, it can be concluded from Figures 4.19 and 4.20, that the stresses are over-predicted at high temperatures on the non-isothermal level. This is due to the fact that there is significant application of stress relaxation and viscous behavior at high temperatures¹ (significant time-dependent plasticity for temperatures over 450°C [70]).

The IF tests are typically done at a significantly higher strain rate in comparison to OPTMF tests. This model is not rate-dependent, hence these effects are omitted. To be able to describe the high temperature region more accurately, a higher-level material model needs to be calibrated (e.g. rate-dependent models like EVH or 2LVP as described in Subsection 3.3.1). The author did not have access to such experimental data, which is required for the aforementioned material model calibration. This is a further possibility for future research, and it is described in Chapter 5.

In addition, the identified constants are plotted against the temperature in Figure 4.21. It can be seen that the constraints from Equations 4.3–4.6 representing isothermal and non-isothermal inequalities were fulfilled. The importance of decrease of the magnitude with respect to temperature is a substantial aspect of calibration. One might end up with convergence issues [70] or get unrealistic material responses, which was studied in [50].

This model could further be expanded to combined hardening (kinematic + isotropic), however from Figure 4.3 (right), it is evident that the isotropic (cyclic) hardening is only present at 400°C for a few initial cycles; and the rest of the temperature levels show no significant isotropic hardening/softening. The hysteresis loops are stabilized in a few cycles. Therefore, the combined hardening was disregarded and only kinematic hardening was taken into account (the same approach was chosen in [70]). Thus, the material parameters are obtained on the basis of cyclically stable hysteresis loops at half life.

¹This fact was discussed with prof. Dr.-Ing. Thomas Seifert of the Offenburg University of Applied Sciences (thomas.seifert@hs-offenburg.de) in a private email conversation. The over-prediction of stresses in the high temperature region is typical for this level of material model. *”...Typically the strain rate in the LCF tests is much higher than in the TMF tests. If you do not consider the time dependent material behavior (strain rate dependency, stress relaxation, ...), you most probably will overestimate the stresses at higher temperatures (as you do). Attached to this email you will find a figure of a TMF test done on a SiMo material with the corresponding models...”* The aforementioned figure is depicted in the Appendix B of this thesis with the permission of the professor. We can see that the behavior is similar to this case.

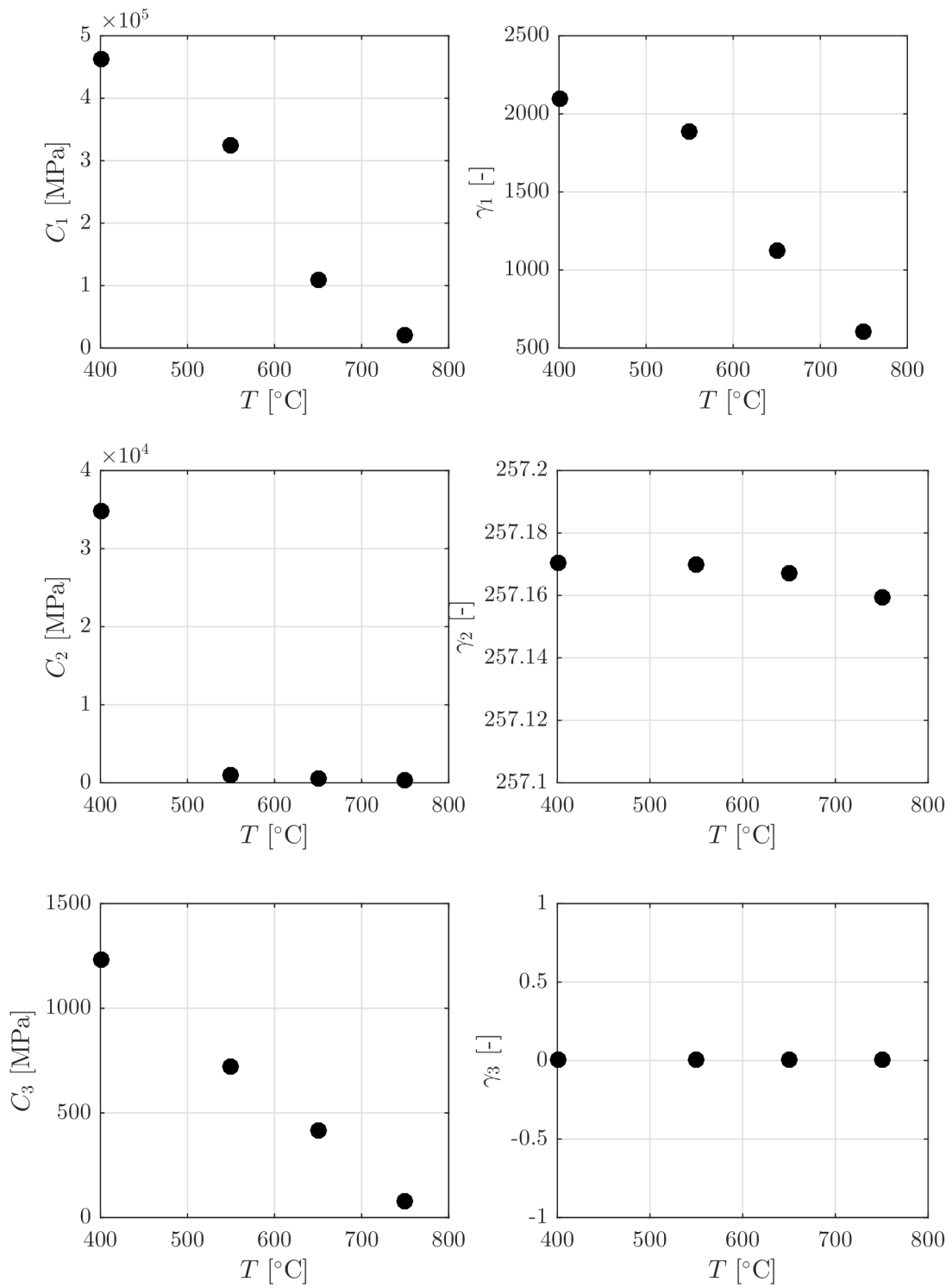


Figure 4.21: Identified Chaboche constants plotted against temperature

On the Stability of Material Parameters

Advanced temperature-dependent plasticity models (like Chaboche) contain a relatively large amount of parameters which are identified on the basis of material tests. This itself is a non-trivial task, because generally the material properties are non-objective – different persons might identify different material parameters which both give a good fit to the test data. Furthermore, „*small variations in the experimental data might result in large variations in material property values if they are determined with numerical optimization methods*” [56]. To be able to obtain a robust solution of material parameters, the loading history must be complex and activate all material phenomena (e.g. CLCF test in Subsection 3.2.4). This was studied at length in [56], where analytical and statistical approaches were used to examine the robustness of the solution on the basis of CLCF test. Since the author did not have these experimental data available, the obtained solution was considered as sufficient. Although this solution might not be the global minimum, it describes the experiments well. To be able to examine the robustness, at first a CLCF test which activates all material phenomena needs to be performed, and then a higher-level material model (with the Chaboche basis of non-linear kinematic hardening) could be calibrated. From this, the same approach as in [56] can be used (a calculation of covariance and eigenvalues of the Hessian matrix which informs about the curvature of the least-square function) and stable material properties are obtained. It was also noted in [56] that even by using the gradient-based optimization, sometimes manual modifications of constants are still needed, based on the experience of the engineer who identifies the constants.

4.1.4. Material Model for Additional Components

Since the component simulation considers the effects of bolt pre-tension and the water-cooled engine head, there are additional components present. It is common practice that the engine head is simplified into a rectangular block (called further on “engine head dummy”) as in [18, 27, 54]. The bolts are considered to be made out of AISI 304 stainless steel and the engine head dummy out of EN-GJL-250 cast iron, which is suitable for such application [47]. The physical and mechanical properties of AISI 304 steel are taken from [58]. The physical properties of EN-GJL-250 cast iron have been taken from [76] and the mechanical properties from [46]. Again, for the transient thermal simulation, λ , c_p and ρ are needed. For the subsequent structural analysis, a temperature-dependent α have been used and a temperature-dependent linear elastic model was considered for the additional components. The same approach was done in [55]. The properties for both AISI 304 steel and EN-GJL-250 cast iron are plotted in Figure 4.22 below. These values were input into the FEM simulations.

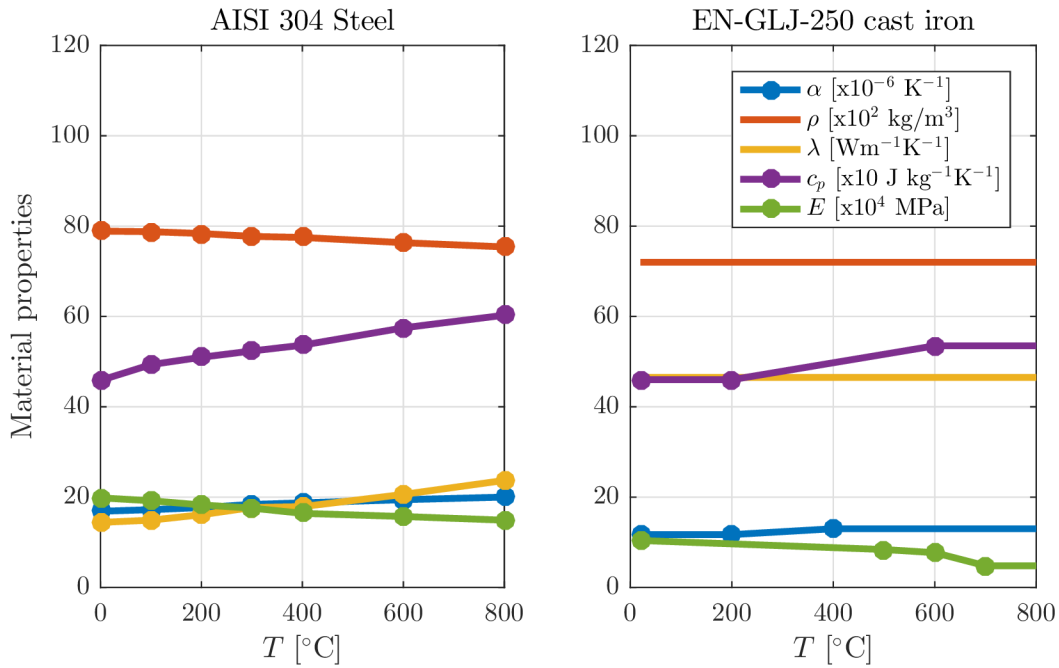


Figure 4.22: Physical and mechanical properties for bolts (AISI 304) [58] and engine head dummy (EN-GJL-250) [46, 76]

4.2. Finite Element Model

4.2.1. Model of Geometry

The model of geometry of a 4 cylinder exhaust manifold was created in Catia V5 R26 and can be seen in Figure 4.23. Since this thesis focuses on the workflow of these problematics, the model was done on purpose with planar symmetry. This is further beneficial with respect to number of elements for numerical modelling. Only half of the model is meshed, therefore the computational time is reduced.

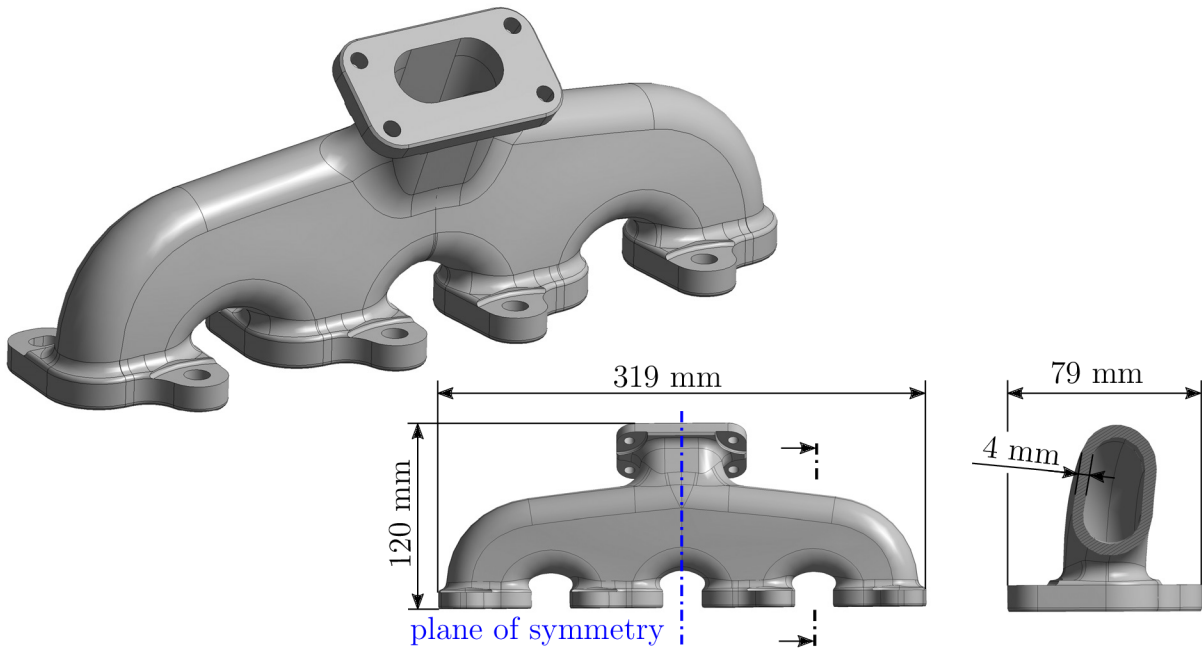


Figure 4.23: Model of geometry of the analyzed exhaust manifold with informative dimensions

4.2.2. Model of Thermal Boundary Conditions

The author would like to note that this subsection is not the goal of the thesis and is performed only in order to obtain thermal boundary conditions. Therefore, the topics regarding CFD and CHT are not described as extensively as the rest of the thesis, and the author leaves it up to the reader in case of interest for further research.

Thermal boundary conditions are usually estimated by in-house software with empirical approaches [18], one-dimensional modelling [63, 70] or on the basis of steady state CFD simulations [21, 27, 47, 61, 64]. All of these approaches should be calibrated and validated based on bench tests with the actual component prototype. The CFD simulation approach was chosen in this thesis. The CHT module is used for the forced convection between the fluid (exhaust gas) and solid (exhaust manifold).

For transient thermal FEM analysis, the bulk temperature T_{bulk} and heat transfer coefficient HTC are mapped onto the internal surfaces of manifold from the CFD simulation. This models the forced convection between exhaust gas and the exhaust manifold [18]. The problem is modelled as two steady state simulations of heat-up and cool-down conditions as in [61]. The exhaust manifold is loaded by the thermal shock. The thermal shock is a representation of in service loading, and it is used for validation of physical prototypes as well as for the model of the load in the virtual prototypes [16, 52]. The transformation of the in service temperature into the representative thermal shock can be done using Stress–Strength Interference Analysis, which has been proposed in [16]. The thermal shock profile used in this thesis is depicted in Figure 4.24. The two steady state conditions (heat-up and cool-down) calculated in CHT simulation are depicted by blue points. The exhaust gas temperature T_1 from thermal shock profile and the engine load ramps were created on the basis of [23, 37, 51, 52, 55] (heating for 300 s at 800°C, cooling for 400 s at 110°C, ramps for 10 s – total duration of 720 s). Then the T_{bulk} and

HTC from the two steady state moments are imposed to transient thermal analysis, and ramped based on the engine load line as described later.

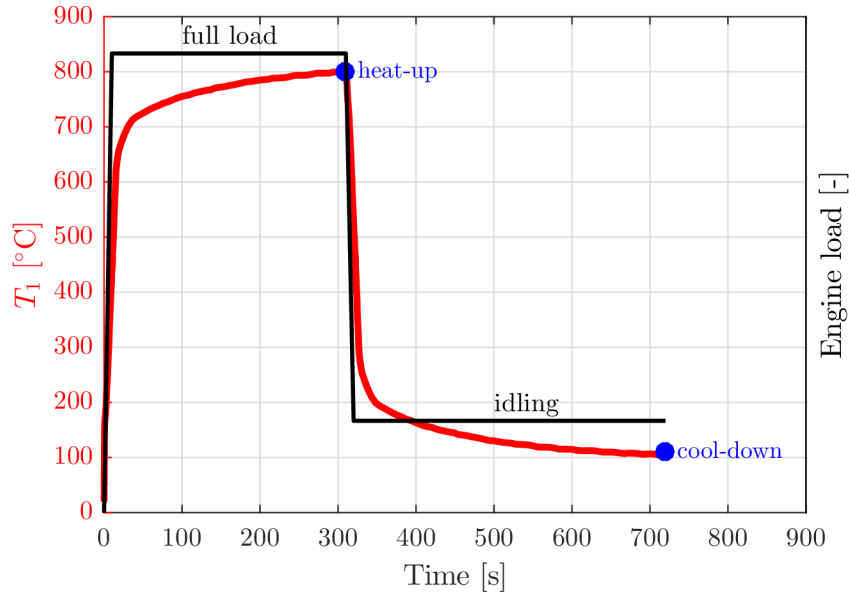


Figure 4.24: Considered thermal shock profile, created on the basis of [23, 37, 51, 52, 55]

The problem was modelled in ANSYS CFX 19.2. as two steady state CHT analyses. This approach averages the transient pulsations given by the pistons into a steady state calculation, as in [20]. The set of boundary conditions is prescribed on the basis of [20, 39]. This means an exhaust gas mass flow \dot{m} placed on the manifold's inlet 1 and 2, exhaust gas inlet temperature T_1 , exhaust gas static pressure at outlet P , ambient temperature T_{amb} , ambient heat transfer coefficient HTC_{amb} and the temperature on the inlet flange surface T_{cont} - as per Figure 4.25. The T_{cont} represents the temperature on the interface between the manifold and engine head, which is typically water-cooled [20]. The actual used magnitudes of \dot{m} , T_{cont} and P were consulted with an expert in this field². The walls are considered smooth. Additionally, a *symmetry* boundary condition was placed on the plane of the symmetry as in [59], and the inlet and outlet interfaces were extended with an adiabatic wall. The inlet was extended in order to evolve dynamic flow entering the exhaust manifold, and the outlet was extended to mitigate convergency issues when a backflow is present at the boundary condition interface. These are common adjustments to the fluid domain. A General Grid Interface with enabled heat transfer was placed between the fluid and solid domain.

²The magnitudes of \dot{m} , T_{cont} and P were consulted with Ing. Luděk Pohořelský, PhD., a Sr. Engineering Manager of the Power Train team in Garrett Advancing Motion.

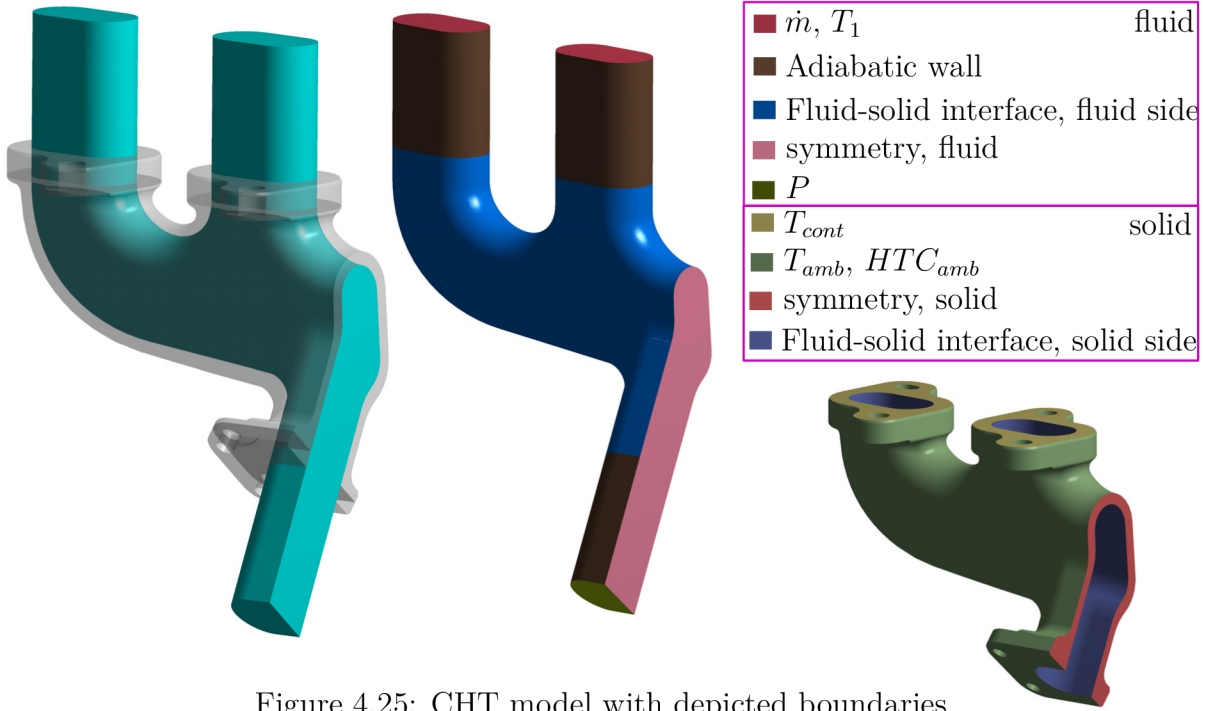


Figure 4.25: CHT model with depicted boundaries

The values of boundary conditions are in the Table 4.2.

Table 4.2: Values of boundary conditions for CHT analysis

	\dot{m} [g/s]	T_1 [°C]	P [bar]	T_{cont} [°C]	T_{amb} [°C]	HTC_{amb} [Wm ⁻² K ⁻¹]
heat-up	20	800	3	300	77	50
cool-down	6	110	1	100	77	50

The thermal conductivity and dynamic viscosity of the exhaust gas material model were set as temperature-dependent according to [20]. The exhaust gas properties are modelled as properties of air, while the error caused by neglecting combustion products should not be more than 2 % [66]. The thermal conductivity and dynamic viscosity are also taken from [66], whereas the dynamic viscosity was submitted into CFX with Sutherland's Formula. The specific heat capacity at constant pressure has an assumed constant value of 1141 Jkg⁻¹K⁻¹ for heat-up and 1009 Jkg⁻¹K⁻¹ for cool-down, as well as density with a value of 0.348 kg m⁻³ for heat-up and 0.995 kg m⁻³ for cool-down [66]. The molar mass is also a constant 28.96 kg kmol⁻¹, which is the conventional value for air, found in many handbooks.

The properties of solid are the same for heat-up and cool-down: the temperature-dependent c_p and ρ from Figure 4.6 and the constant molar mass 55.85 kg kmol⁻¹, which is again the conventional value for cast irons found in many handbooks.

The steady state simulations were executed with the low Reynolds $k\omega$ -SST turbulence model, which resolves the thermal boundary layer well [20].

Mesh quality was tested on two levels. At first, the convergency of the solution was tested to be independent of mesh size, which is depicted in Figure 4.26. The main monitored unit was area integral of wall heat flux (i.e. heat transfer rate from the CHT Q_{CHT}) on both the fluid and solid side. Apart from the Q_{CHT} , other quantities were monitored during the solution, to assure a convergent state. A low value of residuals with values of $3.67 \cdot 10^{-4}$ or below were achieved with a single precision solver. By refining the mesh by

25 % from 406k to 509k elements, the Q_{CHT} changed at heat-up from 1124.1 W to 1125.1 W which is 0.09 %, and at cool-down the value 18.5 W did not change on a recognizable level. Secondly, a prism layer, depicted in Figure 4.27, was refined until the dimensionless wall distance y^+ was less than 1. This guarantees proper resolution of temperature gradient in the boundary layer [20]. The highest present y^+ value was $y^+ = 0.55$ and its distribution at the fluid-solid CHT interface is in Figure 4.28. Note that the author managed to create a mesh of sufficient quality with the ANSYS Academic license, which for CFX limits the amount of elements to 512k.

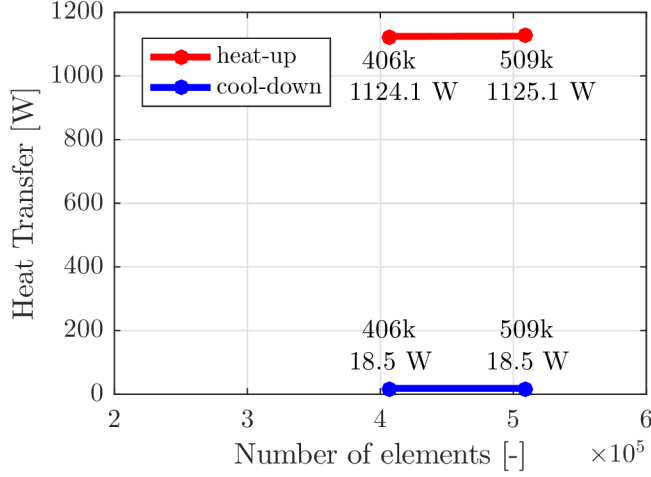


Figure 4.26: Performed mesh independence study

The values of Q_{CHT} can be analytically verified with an energetic balance equation. For the constant c_p and ρ , the theoretical heat transfer rate Q_{theor} is described by Equation 4.8 [81].

$$Q_{theor} = \dot{m}c_p T_{\Delta} \quad (4.8)$$

where T_{Δ} is the exhaust gas temperature drop (inlet–outlet), which was measured from the computed cases – for the heat-up the $T_{\Delta} = 25.3^{\circ}\text{C}$ and for the cool-down the drop was only $T_{\Delta} = 1.6^{\circ}\text{C}$. Then, using the corresponding \dot{m} , c_p and T_{Δ} for heat-up and cool-down phase, the theoretical Q_{theor} can be computed:

$$\text{heat-up: } Q_{theor} = \dot{m}c_p T_{\Delta} = 0.040 \cdot 1141 \cdot 25.3 = 1154.7 \text{ W} \quad (4.9)$$

$$\text{cool-down: } Q_{theor} = \dot{m}c_p T_{\Delta} = 0.012 \cdot 1009 \cdot 1.6 = 19.4 \text{ W} \quad (4.10)$$

The percental difference between the theoretical values and values from the CHT is in the Table 4.3. The error is less than 5 %. If this was a real case, such verification is proposed to assure that the CHT simulations give reasonable values. The T_{Δ} could be also measured in the prototype bench test, and the whole procedure could be additionally validated in the same manner.

Table 4.3: Verification of the Q_{CHT} with Q_{theor}

	Q_{theor} [W]	Q_{CHT} [W]	Difference [%]
heat-up	1154.7	1125.1	-2.6
cool-down	19.4	18.5	-4.6

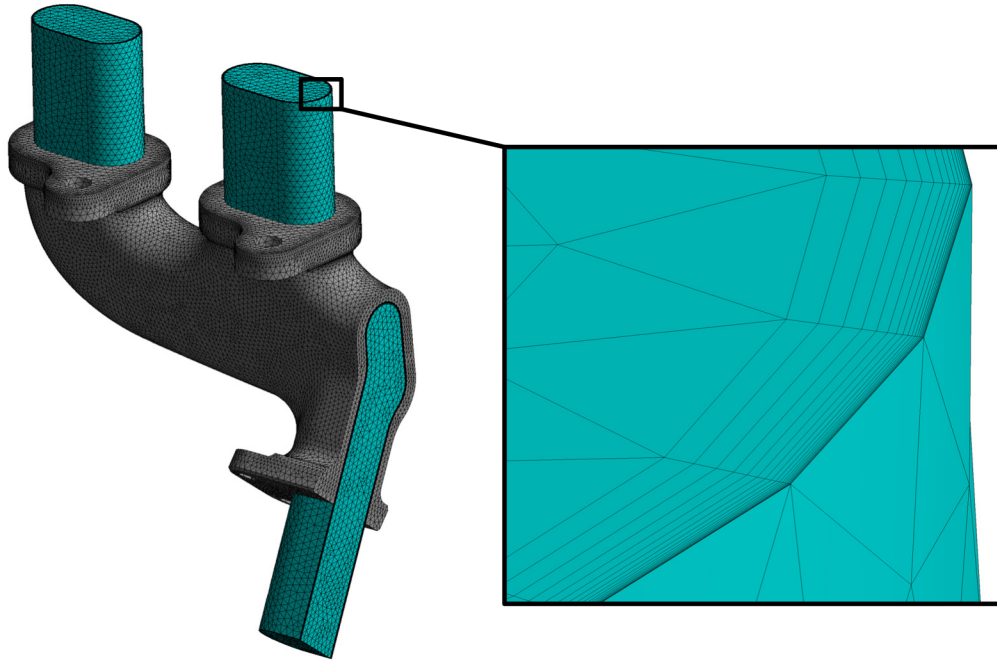


Figure 4.27: Finite volume mesh with detail on the prism layer – 18 elements per total thickness 1 mm

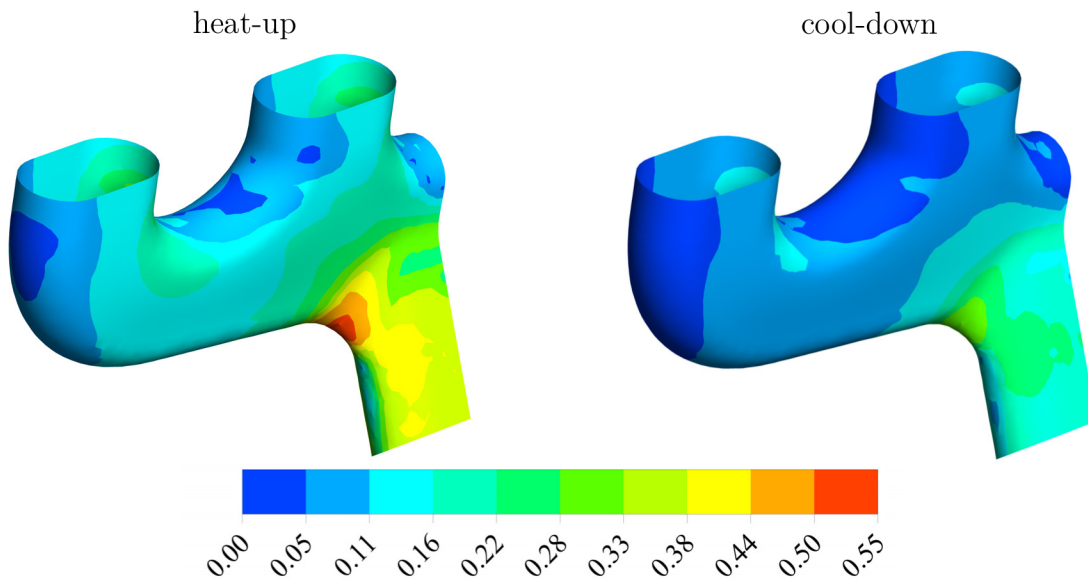


Figure 4.28: Distribution of y^+ on fluid–solid interface

To get the value of HTC , which will be mapped into the subsequent transient thermal FEA, the fluid–solid heat transfer needs to be understood. This can be effectively explained on the one-dimensional steady state CHT in a plane wall model from [31] in Figure 4.29, in which T_{extern} is external wall temperature.

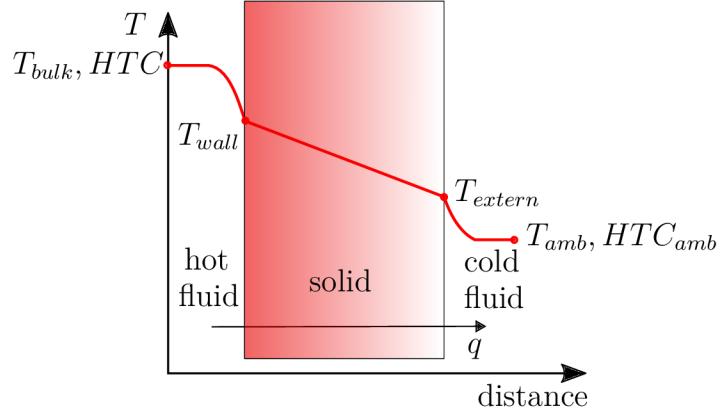


Figure 4.29: Plane steady-state CHT model, reproduced from [31]

In this case, the cold fluid is ambient air and the hot fluid is the exhaust gas. ANSYS CFX offers a quantity called the *Wall Heat Transfer Coefficient*, but this quantity is calculated from the *Wall Adjacent Temperature* which is the temperature from the first finite volume element's centroid next to the wall, and the *Wall Temperature* T_{wall} which is the temperature on the wall of the solid. To be able to get an appropriate value of HTC , a simple recalculation as in [26] needs to be done. Generally, the forced convection boundary condition for the transient thermal FEA is expressed as [31]:

$$q = HTC(T_s - T_0) \quad (4.11)$$

where q is the specific heat transfer rate, T_s is the surface temperature and T_0 is the surrounding temperature [31]. Equation 4.11 is rewritten for the internal surface of the manifold as:

$$q = HTC(T_{wall} - T_{bulk}) \quad (4.12)$$

q and T_{wall} are known from the CHT simulation, so the only unknowns are T_{bulk} and HTC . As [26] suggests, an offset surface from the internal solids wall is created. The offset distance was set to 1 mm in normal direction, which was assumed to be enough to get away from the thermal boundary layer. This gives the T_{bulk} distribution, shown in Figure 4.31. The next step is re-expressing Equation 4.12 as:

$$HTC = \frac{q}{T_{wall} - T_{bulk}} \quad (4.13)$$

With this approach, an appropriate value of HTC is obtained for the subsequent transient thermal FEA. The distribution of the computed HTC is depicted in Figure 4.32, where this quantity was mapped onto the FE mesh.

4.2.3. Finite Element Mesh

The FE mesh of the exhaust manifold was done in ANSYS Workbench 2019 R3 (the same software applies to the following transient thermal and static structural analyses). As mentioned before, apart from the analyzed exhaust manifold, the bolts and engine head dummy are present in subsequent analyses (same as in [18, 27]). The mid-node quadratic elements were used for the FE mesh. At least 2 elements per thin wall are present. The finite element mesh, depicted in Figure 4.30, contains 224k nodes, which is within the limits of the ANSYS Academic license.

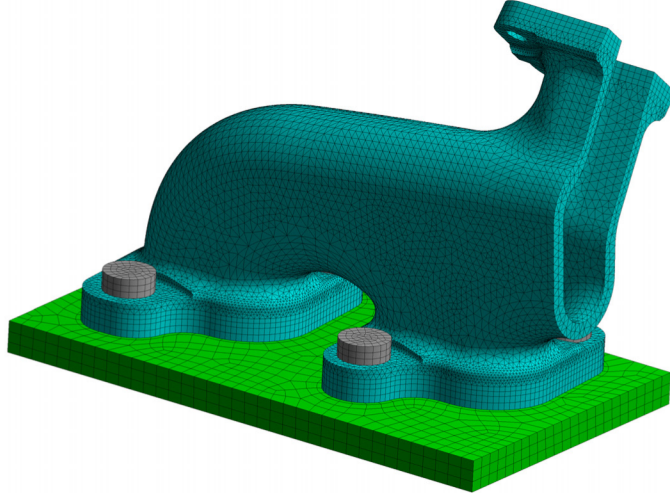


Figure 4.30: Finite element model of exhaust manifold assembly

4.2.4. Transient Thermal Finite Element Analysis

The transient thermal FEA is one-way coupled with the subsequent structural analysis. It is used for the calculation of spatial temperature distribution on the component due to forced convection. The transient conduction in solid isotropic material without the internal heat source is governed by Equation 4.14 [24]:

$$\lambda \left(\frac{\partial^2 T}{\partial x^2} + \frac{\partial^2 T}{\partial y^2} + \frac{\partial^2 T}{\partial z^2} \right) = \rho c_p \frac{\partial T}{\partial t} \quad (4.14)$$

where t denotes time, x , y and z are a spatial coordinates. The physical properties c_p , λ and ρ are known from Figure 4.6. As mentioned before, the transient thermal analysis starts with mapping the T_{bulk} and HTC from the CHT analysis onto internal surfaces of manifold. This can be done efficiently in the ANSYS Workbench *External Data* module. The T_{bulk} and HTC obtained in CHT simulation are exported into a .csv table and then mapped onto the FE mesh as in [41, 51]. The visual verification of T_{bulk} gained in CHT analysis and mapped on the FE mesh is in Figure 4.31, and the mapped HTC is in Figure 4.32.

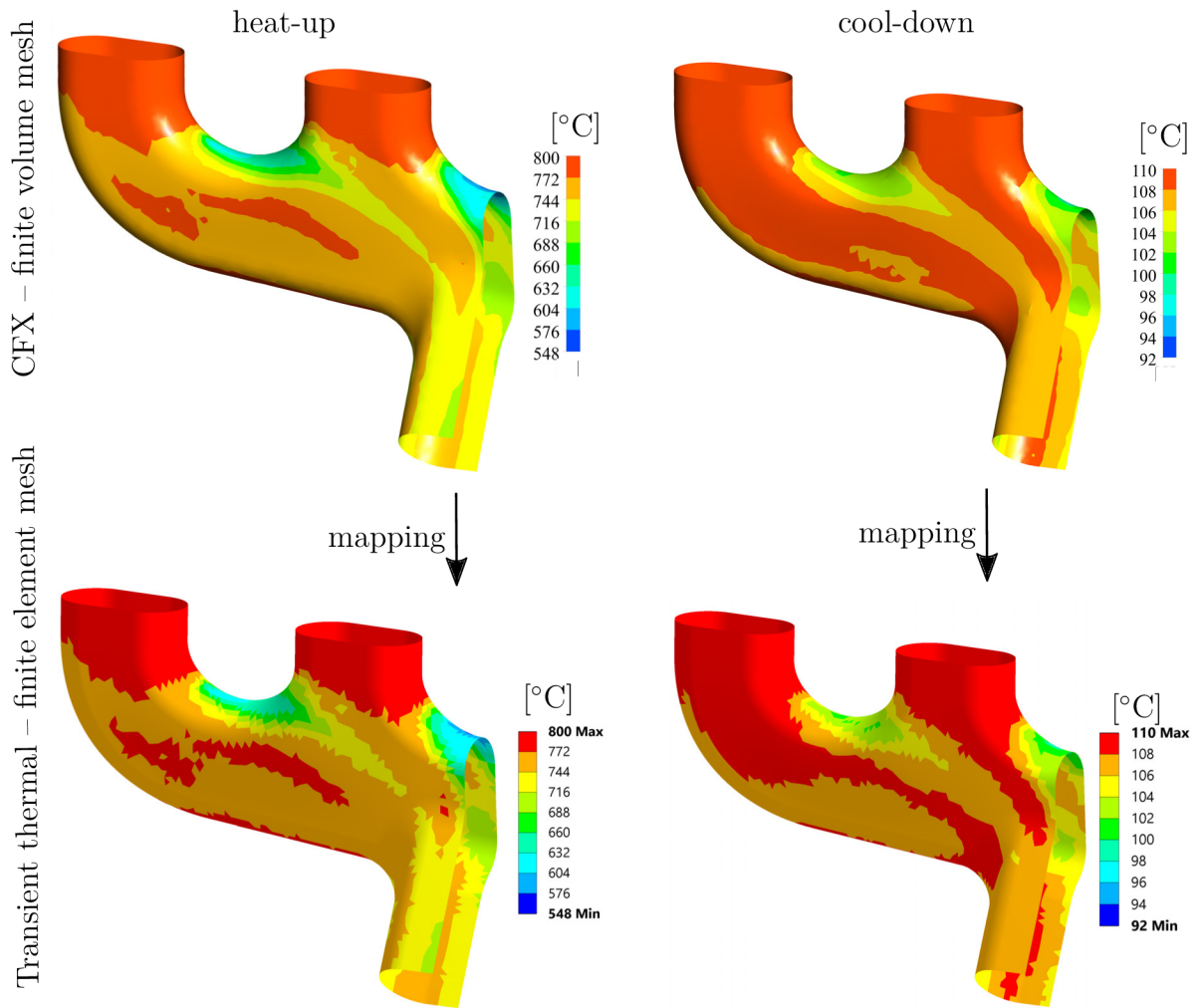


Figure 4.31: Verification of mapped bulk temperature T_{bulk}

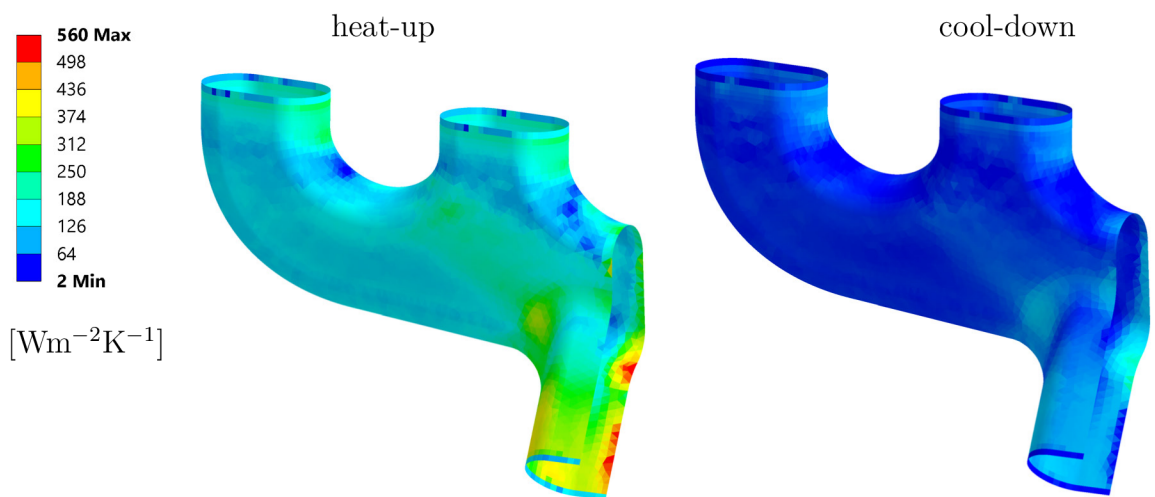


Figure 4.32: Computed HTC mapped on FE mesh

The mapped boundary conditions are ramped according to the thermal shock profile (Figure 4.24), the same as in [37]. The thermal contacts are depicted in Figure 4.33 and their definition is in Table 4.4. The value of thermal contact conductance was defined on the basis of [78].

Table 4.4: Thermal contacts in transient thermal simulation

contact pair	type	formulation	contact conductance
bolts – engine head dummy	bonded	MPC	-
bolts – manifold	bonded	Aug. Lagrange	$1900 \text{ Wm}^{-2}\text{K}^{-1}$
manifold – engine head dummy	bonded	Aug. Lagrange	$1900 \text{ Wm}^{-2}\text{K}^{-1}$

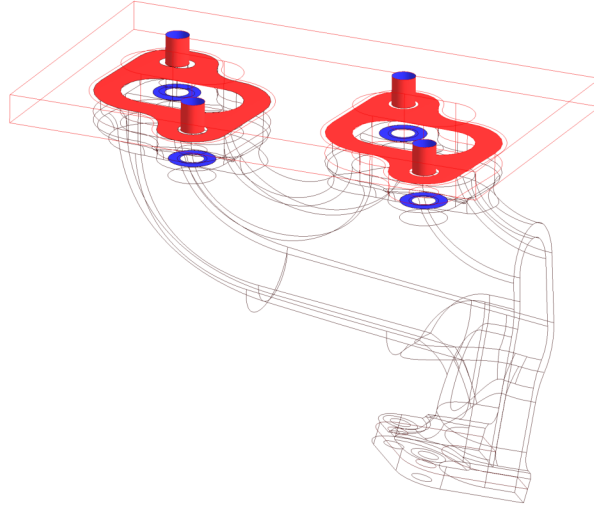


Figure 4.33: Contact pairs in transient thermal simulation

The surfaces on the plane of symmetry have no boundary conditions (i.e. natural boundary conditions). The supposed effect of the water-cooled engine head is modelled with placing a convection boundary condition of $HTC = 2000 \text{ Wm}^{-2}\text{K}^{-1}$ and $T_{bulk} = 200^\circ\text{C}$ on the inner face of the engine head dummy (i.e. the upper face in Figure 4.34). The rest of the external surfaces have the same boundary condition as in Subsection 4.2.2 – $T_{amb} = 77^\circ\text{C}$ and $HTC_{amb} = 50 \text{ Wm}^{-2}\text{K}^{-1}$ [39], modelling the natural convection with radiation taken indirectly in these coefficients. The amount of thermal shock cycles have been chosen in order to obtain stable cycle, the same as in [14] – 3 cycles were enough. The obtained spatial temperature distribution is together with the thermal shock profile and the corresponding time moment in Figure 4.34.

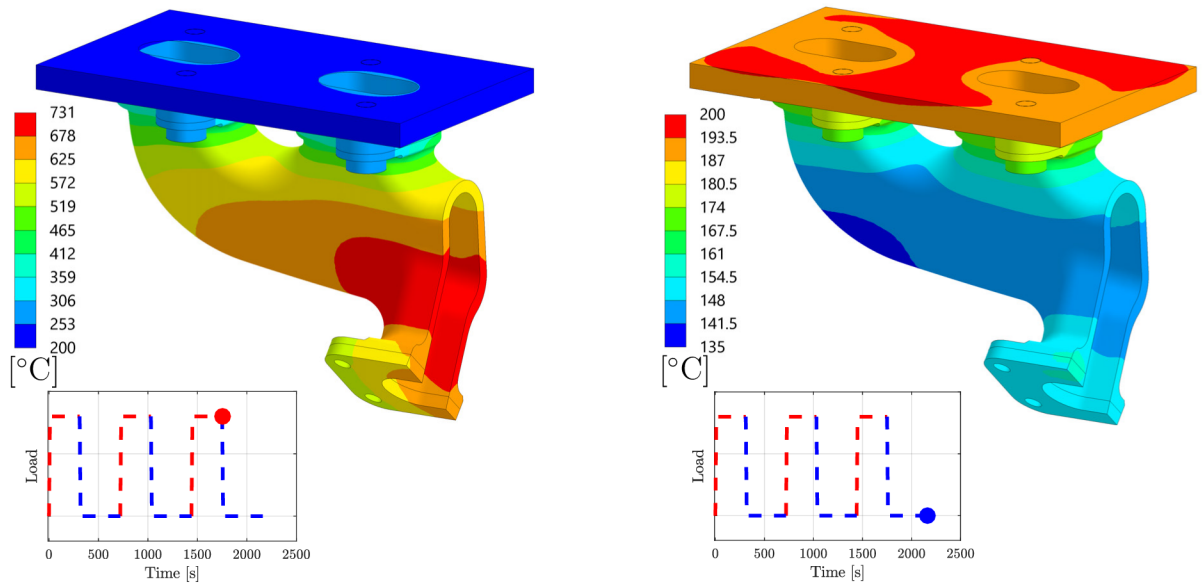


Figure 4.34: Spatial temperature distribution at heat-up and cool-down phase of thermal shock profile, inspired by [51]

Additionally, the time-temperature dependency of the node with the maximum temperature was plotted in Figure 4.35:

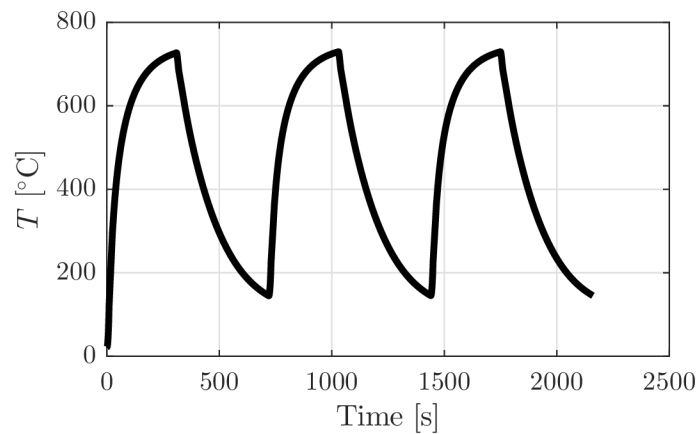


Figure 4.35: Time-temperature history at the node where the maximum occurs

Note that for the heat-up phase, the HTC was increased by a factor of 1.3 and T_{bulk} by a factor of 1.2, in order to obtain higher temperatures. With this and other adjustments (calibrating the contact conductance, adjusting ambient conditions, adjusting cooling at engine head dummy face), the temperature magnitude can be calibrated with experimental measurements. Normally when there are financial resources, a set of thermocouples is attached to several external locations of the exhaust manifold prototype, and the time-temperature dependency is known at these locations. At this point, if this measurement was available, such calibration and validation should be performed as in [14, 18, 47, 55, 70]. The proposal of validation of the results is described later in Subsection 4.3.3.

4.2.5. Structural Finite Element Analysis

The next step is imposing the temperature field in the form of thermal displacements into the structural simulation. The one-way coupled problem was modelled within the ANSYS Workbench Environment. The workflow is depicted in Figure 4.36.

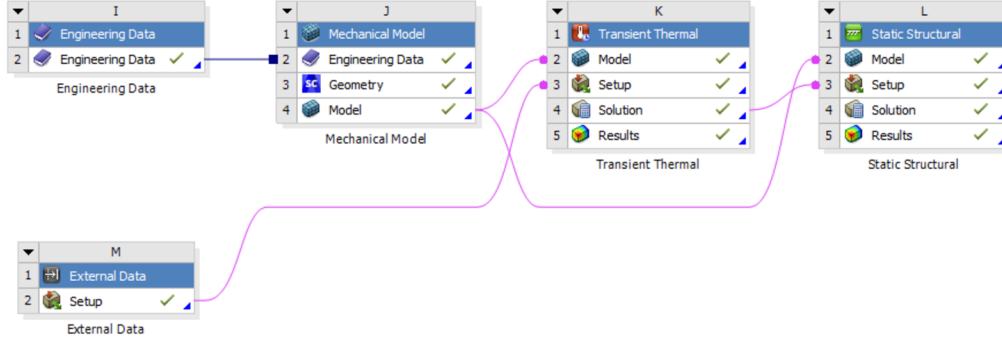


Figure 4.36: Simulation workflow in ANSYS Workbench

In the *Engineering Data* module, a material model is defined. In the *External Data* module, the HTC and T_{bulk} values for the heat-up and cool-down phases obtained in the CHT simulation are imported. Then in the *Mechanical Model* module, the FE mesh was created. Subsequently in the *Transient Thermal* module, 3 thermal shock cycles were modelled in transient thermal simulation as described above. Regarding the final *Static Structural* module, thermal displacements are calculated using the α coefficient (from Figure 4.6) from the last stable thermal shock cycle, with an elasto–plastic material model. This models a representative structural cycle, which is later used for fatigue life prediction. Note that the only temperature-independent property was Poisson’s ratio μ , which was assumed to be a standard value of 0.3 for all components.

The contact pairs remain the same as in Figure 4.33, but their definition was switched and is presented in Table 4.5:

Table 4.5: Contacts in structural simulation

contact pair	type	formulation	friction coefficient
bolts – engine head dummy	bonded	Aug. Lagrange	-
bolts – manifold	frictional	Aug. Lagrange	0.2
manifold – engine head dummy	frictional	Aug. Lagrange	0.2

The internal pressure was disregarded [55]. There is no gasket between the manifold and engine head dummy: this could, however, be added; and the contact pressure could be investigated with respect to sealing as in [18]. The bolt shanks are 8 mm in diameter and the bolt heads are 16 mm in diameter. Their axial pre-load is 20 kN [54]. The diameter of the bolt holes is slightly greater than the diameter of the bolt shanks, allowing lateral motion of the manifold [54]. The plane of symmetry is modelled using a *Frictionless support* boundary condition, which prescribes fixed displacement to the normal direction of the surface (i.e. symmetry). The engine head is supposed to be bulky and stiff, therefore the nodes on the base of the engine head dummy have prescribed fixed displacement in the normal direction (global z direction, as well using *Frictionless support*). One node on the engine head dummy has fixed all degrees of freedom in order to have a constrained model. This allows the engine head to expand freely in the two lateral directions, modelling its thermal expansion [54]. The above-mentioned structural boundary conditions are

depicted in Figure 4.37. The spatial temperature field is taken from the last stabilized thermal cycle in discrete time points, with each time point representing a load step in the structural simulation.

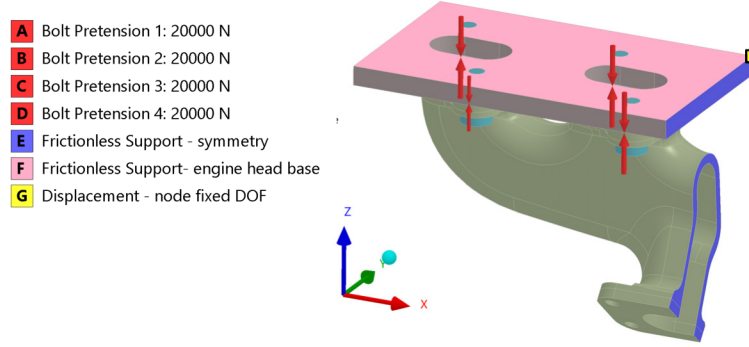


Figure 4.37: Structural boundary conditions

4.3. Fatigue Life Prediction

4.3.1. Fatigue Life Model

To be able to determine the number of cycles to failure N_f , the results are post-processed using the fatigue life model. Note that based on the experimental data, N_f was determined when a 5% drop in maximum stress occurred, in comparison to the stabilized state [65]. The following two different approaches were used in this thesis.

Energy-based Criterion

At first, an energy-based fatigue life criterion, proposed and specifically used in [65] for uniaxial LCF and OPTMF tests of SiMo 4.06 material, was used in this thesis. This criterion uses the dissipated energy per cycle w , which is a product of a numerical integration over the stabilized cycle [65, 68]:

$$w = \int_{\text{cycle}} \boldsymbol{\sigma} : \dot{\boldsymbol{\varepsilon}}_{pl} dt \quad (4.15)$$

where $\dot{\boldsymbol{\varepsilon}}_{pl}$ is the mechanical plastic strain rate tensor and $:$ denotes the double dot product. According to Bartošák et al. [65], the temperature term is not needed, since the $w - N_f$ dependency is not significantly influenced by temperature. This makes the post-processing simple, since there are no temperature-dependent terms. The oxidation is indirectly taken in this criterion. The dissipated energy per cycle w – number of cycles to failure N_f equation is [65]:

$$w = AN_f^B \quad (4.16)$$

where A and B are material parameters obtained by the least squares fitting procedure from the uniaxial tests. Their values are presented in Table 4.6. To get the prediction of fatigue life, the Equation 4.16 is re-expressed:

$$N_f = (A^{-1}w)^{B^{-1}} \quad (4.17)$$

Table 4.6: Constants obtained from fitting procedure of the experimental LCF and OPTMF data by Equation 4.17 [65]

A [mJmm ⁻³]	B [-]
87.096	-0.624

The validation of criterion from Equation 4.17 is done in Figure 4.38 with factor 2 and factor 5 bands [67]. In this Figure, the observed and predicted N_f for the LCF and OPTMF tests, based on the provided uniaxial test data in [65], are plotted.

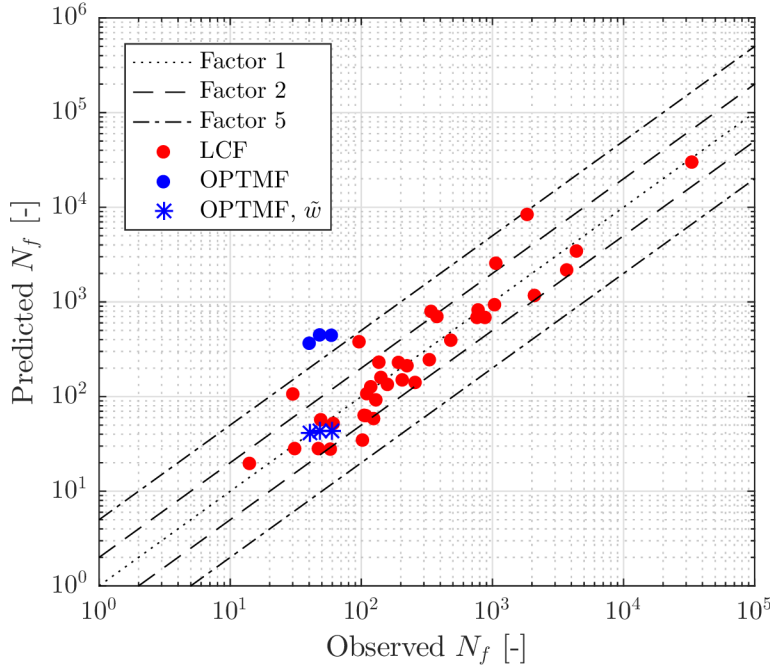


Figure 4.38: Validation of the fatigue life model – observed and predicted N_f for energy-based criterion, recreated from the data in [65]

It is evident that the prediction of OPTMF tests is out of the factor 5 band. This is because of the mean stress influence. As mentioned before, the mean stress also influences the fatigue life. Therefore Bartošák et al. [65] expanded the relationship with the additional material parameter $\alpha_{\tilde{w}}$. This material parameter takes into account the mean stress effect in the form of the stress ratio R_σ , defined for uniaxial cycle as $R_\sigma = \frac{\sigma_{min}}{\sigma_{max}}$. The Equation 4.17 is modified, and the modified dissipated energy \tilde{w} criterion was introduced [65]:

$$\tilde{w} = AN_f^B + \alpha_{\tilde{w}}(-1 - R_\sigma^{-1}) \quad (4.18)$$

The R_σ is equal to -1 for LCF tests (fully reversed cycle), and for the OPTMF tests the R_σ is approximately equal to -0.4 [65]. The value of the parameter $\alpha_{\tilde{w}}$ was identified by the fitting procedure in [65]. By applying this modified criterion, the OPTMF tests can be predicted better, as visible in the Figure 4.38. However, for the multiaxial stress state and general load cycle, R_σ is not so straightforward to evaluate. The identification of R_σ from the multiaxial stress state would lead to a CPA, and its implementation is part of the further possible work on this topic, described in Chapter 5. Therefore, only the simple dissipated energy per cycle criterion from Equation 4.17 was used for the fatigue

life prediction. The multiaxial implementation is evident from Equation 4.15 – it is a sum of six integrals per cycle [79]. Apart from the temperature-independence benefit, energy-based approaches can be used for non-proportional loading. However, energy is a scalar quantity, therefore it does not account for the fatigue damage nucleation and accumulation observed on specific planes [79]. The implementation of the energy-based criterion was realized as *User Defined Result* in ANSYS Workbench, since there are no temperature-dependent terms. The energy-based (i.e. dissipated energy per cycle) fatigue life criterion was used for same case of TMF of the exhaust manifold in [16, 17, 38]. According to Charkaluk [16], the energy-based approach is more suitable for multiaxial TMF cases, compared to standard strain-based approaches, because of its clear multiaxial formulation. Additionally, the energy-based criterion with two modifications have been used for TMF fatigue life prediction of exhaust manifold in [40].

Strain-based Criterion

Secondly, a strain-based approach was used. The relationship describing the fatigue life prediction is a well-known Basquin and Manson–Coffin law [5]:

$$\varepsilon_a = \frac{\Delta\varepsilon}{2} = \frac{\sigma'_f}{E}(N_f)^a + \varepsilon'_f(N_f)^b \quad (4.19)$$

where σ'_f is fatigue strength coefficient, a is fatigue strength exponent, ε'_f is fatigue ductility coefficient, and b is fatigue ductility exponent [32]. Unlike the energy-based criterion, the strain-based fatigue life model used in this thesis is temperature-dependent. The coefficients were calibrated from the data in [65, 70]. The constants identified in the fitting procedure are in Table 4.7. The individual calibration at each temperature level is depicted in Figure 4.40. In addition, the strain-based approach from Equation 4.19 does not account for the effect of the mean stress σ_m in the cycle. Thus, the mean stress corrections were proposed, such as the Morrow – Equation 4.20, or the Swift–Watson–Topper (SWT) – Equation 4.21 [32]. The validation of strain-based fatigue life models is in Figure 4.39. The uniaxial LCF tests are predicted better when compared to energy-based criterion (Figure 4.38) since most of the data are scattered within the Factor 2 band. Additionally, it is evident that the mean stress effect in the OPTMF test ($\sigma_m = 141$ MPa [65]) has again significant influence on the fatigue life prediction. The SWT correction has the closest N_f prediction to the experimentally-observed values as seen in Figure 4.39. However, the implementation of mean stress correction models (Morrow, SWT) for the multiaxial stress state is rather difficult, leading again to the CPA approach. This could be a possibility for further research, as described in Chapter 5. For example, Morrow’s equation was used on the same problem (TMF prediction of exhaust manifold) in [55]. The author proceeded with the essential temperature-dependent Basquin–Manson–Coffin relationship from Equation 4.19. The same Basquin–Manson–Coffin approach was done for TMF life prediction of the exhaust manifold in [63]. An equivalent strain approach was used as strain-based multiaxial criteria, as described in [79]. This means that the strain amplitude ε_a is expressed using the equivalent strain amplitude $\varepsilon_{equiv,a}$ with respect to maximum shear strain theory – Equation 4.22, where $\varepsilon_{1,a}$ is the maximum principal strain amplitude and $\varepsilon_{3,a}$ is the minimum principal strain amplitude. This is one of the most commonly-used equivalent strain approaches [79]. Note that Equation 4.22 is used only for the multiaxial formulation, whereas in Figure 4.39 the $\varepsilon_a = \varepsilon_{1,a}$ (meaning the

validation figure is not fully consistent with the multiaxial formulation). However, the difference between these uniaxial and multiaxial formulations cannot be more than 15% for $\mu=0.3$. This is explained in the Appendix C of the thesis. In contrast to energy-based criterion, the strain-based approach is not suitable for non-proportional loading, according to [79].

$$\varepsilon_a = \frac{\Delta\varepsilon}{2} = \frac{\sigma'_f - \sigma_m}{E}(N_f)^a + \varepsilon'_f(N_f)^b \quad (4.20)$$

$$\sigma_{max}\varepsilon_a = \sigma_{max}\frac{\Delta\varepsilon}{2} = \frac{(\sigma'_f)^2}{E}(N_f)^{2a} + \sigma'_f\varepsilon'_f(N_f)^{(a+b)} \quad (4.21)$$

$$\varepsilon_a = \varepsilon_{equ,a} = \frac{\varepsilon_{1,a} - \varepsilon_{3,a}}{1 + \mu} \quad (4.22)$$

Table 4.7: Constants obtained from fitting procedure of the experimental LCF data from [65, 70] by Equation 4.19

T [°C]	20	400	550	650	750
σ'_f [MPa]	826	656	487	234	95
a [-]	-0.083	-0.066	-0.068	-0.043	-0.032
ε'_f [-]	0.026	0.015	0.086	0.141	0.159
b [-]	-0.431	-0.404	-0.604	-0.592	-0.596

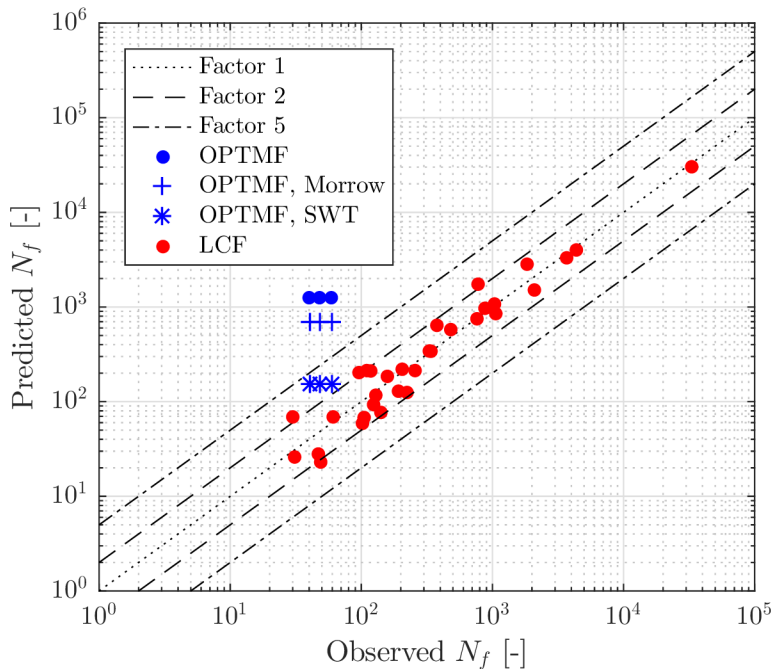


Figure 4.39: Validation of the fatigue life model – observed and predicted N_f for strain-based criterion, created from the data in [65, 70]

Since the strain-based criterion has temperature-dependent terms, the post-processing had to be treated accordingly. A code in MATLAB R2016a was developed, which works with standard FEA outputs – T (transient thermal analysis) and ε_a from Equation 4.22

(static structural analysis) in each integration point. These quantities are imported to the code at the time corresponding to the end of the heat-up phase (which is strain and temperature-wise the most critical moment). A linear interpolation is done between the constants from Table 4.7, and E from Figure 4.2. The same approach of strain–life curve temperature interpolation is mentioned in [28]. Following this, the fatigue life prediction N_f is done by solving Equation 4.19 numerically, with the bisection method in each integration point; since there is no explicit expression of N_f from this equation. Finally, the spatial distribution of predicted N_f is mapped back on the original mesh to be displayed as a contour plot.

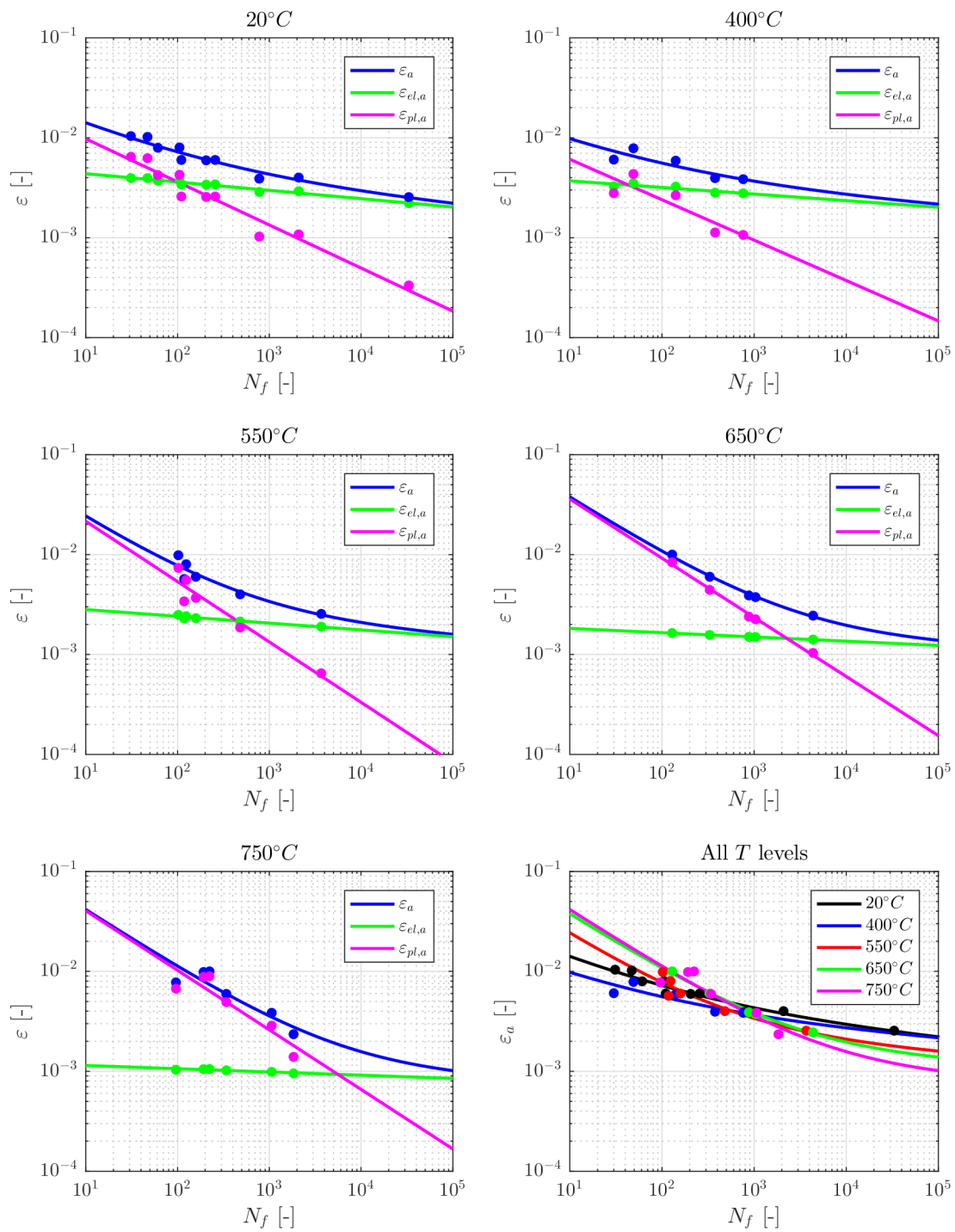


Figure 4.40: Calibrated Basquin and Manson–Coffin curves at each T level from experimental data published in [65, 70]

4.3.2. Comparison of Used Material and Fatigue Life Models

BKIN, Energy-based Criterion

The maximum total deformation of the exhaust manifold was 1.2 mm. The maximum equivalent stress σ_{eqv} was 454 MPa around the edges of the bolt holes (caused by contact forces from the bolt pretension). The spatial distribution of the aforementioned quantities is in Figure 4.41, and it is plotted in the time moment corresponding to the “end of heat-up phase” (i.e. the time depicted in Figure 4.34 (left) by the red dot).

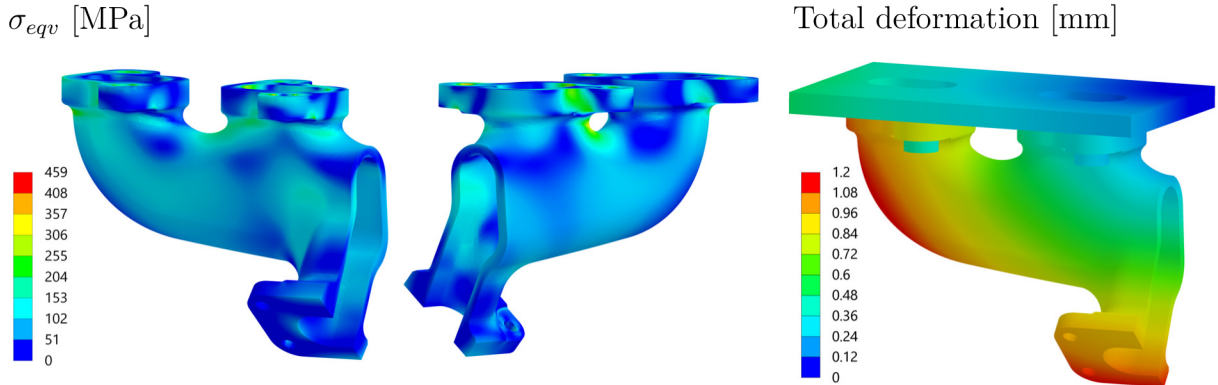


Figure 4.41: σ_{eqv} and total deformation for the BKIN model

The spatial distribution of the equivalent plastic strain range $\Delta\varepsilon_{eqv,pl}$ and N_f^3 prediction using criterion from Equation 4.17 is in Figure 4.42. The criterion was implemented as a *User Defined Result* in ANSYS Workbench post-process. The equivalent plastic strain range $\Delta\varepsilon_{eqv,pl}$ corresponds to the critical areas in the real component [51].

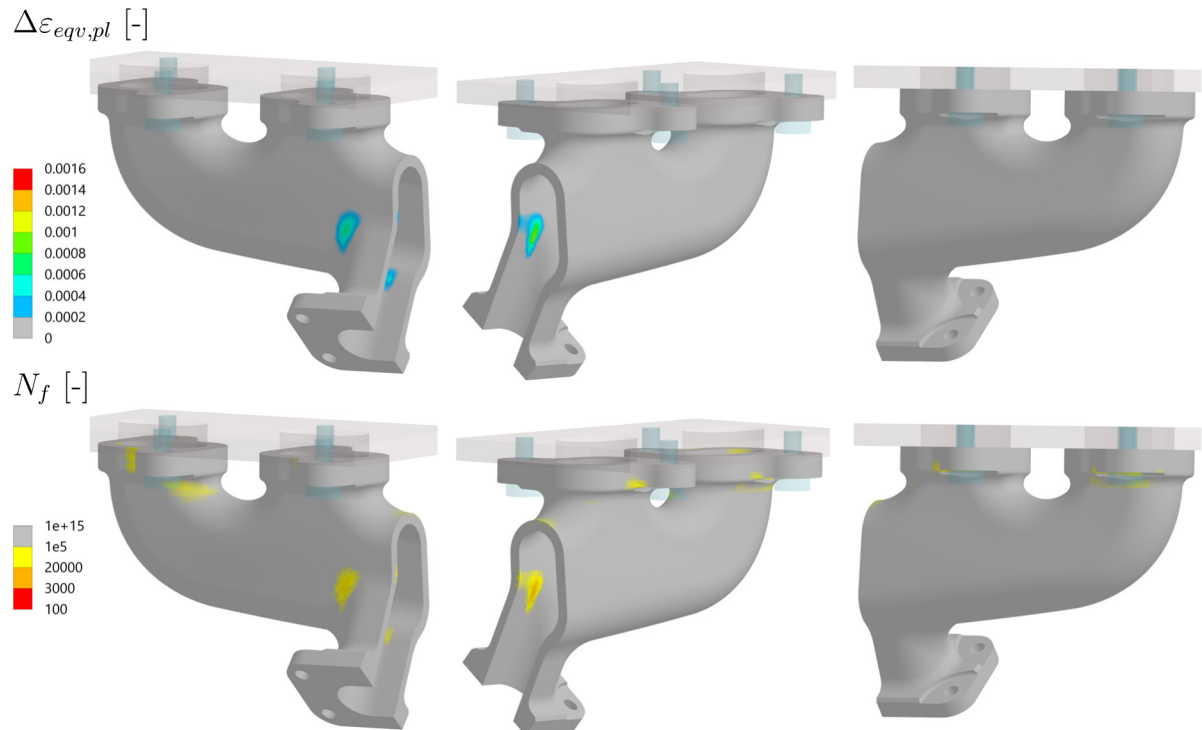


Figure 4.42: $\Delta\varepsilon_{eqv,pl}$ and N_f energy-based for the BKIN model

³Note that N_f is plotted in log-scale in contour plots

The $\Delta\varepsilon_{eqv,pl}$ is related to dissipated energy, therefore we can see that the low life is predicted on the same areas where plasticity occurs. The maximum $\Delta\varepsilon_{eqv,pl}$ was 0.0009 and the minimum N_f 14628. The critical location with the highest plastic strain and lowest predicted life is in Figure 4.43.

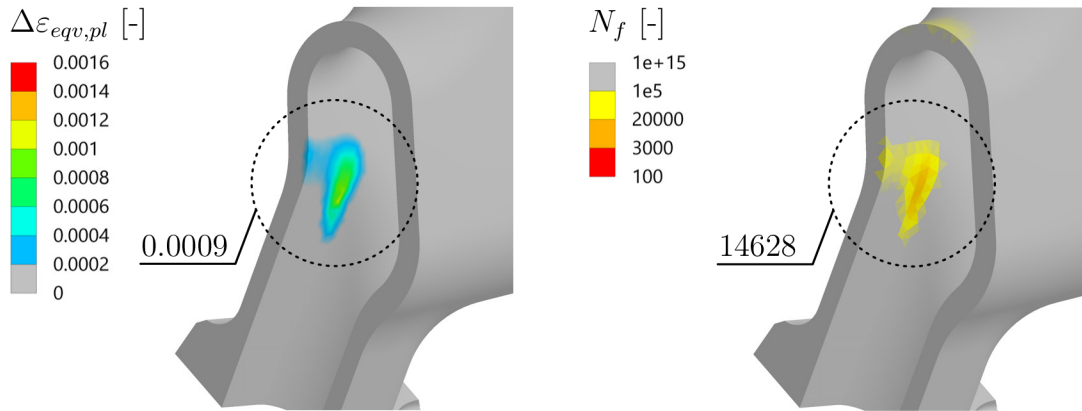


Figure 4.43: Critical location for BKIN model, N_f energy-based, initial coarse mesh

A convergence study with respect to mesh refinement was conducted. This was done by local mesh refinement at the critical location as per Figure 4.44. This was repeated until the result parameter (N_f) did not change significantly with respect to element refinement. The convergence study is plotted in Figure 4.45. At the end of the convergence study, the value of the predicted N_f changed less than 5 % with 50 % element reduction, which was assumed as satisfactory. The maximum $\Delta\varepsilon_{eqv,pl}$ increased to 0.0014, and the N_f decreased to 7933 cycles. These quantities are plotted as a contour plot in Figure 4.46. Note that because of the fact that the criterion is a power law, a relatively small variation in input (in this case w) results in relatively large variation of output (meaning N_f). Hence the results are considerably sensitive to mesh size.

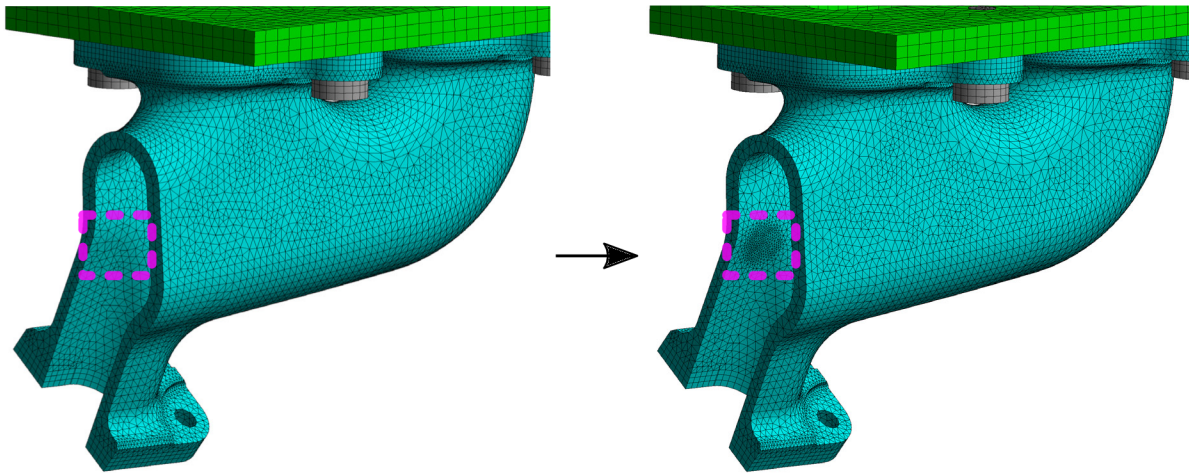


Figure 4.44: Local refinement of the mesh at the critical location

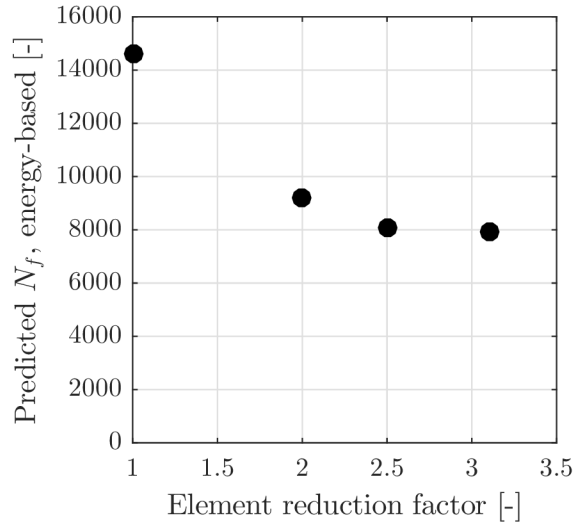


Figure 4.45: Mesh convergence study with respect to N_f for BKIN material model with energy-based criterion

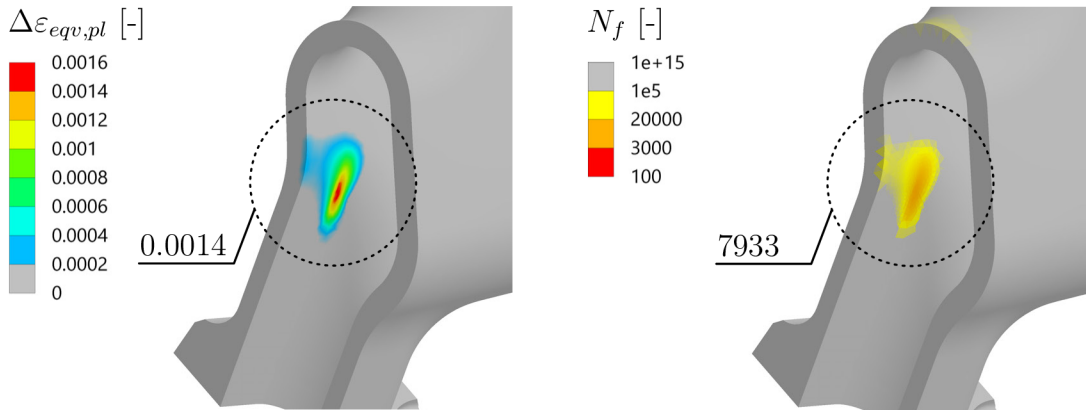


Figure 4.46: $\Delta\varepsilon_{eqv,pl}$ and N_f predicted using an energy-based approach on a refined mesh, BKIN material model

BKIN, Strain-based Criterion

The strain-based criterion was used on an already-refined mesh. That is because of the chronology of the author’s problem-solving. The strain amplitude ε_a , identified by the aforementioned equivalent strain approach with respect to the maximum shear strain theory (Equation 4.22), is depicted in Figure 4.47; as well as the predicted N_f . The temperature of the node containing the critical N_f is 698°C, with $\varepsilon_a = 0.0017$ at the end of heat-up. The critical location remains the same, and the predicted N_f is 16421. Apart from the critical location, the rest of the nodes in the model contained $N_f > 100000$ after post-processing.

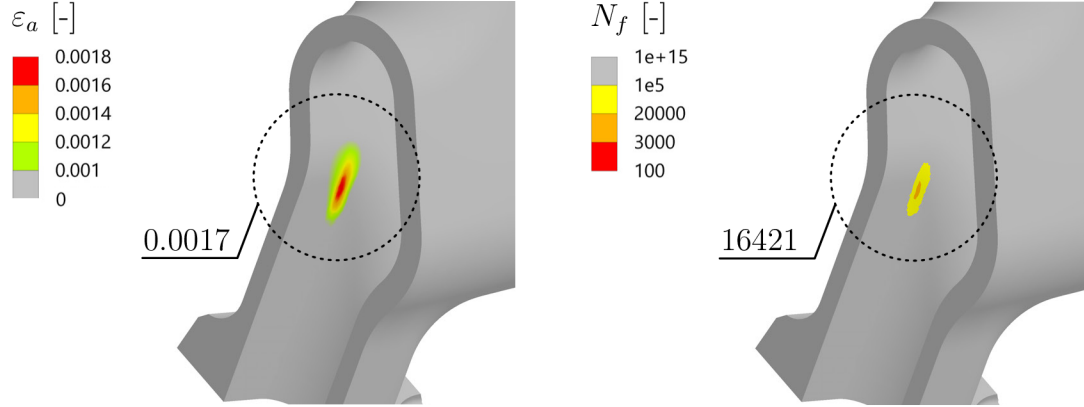


Figure 4.47: ε_a and N_f predicted using the strain-based approach, BKIN material model

Chaboche, Energy-based Criterion

The maximum total deformation of the exhaust manifold was 1.2 mm. The maximum equivalent stress σ_{eqv} was 357 MPa around the edges of the bolt holes (caused by contact forces from the bolt pretension). The spatial distribution of these aforementioned quantities is in Figure 4.48, and is again plotted in the time corresponding to “end of heat-up” (i.e. time depicted in Figure 4.34 (left) by the red dot).

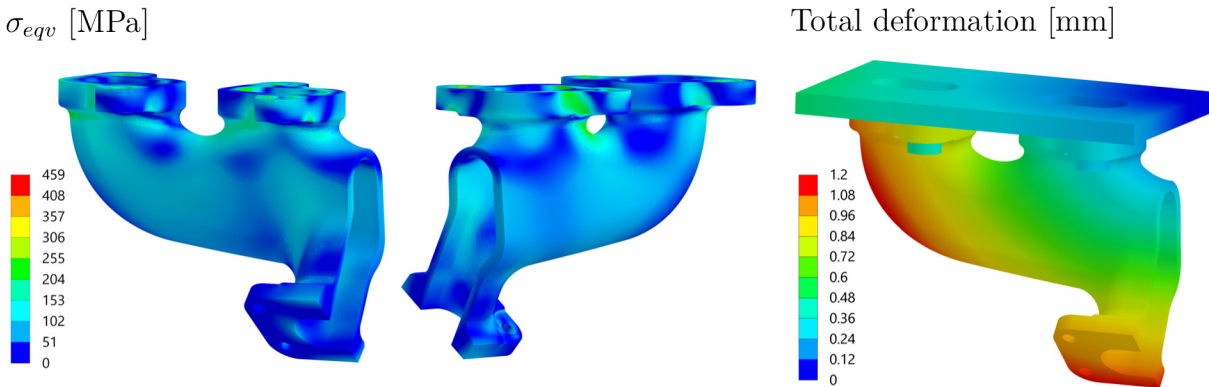


Figure 4.48: σ_{eqv} and total deformation for the Chaboche model

In the same manner, the spatial distribution of the equivalent plastic strain $\Delta\varepsilon_{eqv,pl}$ and the N_f prediction, using criterion from Equation 4.17, is in Figure 4.49.

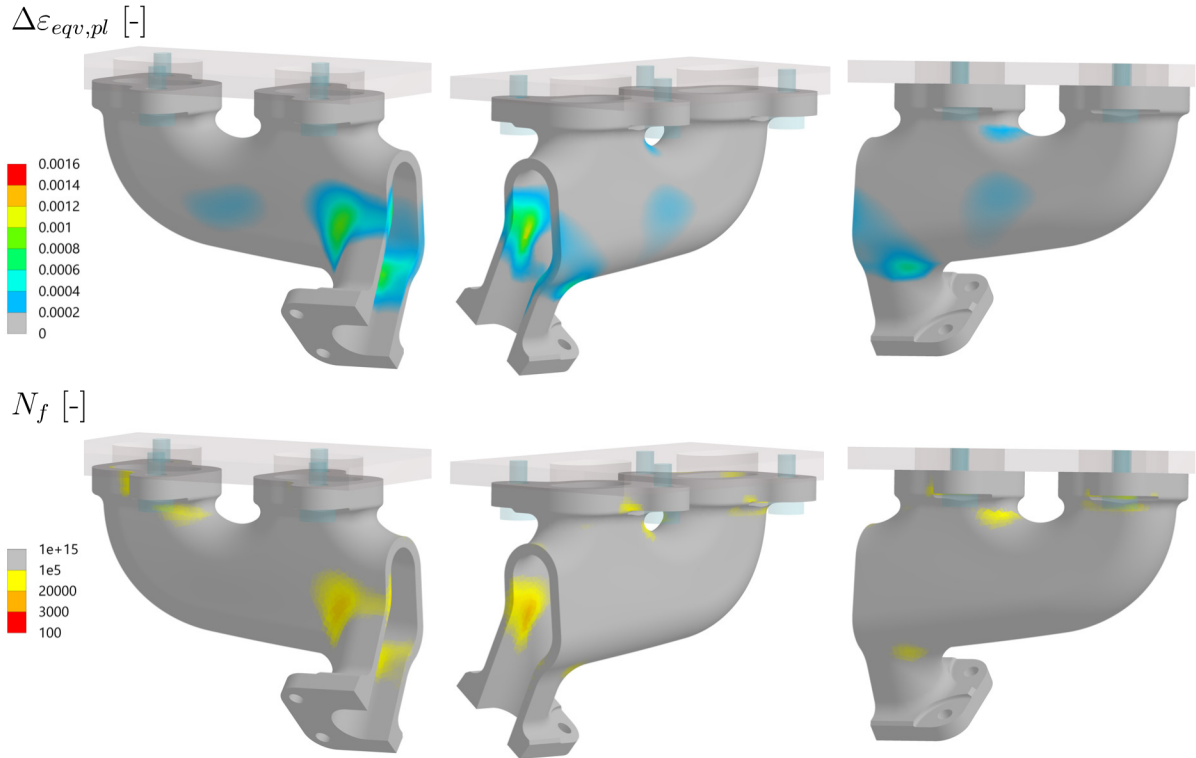


Figure 4.49: $\Delta\varepsilon_{eqv,pl}$ and N_f energy-based for the Chaboche model

The maximum $\Delta\varepsilon_{eqv,pl}$ was 0.0011, and minimum N_f 13959. Some small values of plasticity also occurred around the bolt holes, where previously mentioned high stresses appeared, hence low life was predicted. This phenomena can be also be seen in [55]. This contact area is disregarded, since it does not influence the main function of the exhaust manifold – containing the exhaust gases. If the crack initiates on this bolt hole and flange, it is likely not going to lead to exhaust gas leakage. The cracks that appear on the thin wall are the critical ones, since they lead to the manifold failure – exhaust gas leakage. Therefore, the main critical location was evaluated in Figure 4.50.

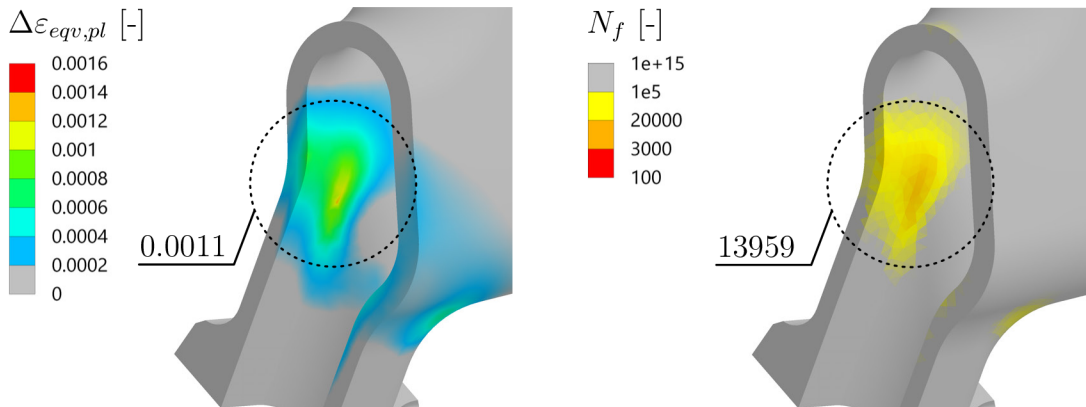


Figure 4.50: Critical location for Chaboche model, N_f energy-based, initial coarse mesh

Again, the mesh convergence study was executed in the same manner as for the BKIN material model. At the end of the convergence study, the value of the predicted N_f again changed less than 5%, with 50% element reduction which was deemed satisfactory. The maximum $\Delta\varepsilon_{eqv,pl}$ increased to 0.0014 and the N_f decreased to 8660 cycles. The mesh

convergence study is plotted in Figure 4.51, and $\Delta\varepsilon_{eqv,pl}$ and N_f on the fine mesh are plotted as a contour plot in Figure 4.52.

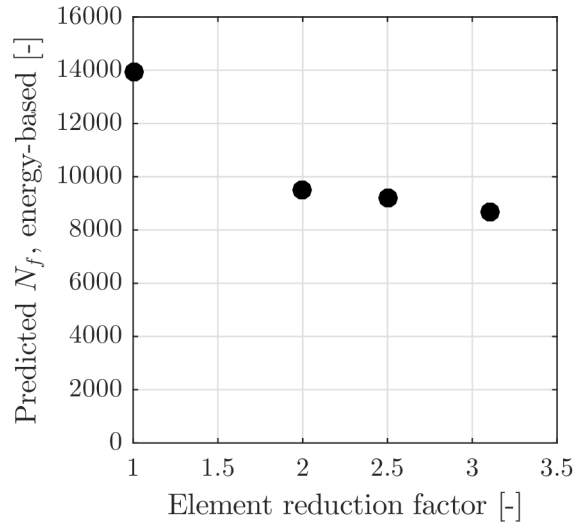


Figure 4.51: Mesh convergence study with respect to N_f for the Chaboche material model with energy-based criterion

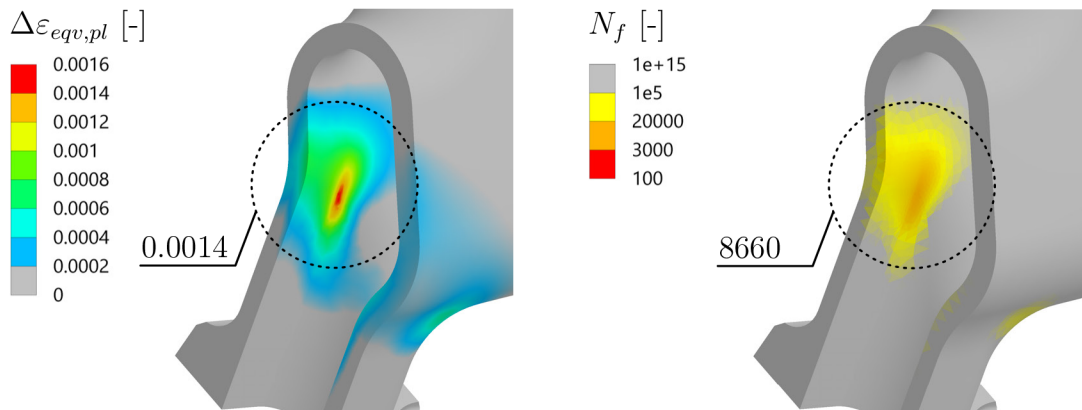


Figure 4.52: $\Delta\varepsilon_{eqv,pl}$ and N_f predicted using energy-based approach on a refined mesh, Chaboche material model

Chaboche, Strain-based Criterion

The same as for the BKIN, the strain-based criterion was used on an already-refined mesh, due to the chronology of the author's problem-solving. The strain amplitude ε_a , identified by the equivalent strain approach with respect to the maximum shear strain theory, is depicted in Figure 4.53; as well as the predicted N_f . The temperature of the node containing the critical N_f is 698°C (the same as the BKIN) with $\varepsilon_a = 0.0016$ at the end of heat-up. The critical location remains the same, and the predicted N_f is 17525. Apart from the critical location, the rest of the nodes in the model contained $N_f > 100000$ after post-processing.

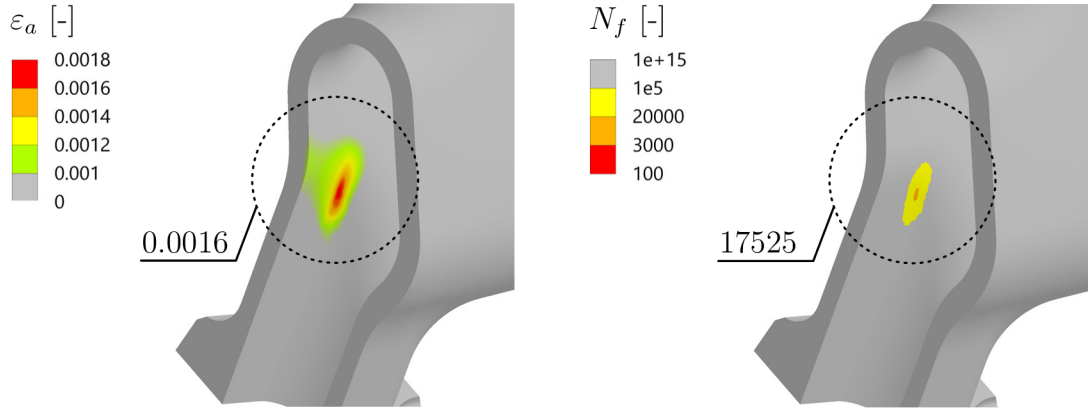


Figure 4.53: ε_a and N_f predicted using strain-based approach, Chaboche material model

Analysis of Results and Discussion

It can be concluded from Figures 4.42 and 4.49 that the BKIN model predicts the plastic deformation on lesser and smaller areas in comparison to the Chaboche model. This is likely caused by adjusting the yield stress magnitude to a greater level than in the experiments as seen in Figure 4.14. From Figure 4.54, it is evident that the critical location is predicted on the same spot, regardless of the material or fatigue life model. The magnitude of the minimum N_f does not differ significantly between the material models, but differs between the fatigue life models. This statement is interpreted graphically in the correlation plots in Figure 4.55. The minimum N_f prediction between fatigue life models is contained within the factor 2 band - Figure 4.55 (left). The discrepancy of a factor of 2 between the models is not unusually high – for example in [40], two similar energetic approaches were compared and the discrepancy between these approaches was of factor of 3 in the critical location.

The absolute values of the predicted minimum N_f in the critical location are in Table 4.8. It can therefore be stated that in this work, the N_f prediction in the critical area is more sensitive to the fatigue life model than to the material model. In addition, an energy-based approach predicts more conservative values on more areas compared to the strain-based approach. An energy-based fatigue life model, combined with the Chaboche material model, predicts TMF on more and larger locations in comparison to the rest of the combined approaches.

Table 4.8: Predicted minimum N_f at critical location, comparison of material and fatigue life models

Material model	Fatigue life model	N_f
BKIN	energy-based	7933
Chab	energy-based	8660
BKIN	strain-based	16421
Chab	strain-based	17525

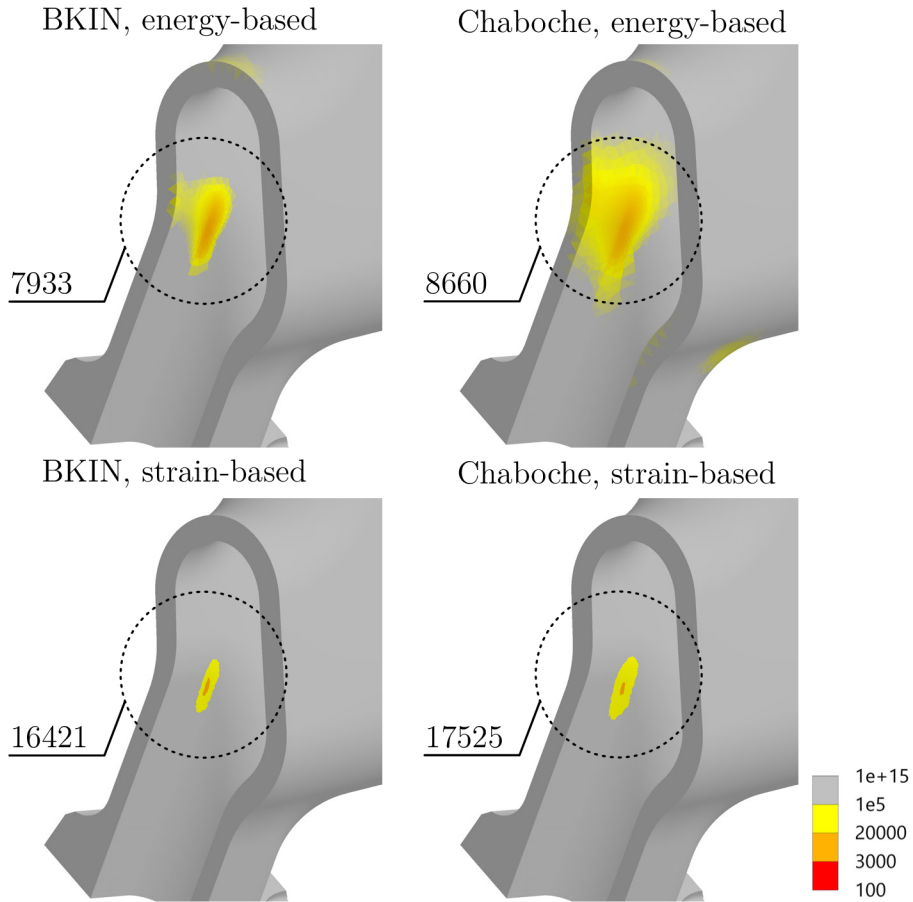


Figure 4.54: Predicted N_f at the critical location, comparison of material and fatigue life models, visual comparison in form of contour plot

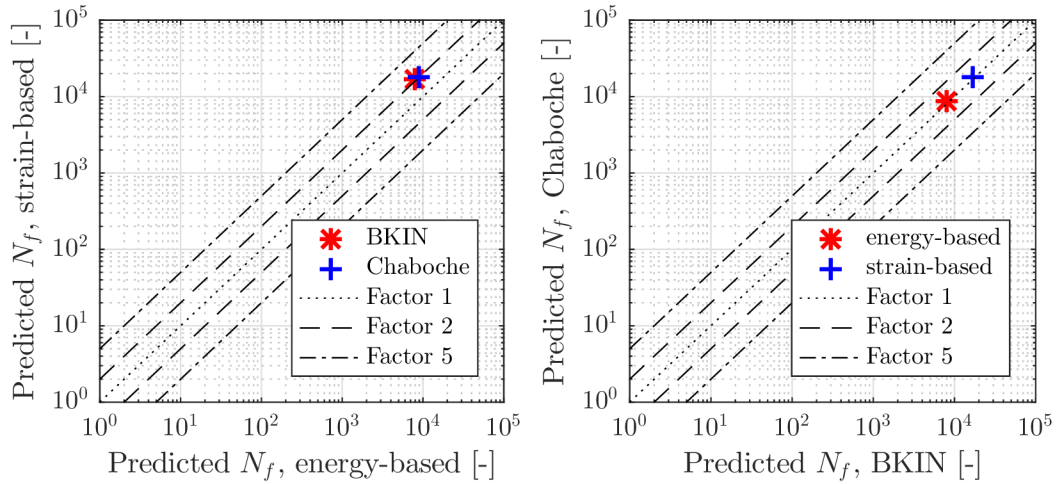


Figure 4.55: Correlation of the predicted minimum N_f at the critical location, (left) with respect to fatigue life models, (right) with respect to material models

4.3.3. Validation of Results

Apart from the experiments conducted on the specimen level, a number of experiments on the component level should also be conducted. This has previously been stated, and is depicted in Figure 3.18. If this was a real case and there were financial resources, the following component experiment is proposed, based on [18, 27, 30, 47, 51, 67, 70]. In the proposed component experiment, the component (exhaust manifold) with gasket is attached to the water-cooled cylinder head. The temperature and mass flow of gas are calibrated on the basis of what the component experience on the real running engine would be (i.e. thermal shock). One such engine simulator was, for example, published in [52], and the approach for the creation of the representative thermal shock on the basis of the real driving conditions is in [16]. During this experiment, several Linear Variable Differential Transformers (LVDTs) and Thermo-Couples (TCs) are attached to the component. The TCs are used for the calibration and validation of transient thermal FE analysis. The LVDTs allow accurate displacements of the component to be measured, which are used for validation of the structural analysis. An example from literature is depicted in Figure 4.56 below [18].

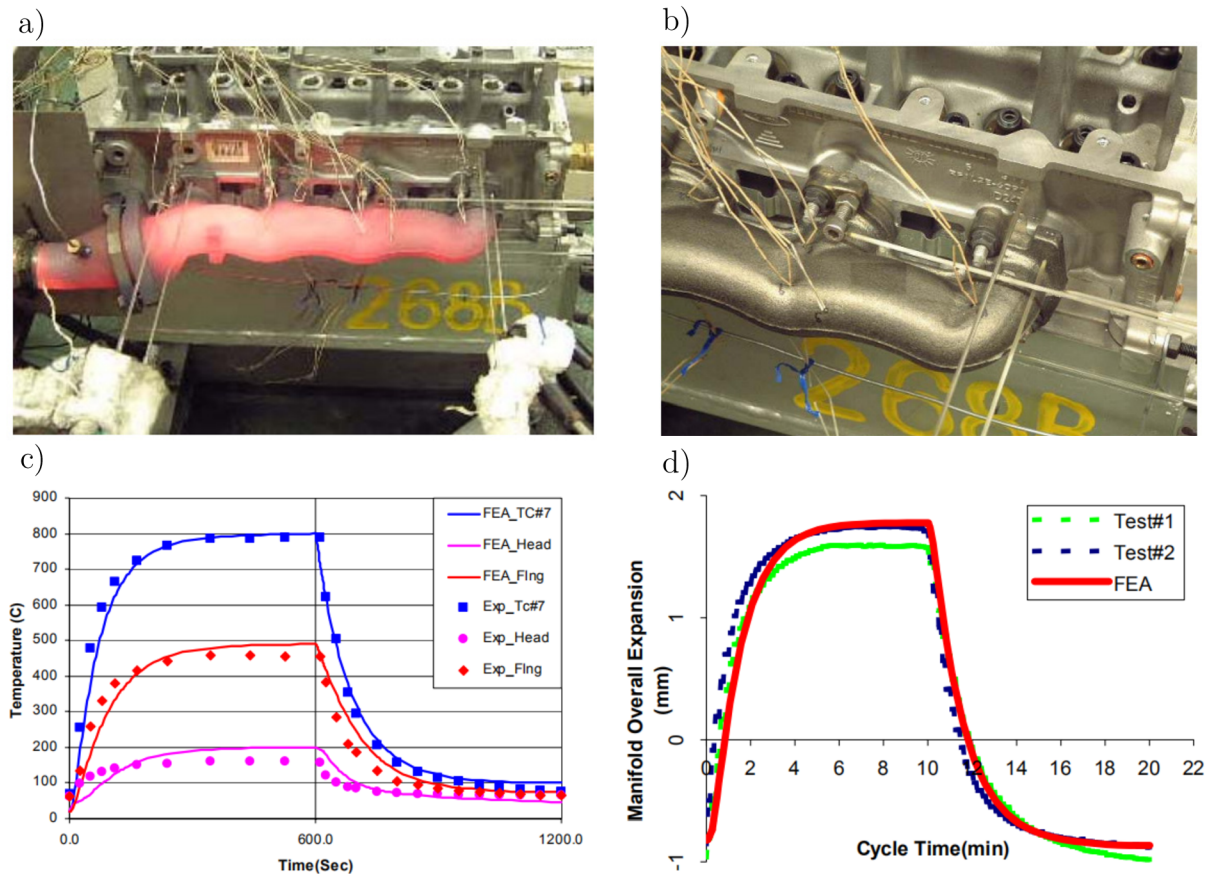


Figure 4.56: a) Experimental setup, b) detail on attached LVDT and TC locations, c) validation of temperature (transient thermal analysis), d) validation of overall expansion (structural analysis) [18]

Additionally, the locations of actual component cracks are validated, i.e. whether the cracks appear on the same locations where the FE model predicts low fatigue life. If possible, the time (proportional to the number of cycles) of the crack appearance should be

noted and compared to the predicted one. However, the N_f from uniaxial data is usually determined with respect to crack initiation, whereas in the component test the crack is likely to be noticed after macro-growth (for example in [47] it was treated by the damage operator with respect to the so-called "technical crack" of 1mm length). Therefore, it is not trivial to correlate these quantities. An example from literature is depicted in Figure 4.57 below [47].

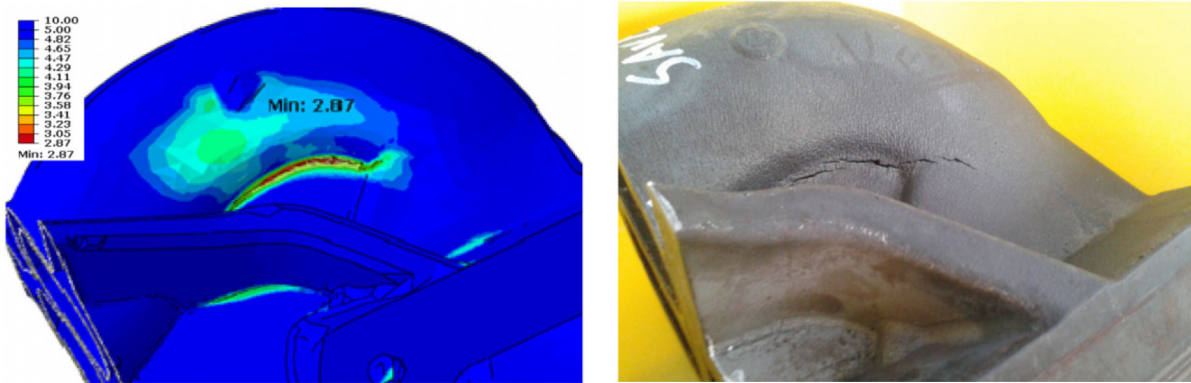


Figure 4.57: Predicted $N_f=748$ by FE model (left), observed $N_f=810$ and 840 (2 tests, same location) on the component prototype (right) [47]

Therefore it can be stated that the role of the experiment is essential for TMF life predictions.

4.3.4. Limitations of Used Model

- The material models of the exhaust manifold are rate-independent, since the creep properties were unavailable.
- The material models of the exhaust manifold are missing room temperature data. This is because the saturated hysteresis loop for 20°C was not published in the article [65]. However, it was assumed on the basis of Figure 4.4 that there is no significant difference in the cyclic behavior from 20°C to 400°C. The high temperature characteristics are the most important ones for the TMF prediction.
- The material models of the exhaust manifold do not account for isotropic (cyclic) hardening/softening. However, this was described in the literature as not a significant influencing factor, since the material does not significantly harden/soften cyclically [70].
- The material models of the exhaust manifold do not account for the effects of ratcheting. Specific experiments would have to be conducted for such material model calibration. However, ratcheting has not been mentioned in any component related reference used in this thesis, except for [18]. So it can be stated that omitting ratcheting is not an uncommon simplification.
- The fatigue life models do not account for the effects of σ_m .
- The fatigue life models do not account for the creep damage mechanism. The same was done in the same application in [20, 55].

- The fatigue life models do not account for the fact that fatigue life is dominated by microcrack growth along specific planes (i.e. shear planes or tensile planes). This phenomenon is accounted for in CPA fatigue life models [77].
- The material data used for material model calibration were assumed as deterministic. It would be preferable to conduct more experiments (i.e. a statistically significant data set) to evaluate it with stochastic approaches using statistical methods.
- The material models of mating components are linear elastic, they might be too stiff if some local plasticity appears. This could be the reason for high contact stresses on the exhaust manifold. However, the same approach was done in [55].
- The model of thermal boundary conditions is based on a steady state CHT (which is common practice due to computational effort), however the reality is closer to transient CHT. The difference between the steady state and transient CHT was studied in [51].
- The effects of radiation are taken indirectly in the natural convection.
- The internal pressure was disregarded, same as in [55].
- There is no gasket in-between the manifold and the cylinder head. It is assumed that the presence of the gasket has no influence on the fatigue life prediction of the manifold.

5. Conclusion

In the first part of the thesis (Chapters 2 and 3), the research study was carried out. The study discussed the damage mechanisms present in TMF, the typical material groups used in the hot end applications, typical uniaxial tests and some of the phenomena of material behavior. Afterwards, an algorithm used for the TMF life predictions was reviewed, and overviews of material and fatigue life models suitable for this problem have been presented.

The second part of this thesis (Chapter 4) applied the previous research to the case study. The case study analyzes a fabricated 3D model of the exhaust manifold. The manifold is considered to be made of SiMo 4.06 cast iron, for which the isothermal and non-isothermal uniaxial tests were performed and digitalized from the literature. The temperature-dependent physical properties were also found in the literature. Since the creep properties of the material were absent, two rate-independent material models with kinematic hardening were calibrated on the basis of uniaxial tests – BKIN and Chaboche. Both models were validated with experiments on both isothermal and non-isothermal levels. The importance of the decreasing trend of the identified constants plotted against temperature was discussed. One of the most important drawbacks of the thesis is the rate-independency of the models, meaning the creep effects were not accounted for. This is one of the most important possibilities for further research. Two steady state CHT analyses were done in order to estimate the thermal boundary conditions. The boundary conditions for the CHT analyses were partly taken from references and partly based on the discussion with an expert in the field. Afterwards, the HTC and T_{bulk} from CHT analyses were mapped onto a discretized FE model in the transient thermal module. The transient thermal simulation identifies the temperature in each discrete node of the FE model in time. The effect of the presence of a water-cooled engine head was taken into account. In order to predict the fatigue life, the strains caused by thermal loading must be known. Hence a structural simulation succeeds. The one-way coupled interaction supposes that the deformation caused by temperature does not affect the spatial temperature distribution back. The structural simulation calculates strains in the nodes using the coefficient of thermal expansion. The structural constrains caused by bolt pretension were considered in the model.

The paradigm of the uncoupled model for the LCF allows the fatigue life prediction to be conducted in sequence. At first, the strain and stress tensors are calculated in the FEA and then the fatigue life prediction is conducted in the post-processing. The damage does not influence mechanical response significantly. Hence, stress and strain tensors calculated in a representative cycle from the structural FEA serve as an input to the fatigue life model. Two fatigue life models without mean stress correction were applied. The first model was a temperature-independent energy-based fatigue life model proposed and calibrated in the literature. The second model was a temperature-dependent strain-based fatigue life model calibrated from the uniaxial data by the author. The energy-based model uses scalar quantity dissipated energy per cycle, which has a straightforward multi-axial formulation, and the post-processing was conducted inside of the commercial FE software since it is temperature-independent. The strain-based model uses the total strain amplitude quantity per cycle, which does not have a straightforward multi-axial formulation. The equivalent total strain amplitude using maximum shear theory has been used for the multi-axial formulation. In order to interpolate between temperatures for the strain-

based model, an in-house code was developed, which uses the nodal temperatures from the transient thermal analysis and nodal strain amplitudes from the structural analysis. The code calculates the number of cycles to failure in each node with respect to temperature, and the spatial distribution of this quantity is mapped back onto the FE mesh in order to display the result as a contour plot.

The structural FEM simulations were repeated a few times with a refined mesh in the critical area, until the predicted number of cycles to failure was assumed to be convergent. Since the fatigue life models works with the power laws, a small variation in the input can result in quite a large variation of the output. Hence, the predicted number of cycles to failure is considerably sensitive to mesh size.

Two material models and two fatigue life models result in 4 separate sets of results, which have been analyzed. As the Chaboche material model has the lower yield stress value, the plasticity was predicted on more and larger areas in comparison to BKIN material model. However, the critical area was predicted on the same location. With the same fatigue life model, the variation of the material model did not make a significant difference in the life prediction in the critical location of this case. The decisive influence on the prediction of the fatigue life in the critical location has in this case been the fatigue life model. The energy-based model predicted more conservative values in terms of fatigue life compared to the strain-based model. However, all four sets of results predict the critical location on the same spot, and the difference between the predicted N_f is of factor of 2 with respect to variation of the fatigue life model. The factor of 2 deviation does not seem to be an enormous error – in [40], the deviation between applied fatigue life models on the component was a factor of 3 in the critical location. As a part of further research, the author suggests to expand Chaboche model into the visco-plastic version (as described in the theoretical part), which can account for the creep effects. Additionally, the fatigue life models do not account for the fact that the fatigue life is dominated along specific (the so-called critical) planes. Therefore, the CPA is suggested as a part of next research. Also the mean stress corrections have been discussed as another possible improvement.

Since the case was fabricated and there were no resources available, the component tests have only been proposed in order to validate applied approaches. As part of the next research, a real component could be analyzed and validated by these tests.

Bibliography

- [1] MASING, G.: Eigenspannungen und Verfestigung beim Messing. *In Proceedings of the 2nd International Congress of Applied Mechanics*. Zürich, Switzerland, 1926, pp. 332–335.
- [2] VON REUSS, A.: Berücksichtigung der elastischen Formänderung in der Plastizitätstheorie. *Zeitschrift für Angewandte Mathematik und Mechanik*. 1930, Vol. 10, Issue 2, pp. 266–274.
- [3] RAMBERG, W., OSGOOD, W. R.: *Description of stress-strain curves by three parameters*. National Advisory Committee for Aeronautics, 1943. Technical Note No. 902.
- [4] PRAGER, W.: A New Method of Analyzing Stresses and Strains in Work-Hardening Plastic Solids. *European Structural Journal of Applied Mechanics*. 1956, pp. 493–496.
- [5] MANSON, S. S., HIRSCHBERG, M. H.: Fatigue behavior in strain cycling in the low and intermediate-cycle range. *In 10th Sagamore Army Research Conference: Fatigue—An Interdisciplinary Approach*. New York, U.S.A., 1963, pp. 13–16.
- [6] ARMSTRONG, P. J., FREDERICK, C. O.: *A Mathematical Representation of the Multiaxial Bauschinger Effect*. Berkeley Nuclear Laboratories, 1966. Report 4258.
- [7] TAIRA, S.: Relationship between thermal fatigue and low-cycle fatigue at elevated temperature. *Fatigue at Elevated Temperatures: ASTM STP520*. 1973, pp. 80–101. DOI:10.1520/STP38831S.
- [8] CHABOCHE, J. L.: Time-independent constitutive theories for cyclic plasticity. *International Journal of Plasticity*. 1986, Vol. 2, Issue 2, pp. 149–188. DOI:10.1016/0749-6419(86)90010-0.
- [9] NEU, R. W., SEHITOGLU, H.: Thermomechanical Fatigue, Oxidation, and Creep: Part I. Damage Mechanisms. *Metallurgical Transactions A*. 1989, Vol. 20, pp. 1755–1767.
- [10] NEU, R. W., SEHITOGLU, H.: Thermomechanical fatigue, oxidation, and Creep: Part II. Life prediction. *Metallurgical Transactions A*. 1989, Vol. 20, pp. 1769–1783.
- [11] ZHUANG, W. Z., SWANSSON, N. S.: *Thermo-Mechanical Fatigue Life Prediction: A Critical Review*. Melbourne, Australia: Defence Science and Technology Organisation Aeronautical and Maritime Research Laboratory, 1998. DSTO-TR-0609.
- [12] ASM INTERNATIONAL.: *ASM handbook: Volume 08: Mechanical Testing and Evaluation*. Materials Park, Ohio, U.S.A.: ASM International, 2000, 10th ed. ISBN-10: 0871703890.
- [13] ASM INTERNATIONAL.: *ASM handbook: Volume 19: Fatigue and Fracture*. Materials Park, Ohio, U.S.A.: ASM International, 2000, 10th ed. ISBN-10: 0871703890.

- [14] LEDERER, G., CHARKALUK, E., VERGER, L., CONSTANTINESCU, A.: Numerical Lifetime Assessment of Engine Parts Submitted to Thermomechanical Fatigue, Application to Exhaust Manifold Design. *SAE Technical Paper: 2000-01-0789*. 2000, ISSN 0148-7191.
- [15] ANSYS, INC.: *Advanced Structural Nonlinearities 6.0, Chapter Three: Plasticity*. 2001. Training Manual.
- [16] BIGNONNET, A., CHARKALUK, E.: Thermomechanical Fatigue in the Automotive Industry. *European Structural Integrity Society*. 2002, Vol. 29, pp. 319-330.
- [17] CHARKALUK, E., BIGNONNET, A., CONSTANTINESCU, A., DANG VAN, K.: Fatigue design of structures under thermomechanical loadings. *Fatigue and Fracture of Engineering Materials and Structures*. 2002, Vol. 25, pp. 1199-1206. DOI:10.1046/j.1460-2695.2002.00612.x.
- [18] HAZIME, R. M., DROPPS, S. H., ANDERSON, D. H., ALI, M. Y.: Transient Non-linear FEA and TMF Life Estimates of Cast Exhaust Manifolds. *SAE International*. 2003. DOI:10.4271/2003-01-0918. SAE Technical Paper 2003-01-0918.
- [19] KUTZ, J. N.: *AMATH 301 Beginning Scientific Computing*. Seattle, U.S.A.: University of Washington, Department of Applied Mathematics, 2003. Study Text. Available online: <http://courses.washington.edu/am301/docs/pdf/301.pdf>.
- [20] HEUER, T., ENGELS, B., WOLLSCHIED, P.: Thermomechanical Analysis of a Turbocharger Based on Conjugate Heat Transfer. *ASME Turbo Expo 2005: Power for Land, Sea and Air*. BorgWarner Turbo Systems GmbH, 2005. DOI:https://doi.org/10.1115/GT2005-68059.
- [21] MOHRMANN, R., SEIFERT, T., WILLEKE, W., HARTMANN, D.: Fatigue Life Simulation for Optimized Exhaust Manifold Geometry. *SAE International*. 2006. DOI:https://doi.org/10.4271/2006-01-1249. SAE Technical Paper 2006-01-1249.
- [22] PEJCHAL, P., PETRUŠKA, J.: *The material model of railway wheel for numerical simulations of cyclic deformation*. Prague, Czech Republic: Institute of Theoretical and Applied Mechanics, AS CR, v.v.i., 2006. Conference Paper.
- [23] SANTACREU, P. O., BUCHER, L., KOSTER, A., REMY, L.: Thermomechanical fatigue of stainless steels for automotive exhaust systems. *La Revue de Métallurgie-CIT*. 2006. DOI:10.1051/metal:2006102.
- [24] PETRUŠKA, J.: *Řešení úloh vedení tepla a teplotní napjatosti pomocí MKP*. Brno, Czech Republic: FSI VUT v Brně, Ústav mechaniky těles, mechatroniky a biomechaniky, 2007. Study Text.
- [25] GLINKA, G.: *The strain life approach to approach to fatigue life assessment of weldments*. 2008. Available online: http://utmis.org.loopiadns.com/media/2016/08/Weldments3_Fatigue_Stockholm_08.pdf.
- [26] ANSYS, INC.: *How do compute the heat transfer coefficient in CFD-Post?* Canonsburg, U.S.A., 2009. FAQs.

- [27] SEIFERT, T., RIEDEL, H.: *Fatigue Life Prediction of High Temperature Components in Combustion Engines and Exhaust Systems*. Freiburg, Germany: Fraunhofer Institute for Mechanics of Materials IWM, Business Unit Component Safety, 2009. Conference Paper.
- [28] ANSYS, INC.: *ANSYS nCode DesignLife*. 2010. Software Brochure. Available online: <https://www.simutechgroup.com/images/ansys-suites/structures/ansys-ncode-designlife-brochure.pdf>.
- [29] LAENGLER, F., MAO, T., ALEKSANOGLU, H., SCHOLZ, A.: *Phenomenological Lifetime Assessment for Turbine Housings of Turbochargers*. Parma, Italy: 9th Int Conference on multiaxial fatigue & fracture in Parma, 2010. Conference Paper.
- [30] SCHICKER, J., SIEVERT, R., FEDELICH, B., NOACK, H. D., KAZAK, F., MATZAK, K., KÜHN, H. J., KLINGELHÖFFER, H., SKROTZKI, B.: *TMF Lebensdauerberechnung ATL-Heißeile*. Frankfurt, M., Germany: Forschungsvereinigung Verbrennungskraftmaschinen e.V., Vol. 902, 2010. Report.
- [31] BERGMAN, L. T., LAVINE, S. A., INCROPERA, P. F., DEWITT, P. D.: *Fundamentals of Heat and Mass Transfer*. John Wiley and Sons, Inc., 2011. 7th ed. ISBN 13978-0470-50197-9.
- [32] INCE, A., GLINKA, G.: A modification of Morrow and Smith–Watson–Topper mean stress correction models. *Fatigue and Fracture of Engineering Materials and Structures*. 2011, Vol. 34, pp. 854-867. DOI:10.1111/j.1460-2695.2011.01577.x.
- [33] LAENGLER, F., MAO, T., ALEKSANOGLU, H., SCHOLZ, A.: Investigation of application-specific phenomena to improve the lifetime assessment for turbine housings of turbochargers. *Procedia Engineering*. 2011, Vol. 10, pp. 1163-1169. DOI:10.1016/j.proeng.2011.04.194.
- [34] ŠERUGA, D., NAGODE, M.: Unification of the most commonly used time–temperature creep parameters. *Materials Science and Engineering*. 2011, Vol. 528, Issue 6, pp. 2804-2811. DOI:10.1016/j.msea.2010.12.034.
- [35] ANSYS, INC.: *Lecture 2 Advanced Metal Plasticity*. 2012. ANSYS Mechanical Advanced Nonlinear Materials, Manual.
- [36] HALAMA, R., SEDLÁK, J., ŠOFER, M.: *Phenomenological Modelling of Cyclic Plasticity*. Numerical Modelling, Dr. Peep Miidla (Ed.), InTech, 2012. ISBN: 978-953-51-0219-9, DOI:10.5772/35902. Available online: <http://www.intechopen.com/books/numerical-modelling/phenomenological-modelling-of-cyclic-plasticity>.
- [37] LI, Q., WEI, D., MOSER, B., SIT, D., THOMPSON, S.: *TMF Lite Process Development*. Caterpillar Inc., SIMULIA Community Conference, 2012. Conference Paper.
- [38] RATHNARAJ, J. D.: Thermomechanical Fatigue Analysis of Stainless Steel Exhaust Manifolds. *Indian Journal of Science and Technology*. 2012, Vol. 3, Issue 1, pp. 65-68.

- [39] SATISH, S., PRITHIVIRAJ, M., HARI, S.: *Comparison of predictions obtained on an exhaust manifold analysis using conformal and indirect mapped interface*. Hyderabad, India: International Congress on Computational Mechanics and Simulation (ICCMS), IIT Hyderabad, 2012. Conference Paper.
- [40] AMMAR, K., BERANGER, M., FIARD, JM., MISSOUM, D., QUILICI, S.: *Anisothermal energetic approach to predict thermomechanical fatigue lifetime on exhaust manifold*. 2013. Available online: <https://api.semanticscholar.org/CorpusID:204764146>.
- [41] ANSYS, INC.: *Lecture 6 Static Data Transfer. Solving FSI Applications Using ANSYS Mechanical and ANSYS Fluent*. 2013. Manual.
- [42] EKSTRÖM, M.: *Development of a Ferritic Ductile Cast Iron for Increased Life in Exhaust Application*. Stockholm, Sweden: Department of Materials Science and Engineering, Division of Mechanical Metallurgy, Royal Institute of Technology, 2013. ISBN 978-91-7501-711-2.
- [43] EKSTRÖM, M., JONSSON, S.: High-temperature mechanical- and fatigue properties of cast alloys intended for use in exhaust manifolds. *Materials Science and Engineering: A*. 2014, Vol. 616, pp. 78-87. DOI:10.1016/j.msea.2014.08.014.
- [44] JANÍČEK, P.: *Systémová metodologie: brána do řešení problémů*. Brno, Czech Republic: Akademické nakladatelství CERM, 2014. ISBN 978-80-7204-887-8.
- [45] LIU, Y., MILLER, L., CHEN, J.: *Thermo-Mechanical Fatigue (TMF) Virtual Analysis for Exhaust Manifold Durability Using FEMFAT HEAT*. Chrysler Group LLC, 2014. FEMFAT User Meeting. Conference Presentation.
- [46] PEVEC, M., ODER, G., POTRČ, I., ŠRAML, M.: Elevated temperature low cycle fatigue of grey cast iron used for automotive brake discs. *Engineering Failure Analysis*. 2014, Vol. 42, pp. 221-230. DOI:10.1016/j.engfailanal.2014.03.021.
- [47] SEIFERT, T., HAZIME, R., DROPPS, S.: TMF Life Prediction of High Temperature Components Made of Cast Iron HiSiMo: Part II: Multiaxial Implementation and Component Assessment. *SAE International Journal of Materials and Manufacturing*. 2014, Vol. 7, Issue 2. DOI:10.4271/2014-01-0905.
- [48] SEIFERT, T.: *Werkstoffmechanik*. Offenburg, Germany: Hochschule Offenburg, 2014. Study Text.
- [49] VON HARTROTT, P., SEIFERT, T., DROPPS, S.: TMF Life Prediction of High Temperature Components Made of Cast Iron HiSiMo: Part I: Uniaxial Tests and Fatigue Life Model. *SAE International Journal of Materials and Manufacturing*. 2014, Vol. 7, Issue 2. DOI:10.4271/2014-01-0915.
- [50] CAILLETAUD, G., QUILICI, S., AZZOUZ, F., CHABOCHE, J. L.: A dangerous use of the fading memory term for non linear kinematic models at variable temperature. *European Journal of Mechanics A/Solids*. 2015, Vol. 54, pp. 24-29. DOI:10.1016/j.euromechsol.2015.06.007.

- [51] FAN, S. C.: *The Thermal Mechanical Fatigue (TMF) Analysis for an Exhaust Manifold – An Application of File Based Coupling*. HAITEC. San Diego, U.S.A.: STAR Global Conference, 2015. Conference Presentation.
- [52] LORET, A.: *Hot Gas Stand Durability Tests for Turbine Housing Design Validation*. Mitsubishi Turbocharger and Engine Europe BV. 2015.
- [53] ŠPANIEL, M., BARTOŠÁK, M.: *Brief manual of scripts for thermo-mechanical fatigue predictions*. Prague, Czech Republic: Czech Technical University in Prague, Faculty of Mechanical Engineering, Department of Mechanics, Biomechanics and Mechatronics, 2015. Report. Available online: http://mechanika.fs.cvut.cz/content/files/software/tz_script.pdf.
- [54] 3DS SIMULIA: *Abaqus Example Problems Guide, chapter 5.1.3 Exhaust manifold assemblage*. Dassault Systèmes, 2016. Available online: <http://130.149.89.49:2080/v2016/books/exa/default.htm?startat=ch05s01aex119.html>.
- [55] CARDOSO, A. D. A., ANDREATTA, E. C.: Thermomechanical Analysis of Diesel Engine Exhaust Manifold. *SAE International*. 2016. ISSN: 0148-7191. SAE Technical Paper 2016-36-0258.
- [56] REKUN, I., SEIFERT, T., JÖRG, R.: *Determination Of Stable And Robust Material Properties For The Assessment Of Thermomechanically Loaded Components Of Rocket Engines With Viscoplastic Equations*. Toulouse, France: The 14th European Conference on Spacecraft Structures, Materials and Environmental Testing (ECSSMET), 2016. Conference Paper.
- [57] ŠPANIEL, M., BARTOŠÁK, M.: *Software routines for material model of low-cycle thermo-mechanical fatigue in Abaqus FEM software*. Prague, Czech Republic: Czech Technical University in Prague, Faculty of Mechanical Engineering, Department of Mechanics, Biomechanics and Mechatronics, 2016. Technical Report.
- [58] SUMAN, S., SRIDHAR, P., BISWAS, P.: *Numerical prediction of welding distortion in submerged arc welded butt and fillet joints*. Kanchipuram, India: International conference of design and manufacturing, IIITDM, 2016. Conference Paper.
- [59] WANG, D., ZHANG, W., LIU, D., CHEN, X., TANG, G., OKOSUN, T., WU, B., ZHOU, C. Q.: *CFD Simulation of a 6-Cylinder Diesel Engine Intake and Exhaust Manifold*. Houston, U.S.A.: Proceedings of the ASME 2015 International Mechanical Engineering Congress and Exposition, 2016. Conference Paper. DOI:<https://doi.org/10.1115/IMECE2015-52399>.
- [60] AHMED, R., BARRETT, P. R., MENON, M., HASSAN, T.: Thermo-mechanical low-cycle fatigue-creep of Haynes 230. *International Journal of Solids and Structures*. 2017, Vols. 126–127, pp. 90-104. DOI:10.1016/j.ijsolstr.2017.07.033.
- [61] HAZIME, R., SEIFERT, T., KESSENS, J., JU, F.: Lifetime Assessment of Cylinder Heads for Efficient Heavy Duty Engines Part I: A Discussion on Thermomechanical and High-Cycle Fatigue as Well as Thermophysical Properties of Lamellar Graphite Cast Iron GJL250 and Vermicular Graphite Cast Iron GJV450. *SAE International Journal of Engines*. 2017, Vol. 10, Issue 2. DOI:10.4271/2017-01-0346.

- [62] HONEYWELL INTERNATIONAL INC. MORRIS PLAINS, NJ 07950 (US): *Stainless Steel Alloys And Turbocharger Turbine Housings Formed From The Stainless Steel Alloys*. European Patent Specification EP 2 980 253 B1, 2017.
- [63] YOGESH, K., ANANTHESHA, MAHENDRA BABU, N. C.: Assessment of Thermo-Mechanical Fatigue Performance of an Exhaust Manifold through Simulation. *Indian Journal of Science and Technology*. 2017, Vol. 10, Issue 12. DOI:10.17485/ijst/2017/v10i12/105559.
- [64] ANSYS, INC.: *Thermo-Mechanical Fatigue White Paper*. Canonsburg, U.S.A., 2018.
- [65] BARTOŠÁK, M., NOVOTNÝ, C., ŠPANIEL, M., DOUBRAVA, K.: Life assessment of SiMo 4.06 cast iron under LCF and TMF loading conditions. *Materials at High Temperatures*. 2018, Vol. 36, Issue 4, pp. 285-295. DOI:10.1080/09603409.2018.1542825.
- [66] JÄÄSKELÄINEN, H.: Diesel Exhaust Gas. In: *DieselNet* [online]. Revision 2018.01. Ecopoint Inc. Available online: https://www.dieseln.net/tech/diesel_exh.php.
- [67] LIU, Y., CHEN, Y. SAWKAR, N., XU, N., GAIKWAD, S., SEATON, P., SINGH, K.: A Thermomechanical Fatigue Analysis on a Ductile Cast Iron Exhaust Manifold. *SAE International Journal of Materials and Manufacturing*. 2018, Vol. 11, Issue 4, pp. 517-528. DOI:10.4271/2018-01-1215.
- [68] NĚMEC, I., TRCALA, M., REK, V.: *Nelineární mechanika*. Brno, Czech Republic: Vysoké učení technické v Brně, nakladatelství VUTIUM, 2018. ISBN: 978-80-214-5519-1.
- [69] WANG, W., MA, Y., YANG, M., JIANG, P., YUAN, F., WU, X.: Strain Rate Effect on Tensile Behavior for a High Specific Strength Steel: From Quasi-Static to Intermediate Strain Rates. *Metals*. 2018, Volume 8, Issue 1, 11. DOI:10.3390/met8010011.
- [70] BARTOŠÁK, M., ŠPANIEL, M., DOUBRAVA, K.: Life assessment of SiMo 4.06 turbocharger turbine housing: Damage operator approach. *Engineering Failure Analysis*. 2019, Vol. 105, pp. 736-755. DOI:10.1016/j.engfailanal.2019.06.0685.
- [71] HAZIME, R., SEIFERT, T., CHANG, C. C., KASSIR, A., SETHY, A.: A Mechanism-Based Thermomechanical Fatigue Life Assessment Method for High Temperature Engine Components with Gradient Effect Approximation. *SAE International*. 2019. DOI:10.4271/2019-01-0536. SAE Technical Paper 2019-01-0536.
- [72] PEČ, M., ŠEBEK, F., ZAPLETAL, J., PETRUŠKA, J., HASSAN, T.: Automated calibration of advanced cyclic plasticity model parameters with sensitivity analysis for aluminium alloy 2024-T351. *Advances in Mechanical Engineering*. 2019, Vol. 11, Issue 3, pp. 1-14. DOI:10.1177/1687814019829982.
- [73] ŠPANIEL, M., KUŽELKA, J., BARTOŠÁK, M., FUMFERA, J.: *Výpočtová predikce nízkocyklové únavy*. Prague, Czech Republic: Conference CAE Forum 2019, 17. – 18. 10. Park Holiday Hotel Prague, 2019. Conference Presentation.

- [74] BARTOŠÁK, M., ŠPANIEL, M., DOUBRAVA, K.: Unified viscoplasticity modelling for a SiMo 4.06 cast iron under isothermal low-cycle fatigue-creep and thermo-mechanical fatigue loading conditions. *International Journal of Fatigue*. 2020, Vol. 136, 105566. DOI:10.1016/j.ijfatigue.2020.105566.
- [75] BURŠA, J.: *Strength of materials II- Fatigue failure*. Study Text. Available online: <http://www.old.umd.fme.vutbr.cz/~jbursa/Backgrounds/2-3A-lecture-fatigue.pdf>.
- [76] WALZENGIESSEREI COSWIG, GMBH: EN-GJL-250 Physical properties. In: *Walze-Coswig* [online]. Available online: <https://www.walze-coswig.com/hand-mould-casting/material-information>.
- [77] EFATIGUE ALTAIR ENGINEERING, INC.: Multiaxial Strain-Life Technical Background. In: *eFatigue* [online]. Available online: <https://www.efatigue.com/multiaxial/background/strainlife.html>.
- [78] ENGINEERS EDGE, LLC.: Thermal Contact Conductance. In: *ENGINEERS EDGE* [online]. Available online: https://www.engineersedge.com/heat_transfer/thermal_contact_conductance_13849.htm.
- [79] FATEMI, A.: *Chapter 10 – Multiaxial Fatigue*. Toledo, U.S.A.: University of Toledo. Training Presentation. Available online: https://www.efatigue.com/training/Chapter_10.pdf.
- [80] MATHWORKS, INC: MATLAB Manual: fmincon. In: *MathWorks* [online]. Available online: <https://www.mathworks.com/help/optim/ug/fmincon.html>.
- [81] VLACH, R.: *Tepelné procesy v mechatronických soustavách: Tepelné odpory*. Brno, Czech Republic: Ústav mechaniky těles, mechatroniky a biomechaniky, Fakulta strojíňho inženýrství, Vysoké učení technické v Brně. Study Text.
- [82] VLACH, B.: *Creep – tečení*. Study Text. Available online: http://imse.fme.vutbr.cz/images/umvi/vyuka/mezni_stavy/prednasky/10_6MS_creep.pdf.
- [83] [Figure] Glowing hot end of the combustion engine. Available online: <https://qph.fs.quoracdn.net/main-qimg-cf008c30a001881d182f1d33ebb467b8>.

6. List of symbols and abbreviations

LATIN SYMBOLS

a	fatigue strength exponent
A	energy-based fatigue criterion constant
A_N	coefficient in Norton's creep model
\mathbf{A}	linear inequality constrain matrix
b	fatigue ductility exponent
B	energy-based fatigue criterion constant
\mathbf{b}	linear inequality constraints vector
c_p	specific heat
C	Chaboche's constant proportional to hardening modulus
$ceq(x)$	equality constraint
E	Young's modulus
E_T	tangent hardening modulus
$E_{(pl)}$	elastic modulus in elasto-plastic network
$E_{(v)}$	elastic modulus in visco-elastic network
f	ratio of elastic moduli, a constant for two-layer visco-plastic model
$f(x)$	objective function
F	yield surface
G	shear modulus
HTC	heat transfer coefficient
HTC_{amb}	ambient heat transfer coefficient
k	number of backstresses
K'	cyclic strength coefficient
lb	lower bounds
\dot{m}	exhaust gas mass flow
n	number of temperature levels
n_N	exponent in Norton's creep model
n'	cyclic strain hardening exponent
N_f	number of cycles to failure
$N_{pp,cc,pc,cp}$	numbers of cycles to failure due to specific damage cycle, used in strain range partitioning fatigue life model
$N_{fat,ox,creep}$	numbers of cycles to failure due to fatigue, oxidation or creep, used in Neu-Sehitoglu fatigue life model
P	exhaust gas outlet static pressure
q	specific heat transfer rate
Q_{CHT}	heat transfer rate from CHT simulation
Q_{theor}	heat transfer rate calculated from the energetic balance equation
Q_p	plastic potential
Q_N	activation energy
R	universal gas constant
R_m	ultimate tensile strength
R_{ϵ^m}	mechanical strain ratio, also called constraint

R_σ	stress ratio
\underline{S}	deviatoric stress tensor
t	time
T	temperature
T_0	surroundings temperature
T_1	exhaust gas inlet temperature
T_{amb}	ambient temperature
T_{bulk}	bulk temperature
T_{cont}	temperature at inlet flange of manifold
T_{extern}	external wall temperature
T_{melt}	melting temperature
T_s	surface temperature
T_{wall}	(internal) wall temperature
T_Δ	drop of the exhaust gas temperature from inlet to outlet
ub	upper bounds
w	dissipated energy per cycle
\tilde{w}	modified dissipated energy per cycle
x, y, z	spatial coordinates
\tilde{x}	unknown set of material constants
x_0	initial guess of constants
y^+	dimensionless wall distance
Y	isotropic hardening function

GREEK SYMBOLS

α	coefficient of thermal expansion
$\alpha_{\tilde{w}}$	modified energy-based fatigue life criterion constant
$\underline{\alpha}$	backstress
γ	Chaboche's constant, rate of decrease of hardening modulus
ε	total strain
ε_1	maximum principal strain
ε_3	minimum principal strain
ε_{creep}	strain related to creep
ε_{el}	elastic strain
$\varepsilon_{el(pl)}$	elastic strain in elasto-plastic network
$\varepsilon_{el(v)}$	elastic strain in visco-elastic network
ε_m	mean strain
ε_{pl}	plastic strain
ε_v	viscous strain
ε_{vp}	visco-plastic strain
ε^m	mechanical strain
ε^{th}	thermal strain
$\hat{\varepsilon}_{pl}$	accumulated plastic strain

$\underline{\varepsilon}_{pl}$	plastic strain tensor
ε'_f	fatigue ductility coefficient
$\dot{\varepsilon}_{creep}$	strain rate related to creep
$\dot{\varepsilon}_{ss}$	steady state strain rate related to secondary creep
$\dot{\underline{\varepsilon}}_{pl}$	mechanical plastic strain rate tensor
λ	thermal conductivity
λ_p	plastic multiplier
μ	Poisson's ratio
ρ	density
σ	stress
σ_0	yield stress
$\sigma_{I,II,III}$	principal stresses
σ_A	generic stress value larger than yield stress
σ_c	endurance limit
σ_m	mean stress
$\underline{\sigma}$	stress tensor
σ'_f	fatigue strength coefficient

RECURRENT SUBSCRIPTS & PRESCRIPTS

a	amplitude of quantity in the cycle
eqv	equivalent by von Mises condition unless otherwise stated
i,j	indexes
max	maximum of quantity in the cycle
min	minimum of quantity in the cycle
Δ	range of quantity in the cycle

ABBREVIATIONS

2LVP	Two-Layer Visco-Plastic
APDL	ANSYS Parametric Design Language
BC	Boundary Conditions
BKIN	Bilinear Kinematic Hardening
CFD	Computational Fluid Dynamics
CHT	Conjugate Heat Transfer
CLCF	Complex Low Cycle Fatigue
CPA	Critical Plane Approach
DCCW	Diamond Counterclockwise
DCW	Diamond Clockwise
EVH	Exponential Visco-Hardening
FE	Finite Element
FEA	Finite Element Analysis
FEM	Finite Element Method

HCF	High Cycle Fatigue
IF	Isothermal Fatigue
IPTMF	In-Phase Thermo–Mechanical Fatigue
LCF	Low Cycle Fatigue
LVDT	Linear Variable Differential Transformer
OPTMF	Out-of-Phase Thermo–Mechanical Fatigue
SiMo	Silicon–Molybdenum
SRP	Strain Range Partitioning
SWT	Swift–Watson–Topper
TC	Thermo-Couple
TMF	Thermo–Mechanical Fatigue
UY	displacement in y axis direction

7. Appendix

Appendix A: Validation of Chaboche Model With Recent Experiments

Figure 7.1 shows the calibrated Chaboche model validated with recently published experiments from [74]. Due to a time shortage, these experiments were not used for the calibration of the model.

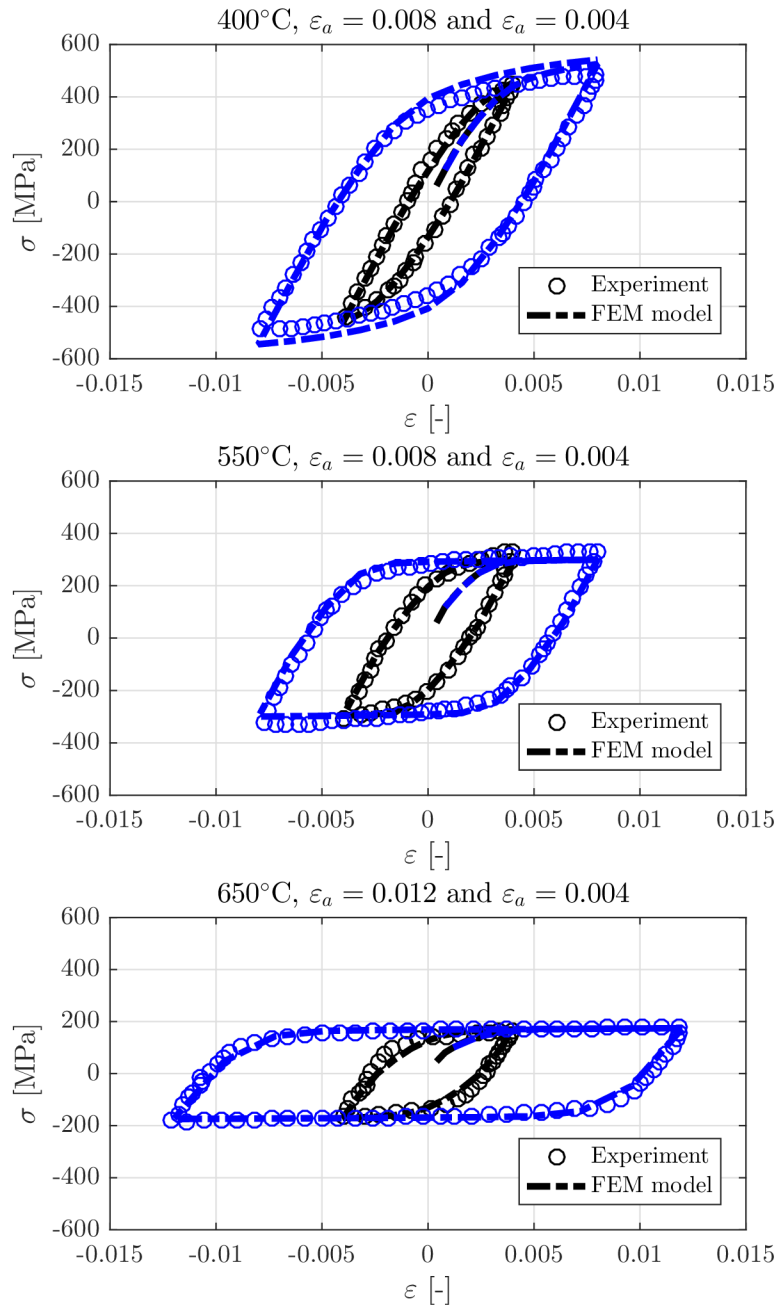


Figure 7.1: Validation of the Chaboche model with various strain amplitudes. However, these experiments were not used for the calibration. Experimental data are from [74].

Appendix B: OPTMF Test With Various Cyclic Plasticity Models

Figure 7.2, provided by prof. Dr.-Ing. Thomas Seifert, shows various cyclic plasticity models validated with OPTMF test. The rate-independent kinematic hardening model over-predicts stresses in high-temperature region due to neglect of rate-dependent effects. The behavior is consistent with the case study of this thesis.

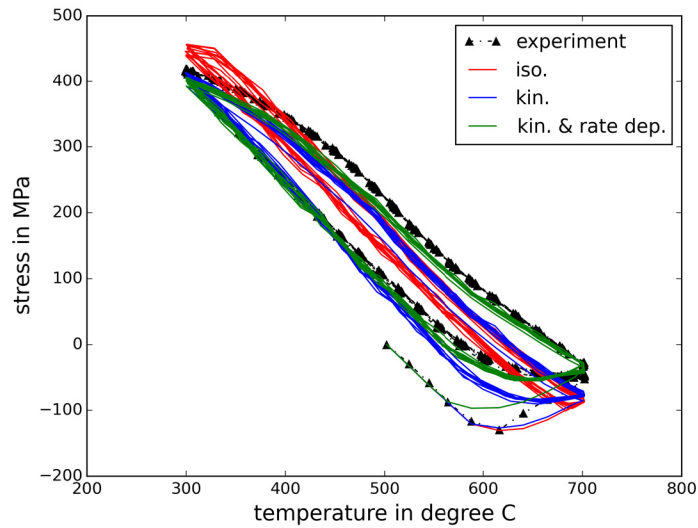


Figure 7.2: OPTMF test - different material models applied on SiMo alloy, courtesy of prof. Dr.-Ing. Thomas Seifert, Offenburg University of Applied Sciences (thomas.seifert@hs-offenburg.de), email conversation

Appendix C: The Difference Between the Uniaxial and Multiaxial Formulation of Strain Amplitude Applied to the Uniaxial Test

Why can the deviation between the uniaxial and multiaxial formulation of the strain amplitude in the strain-based criterion not be larger than 15 % when applied to uniaxial test? The strain amplitude for the uniaxial test, calculated using the equivalent strain approach with respect to maximum shear theory, is:

$$\begin{aligned} \frac{\varepsilon_{1,a} - \varepsilon_{3,a}}{1 + \mu_{el}} &= \frac{\varepsilon_{1,a,el} - \varepsilon_{3,a,el}}{1 + \mu_{el}} + \frac{\varepsilon_{1,a,pl} - \varepsilon_{3,a,pl}}{1 + \mu_{el}} = \frac{\varepsilon_{1,a,el} + \mu_{el} \varepsilon_{1,a,el}}{1 + \mu_{el}} + \frac{\varepsilon_{1,a,pl} + \mu_{pl} \varepsilon_{1,a,pl}}{1 + \mu_{el}} = \\ &= \varepsilon_{1,a,el} + \frac{\varepsilon_{1,a,pl} + 0.5 \varepsilon_{1,a,pl}}{1 + 0.3} = \varepsilon_{1,a,el} + \frac{1.5}{1.3} \varepsilon_{1,a,pl} = \varepsilon_{a,1,el} + 1.15 \varepsilon_{a,1,pl} \end{aligned}$$

where Poisson's ratio is 0.3 for elastic deformation and 0.5 for plastic deformation. Hence:

$$\text{uniaxial formulation: } \varepsilon_a = \varepsilon_{1,a,el} + \varepsilon_{1,a,pl}$$

$$\text{multiaxial formulation: } \varepsilon_a = \varepsilon_{1,a,el} + 1.15 \varepsilon_{1,a,pl}$$

It is evident that the 15 % difference can only be for perfectly plastic deformation. However, in reality there is also some elastic deformation present, therefore the deviation will always be smaller than 15 %.